

PHOTOIONIZATION/PHOTODETACHMENT SPECTROSCOPY AND DYSON
ORBITALS: THEORETICAL TOOLS TO AID EXPERIMENTAL STUDIES

by

Anastasia Gunina

A Dissertation Presented to the
FACULTY OF THE USC GRADUATE SCHOOL
UNIVERSITY OF SOUTHERN CALIFORNIA
In Partial Fulfillment of the
Requirements for the Degree
DOCTOR OF PHILOSOPHY
(CHEMISTRY)

May 2017

Acknowledgements

First of all, I would like to express my deep gratitude towards my research adviser, Professor Anna I. Krylov. She happens to possess a very rare combination of strong passion to science and seemingly endless patience. These qualities create an outstanding mentor and a bright role model to follow and improve yourself. Under her guidance, you never run out of support and encouragement, which is not less important than (also generous) direct teaching and knowledge sharing. Her attention to promoting students' scientific development via custom-tailored interests-based set of research activities contributes a lot into creating well-rounded experience and preparing for life after graduation. In addition, I would like to specially acknowledge Prof. Krylov's enthusiasm in promoting the idea of women in science, which greatly facilitated my personal development and helped me to build confidence over graduate school years.

Graduate school was a great time, and great time is in considerable part defined by having great people around: colleagues and friends. Friends in the U.S. – Nadia, Nastia, Lyuda, John, Roma, Vlad, Dasha, Pasha – were always around to support, to discuss general and philosophic matters, and of course to participate in fun activities

and unwinding. Friends in Russia – Masha, Ksyusha, Galya, Vera, Masha, Olya, Vika, Oksana, and Tatiana Antonovna – remained warm and welcoming despite long years and distances. Maxim made a special contribution to my life by encouraging to come to USC for a summer research program and recommending “some strong female professor in theoretical chemistry” in a line with my emerging interest of the time, which subsequently turned into entering specific graduate school and joining particular research lab. It is interesting how small factors sometimes sum up into something life-determining.

Most of graduate student’s life gets spent in the lab, so it was a pleasure to be a part of enthusiastic, open-minded, and supportive research group, with a thriving culture of sharing knowledge and helping each other. Everybody was a great labmate, yet I would like to specially thank Dr. Evgeny Epifanovsky and Dr. Dmitry Zuev for teaching me basics of coding in Q-Chem, as well as Dr. Samer Gozem for his work on debugging and improving *ezDyson* code.

Outside of the department, I would like to thank our experimental collaborators, Prof. Dr. Ruth Signorell and Dr. Musahid Ahmed, for bringing us interesting challenges to contribute into. Help from Prof. John Stanton, Dr. Takatoshi Ichino, and Dr. Ilya Ryabinkin in testing Dyson orbitals code is gratefully acknowledged.

Last but not least, I would like to thank people that raised me over the years preceding graduate school: parents and teachers. I learned a lot from Prof. Sergey I. Lopatin, who allowed me into his lab on my freshman year, contributed countless hours of supervising experimental work and discussing the results, and later facilitated

a shift of interest towards combining theoretical modeling with experiments to study nature. Dr. Sergey G. Semenov, Prof. Andrei I. Panin and Prof. Alexander V. Tulub gave me initial knowledge in quantum chemistry, well above and beyond formal academic requirements. Finally, my parents always supported my “unconventional” interest towards STEM fields and kept open minds about geopolitical matters, thus making this all possible.

Table of contents

Acknowledgements	ii
List of tables	vii
List of figures	viii
Abstract	xv
Chapter 1: Introduction and overview	1
1.1 Photoelectron spectroscopy and imaging	1
1.2 Solvent effects in photoionization and photodetachment	8
1.3 Chapter 1 references	14
Chapter 2: Theory	28
2.1 Equation-of-motion coupled-cluster family of methods	28
2.2 Dyson orbitals	32
2.3 Chapter 2 references	36
Chapter 3: Photoelectron wave function in photoionization: Plane wave or Coulomb wave?	37
3.1 Photoelectron wave function in photoionization	37
3.2 Appendix A: Detailed comparison between PW and CW for $l=0-5$, Mulliken charges in ionized species, photoionization cross-sections for selected molecules with and without FCFs, comparison between photoelectron radial functions with different Z with formaldehyde's Dyson orbital . . .	54
3.3 Appendix B: Using variational optimization to determine the optimal charge: Formaldehyde example	60
3.4 Chapter 3 references	63
Chapter 4: Probing electronic wave functions of sodium-doped clusters: Dyson orbitals, anisotropy parameters, and ionization cross-sections	69
4.1 Introduction	69
4.2 Theoretical methods and computational details	74

4.2.1	Dyson orbitals within the equation-of-motion coupled-cluster framework	74
4.2.2	Cross-sections and photoelectron angular distributions	78
4.2.3	Computational details	80
4.3	Results and discussion	83
4.3.1	Electronic properties of sodium-doped ammonia and DME clusters	83
4.3.2	Effect of structural fluctuations on electronic properties	94
4.3.3	The effect of correlation on the shape of Dyson orbitals	98
4.3.4	Comparison with experiment	106
4.4	Conclusions	108
4.5	Appendix A: Calculations of total cross-sections and anisotropy parameters	110
4.6	Appendix B: Wave function analysis	114
4.7	Appendix C: The effect of thermal fluctuations on the observables	115
4.8	Appendix D: Comparison of DFT and EOM-EA Dyson orbitals: The effect on β and σ	120
4.9	Chapter 4 references	128
Chapter 5: Photoionization of arginine in gas phase and in solution		132
5.1	Introduction	132
5.2	Computational details	134
5.3	Results and discussion	137
5.3.1	Gas-phase ionization	137
5.3.2	Effect of solvation	140
5.4	Chapter 5 references	146
Chapter 6: Future work		148
6.1	Method development: Electronic structure part, outgoing electron and experimental observables modeling, extension to time-resolved experiments	148
6.2	Understanding solvent effects	151
6.3	Scanning tunneling microscopy	153
6.4	Chapter 6 references	156
Bibliography		159

List of tables

4.1	Electronic properties computed using the EOM-EA-CCSD/aug-cc-pVDZ wave functions for the $\text{Na}(\text{NH}_3)_n$ clusters, $n=1\text{-}10$. VIEs are given in eV and other quantities in a.u.	83
4.2	Electronic properties computed using the EOM-EA-CCSD/aug-cc-pVDZ wave functions for the $\text{Na}(\text{DME})_m$ clusters, $m=1\text{-}7$. Results for $\text{Na}(\text{DME})_5$, $\text{Na}(\text{DME})_6$, and $\text{Na}(\text{DME})_7$ were obtained with modified basis set and reduced orbital space (see text). VIEs are given in eV and other quantities in a.u.	85
4.3	VIEs ($-\epsilon$ as Koopmans' theorem), dipole moments, and properties of the SOMO orbitals for the $\text{Na}(\text{NH}_3)_n$ and $\text{Na}(\text{DME})_m$ clusters ($n=1\text{-}10$, $m=1\text{-}7$) computed at the UHF/6-31+G(d) and DFT/6-31+G(d) levels of theory. Ionization energies are given in eV and other quantities in a.u.	99
4.4	State properties computed using the EOM-EA-CCSD/aug-cc-pVDZ wave functions and properties of the Dyson orbitals for the lowest electronic state of $\text{Na}(\text{NH}_3)_6$ at selected snapshots. VIEs are given in eV and other quantities in a.u.	118

List of figures

1.1	Various flavors of photoelectron spectroscopy. (a) Origin of photodetachment spectra. (b) Time-resolved photoelectron spectroscopy (bottom) and imaging (top).	2
1.2	The effect of single solvent molecule forming a complex with I^- on PADs as well as line positions and relative intensities in the photoelectron spectra.	9
1.3	Examples of the four main types of solvated electrons observed in $(\text{H}_2\text{O})_{40}$: (a) a dipole-bound surface isomer, (b) a surface isomer, (c) a partially embedded surface isomer, and (d) a cavity isomer. The isosurfaces encapsulate 70% of the electron density.	12
1.4	VDEs of solvated electrons in various solvent clusters as a function of cluster size. For water, three distinct isomeric series (labeled I, II, and III) were found; for methanol, two isomers (I and II) were detected. For acetonitrile, two isomers were observed, but only one is plotted here.	13
2.1	Various EOM operators describing electronic excitations, ionizations, electron attachment and open-shell singlets.	31
3.1	Coulomb radial function for $l=0$ and $k=0.068$ a.u. ($E_k=0.0625$ eV), with $Z=0$, 0.5, and 1.0 (black, orange, and blue curves, respectively). The Coulomb radial function with $Z=0$ is identical to the spherical Bessel function. In the systems studied here, Dyson orbitals do not extend beyond 12 bohr.	43
3.2	Absolute cross-sections for photodetachment from H^- , Li^- , and NH_2^- . Red dots are the experimental values. Black and blue curves denote cross-sections computed using PWs and CWs (with $Z=1$), respectively. For NH_2^- , only the relative cross-sections were measured experimentally and so they have been scaled to match absolute cross-sections obtained by calculations. FCFs are included for NH_2^- . The corresponding Dyson orbitals are shown in the top left corners.	45

3.3	Absolute cross-sections for photoionization from He, Ne, Ar, and H ₂ . Red dots are experimental cross-sections. Black and blue curves denote cross-sections computed using PWs and CWs, respectively. FCFs are included for H ₂ . For neon and argon, the aug-cc-pV6Z basis set was employed. The corresponding Dyson orbitals are shown in the top right corners.	47
3.4	Absolute partial cross-sections for the three lowest ionized states of water, and the total absolute cross-section (excluding contributions from the core-ionized state). Red dots are the experimental cross-sections. Black and blue curves denote the cross-sections computed using PWs and CWs, respectively. FCFs are not included.	48
3.5	Left: Absolute cross-sections for formaldehyde photoionization. The experimental cross-section are shown as red dots. The computed values are shown by black (PW), blue (CW with Z=+1), and orange (CW with Z=+0.25). All computed curves include FCFs. Right: The cross-sections (without FCFs) using different values of Z.	49
3.6	Absolute cross-sections for photoionization of ethylene, acetylene, 1-butene, 1-butyne, methanol, and propyne. For ethylene, two ionized states are accessed. The experimental cross-sections are shown as red dots. The computed values are shown using PW (black), CW (blue), and CW with a charge that gives the best fit with experiment (orange, if a good fit is not already obtained with PWs or CWs). All computed curves include FCFs. The Dyson orbitals and the center of expansion of the PW or CW (yellow circle) are also shown.	50
3.7	Coulomb radial functions for $l=0\text{--}5$ and for two different wave vector values, $k=0.068$ a.u. ($E_k=0.0625$ eV) and 0.271 a.u. ($E_k=1.0$ eV). . . .	55
3.8	Mulliken charges (with hydrogen charges summed onto heavy atoms) for (a) formaldehyde, (b) <i>cis</i> -2-butene, (c) propene, (d) ethylene, (e) acetylene, (f) 1-butene, (g) 1-butyne, (h) methanol, (i) propyne. The blue spheres show the centers of the expansion of the photoelectron wave function.	56
3.9	Absolute cross-sections for photoionization of propene and <i>cis</i> -2-butene. The experimental cross-sections are shown as red dots. The computed values are shown using plane wave (black), Coulomb wave (blue), and Coulomb wave with a charge that gives the best fit with experiment (orange, if a good fit is not already obtained with Coulomb or plane waves). The computed curves include FCFs. Note that our calculations indicate that the second ionized state of propene has vanishing FCFs and, therefore, does not contribute to the cross section. The state shown in this figure is the third ionized state of propene. The Dyson orbitals and the center of expansion of the plane or Coulomb wave (yellow circle) are also shown.	57

3.10	Absolute cross-sections for ethylene, acetylene, 1-butene, 1-butyne, methanol, and propyne. The computed values use a plane wave (black), Coulomb wave (blue), and a Coulomb wave with the charge that gives the best fit to the experiment (orange), if a good fit is not already obtained with Coulomb or plane waves. Solid and dashed lines denote the cross-sections computed with and without FCFs, respectively.	58
3.11	Coulomb radial functions for $l=1$ and for $k=0.271$ a.u. ($E_k=1.0$ eV) with varying Z. Black line shows a cut along the left Dyson orbital for formaldehyde in the x -direction (as shown in the figure). The value of the Dyson orbital is multiplied by x to give $r_x\phi_{IF}^d$ and magnified by a factor of 4 for clarity. As one can see, $l=0.4-0.6$ provide the biggest contribution to the cross-sections for formaldehyde.	59
3.12	The value of Eq. (3.11) computed for CW with different values of Z using displaced point-charge Coulomb potential. Two values of d are considered: one corresponding to placing the charge on the carbon atom (dashed lines) and one at the distance of the hydrogens (solid lines). For both models, we consider Coulomb functions with different k spanning a 40-fold change in kinetic energy.	62
4.1	Dyson orbitals and the respective vertical ionization energies (eV) for the four lowest electronic states of bare sodium and $\text{Na}(\text{NH}_3)_n$, $n=1-3$, computed using the EOM-EA-CCSD/aug-cc-pVDZ wave functions. . .	72
4.2	Dependence of vertical ionization energies on cluster size for the four lowest electronic states of bare sodium, $\text{Na}(\text{NH}_3)_n$, $n=1-10$, and $\text{Na}(\text{DME})_m$, $m=1-5$; EOM-EA-CCSD/aug-cc-pVDZ. The results for $\text{Na}(\text{DME})_{6,7}$ were computed with a smaller basis and reduced orbital space (see text). . .	87
4.3	The effect of electron correlation on the composition of the the first Dyson orbital in $\text{Na}(\text{NH}_3)_n$, $n=0-10$, and $\text{Na}(\text{DME})_m$, $m=0-5$; EOM-EA-CCSD/aug-cc-pVDZ. The values for $\text{Na}(\text{DME})_{6,7}$ were computed with a smaller basis and reduced orbital space (see text). $w(LUMO)$ is the weight of the Hartree-Fock LUMO in the normalized EOM-EA-CCSD Dyson orbital.	88
4.4	Dependence of sizes of Dyson orbitals, \bar{R}^d , on cluster size for the four lowest electronic states of $\text{Na}(\text{NH}_3)_n$, $n=0-10$, and $\text{Na}(\text{DME})_m$, $m=0-5$; EOM-EA-CCSD/aug-cc-pVDZ. The results for $\text{Na}(\text{DME})_{6,7}$ were computed with a smaller basis and reduced orbital space (see text).	89
4.5	Effect of the solvent on dipole moments and the distance between Na and the centroid of Dyson orbitals, d_{eh} , for the lowest electronic state of $\text{Na}(\text{NH}_3)_{0-10}$ and $\text{Na}(\text{DME})_{0-4}$; EOM-EA-CCSD/aug-cc-pVDZ. The results for $\text{Na}(\text{DME})_{5-7}$ were computed with a smaller basis and reduced orbital space (see text).	91

4.6	Dipole moments and the distance between Na and the centroid of Dyson orbitals, d_{eh} , for the four lowest electronic states of $\text{Na}(\text{NH}_3)_n$, $n=0-10$, and $\text{Na}(\text{DME})_m$, $m=0-5$; EOM-EA-CCSD/aug-cc-pVDZ. A line with slope=1 is plotted to guide the eye.	92
4.7	Difference dipole moments and distance between Na and the centroid of Dyson orbitals, d_{eh} , for the four lowest electronic states of $\text{Na}(\text{NH}_3)_n$, $n=0-10$, and $\text{Na}(\text{DME})_m$, $m=0-5$; EOM-EA-CCSD/aug-cc-pVDZ. A line with slope=1 is plotted to guide the eye.	93
4.8	The weight of p_0 amplitude in the outgoing waves at $h\nu=4.66$ eV. $\text{Na}(\text{NH}_3)_n$, $n=0-10$, and $\text{Na}(\text{DME})_m$, $m=0-5$; EOM-EA-CCSD/aug-cc-pVDZ. The results for $\text{Na}(\text{DME})_{6,7}$ were computed with a smaller basis and reduced orbital space (see text).	94
4.9	Snapshots along the equilibrium trajectory for $\text{Na}(\text{NH}_3)_6$. The respective VIE (eV), \bar{R}^d (bohr), and d_{eh} (bohr) are shown for each snapshot. The first picture corresponds to the minimum-energy structure.	95
4.10	Dependence of anisotropy parameter on photon energy at the minimal-energy structure compared with equilibrium trajectory average (computed by averaging β over 21 snapshots) for $\text{Na}(\text{NH}_3)_4$, left, and $\text{Na}(\text{NH}_3)_6$, right.	96
4.11	Snapshots along the equilibrium trajectory for $\text{Na}(\text{DME})_6$. The respective dipole moments (Debay) and \bar{R}^d (bohr) are shown for each snapshot. The first picture corresponds to the minimum-energy structure. All orbitals are shown with the same isovalue of 0.008.	98
4.12	Dyson orbitals for $\text{Na}(\text{DME})_3$ computed with EOM-EA-CCSD (left), $\omega\text{B97X-D}/\text{Koopmans}'$ (middle), and B3LYP/Koopmans' (right). Orbitals are shown with the same isovalue of 0.025. The orbitals are computed using the aug-cc-pVDZ and 6-31+G(d) basis sets for EOM and DFTs, respectively.	98
4.13	Sizes of Dyson orbitals and the distance between their centroids and $\text{Na}^{\delta+}$ for $\text{Na}(\text{NH}_3)_n$, $n=1-10$, and $\text{Na}(\text{DME})_m$, $m=1-7$; at the EOM-EA-CCSD/aug-cc-pVDZ (smaller basis and reduced orbital space for $m=6-7$, see text), $\omega\text{B97X-D}/6-31+G(d)$, CAM-B3LYP/6-31+G(d), B3LYP/6-31+G(d), and HF/6-31+G(d) levels of theory.	102
4.14	Anisotropy parameters (upper panel) and total cross-sections (lower panel) for different cluster sizes at energy of 4.66 eV computed using the EOM-EA-CCSD Dyson orbitals and Koopmans' theorem (DFT or HF SOMO).	105
4.15	The weight of the p_0 amplitude in the outgoing waves at $h\nu=4.66$ eV. $\text{Na}(\text{NH}_3)_n$, $n=0-10$, and $\text{Na}(\text{DME})_m$, $m=0-7$; EOM-EA-CCSD/aug-cc-pVDZ (smaller basis and reduced orbital space for $m=6-7$, see text) versus DFT/6-31+G(d) and HF/6-31+G(d).	106

4.16 Optimizing effective core charge Z for the outgoing p -wave with $E_k=0.5$ eV, 1.5 eV, and 2.5 eV.	111
4.17 Dependence of anisotropy parameters and total cross-sections on photon energy for different values of effective charge Z for Na(NH ₃) (upper panels) and Na(DME) (lower panels).	112
4.18 Dependence of anisotropy parameters and total cross-sections on photon energy and basis sets for Na(NH ₃).	112
4.19 The effect of using reduced basis set and virtual orbital space on β and σ for Na(DME) ₅ . FC denotes the EOM-EA-CCSD/aug-cc-pVDZ calculations with frozen core orbitals. FV denotes calculations with 31 frozen virtual orbitals. FV+basis denotes calculations with 31 frozen virtual orbitals and reduced basis set: aug-cc-pVDZ on heavy atoms and cc-pVDZ on H.	113
4.20 The effect of the basis set on β and σ for Na(NH ₃) ₅ computed with ωB97X-D.	113
4.21 Dependence of states' size, ΔR^{Ψ} , on cluster size for the four lowest electronic states of Na(NH ₃) _n , $n=0-10$, and Na(DME) _m , $m=0-4$, at the EOM-EA-CCSD/aug-cc-pVDZ level of theory.	114
4.22 Anisotropy parameters and total cross-sections computed at different snapshots from the equilibrium trajectory of Na(NH ₃). EOM-EA-CCSD/aug-cc-pVDZ.	115
4.23 Anisotropy parameters and total cross-sections computed at different snapshots from the equilibrium trajectory of Na(DME). EOM-EA-CCSD/aug-cc-pVDZ.	115
4.24 Anisotropy parameters and total cross-sections computed at different snapshots from the equilibrium trajectory of Na(NH ₃) ₄ . EOM-EA-CCSD/aug-cc-pVDZ.	116
4.25 Anisotropy parameters and total cross-sections computed at different snapshots from the equilibrium trajectory of Na(NH ₃) ₆ . EOM-EA-CCSD/aug-cc-pVDZ.	116
4.26 Anisotropy parameters and total cross-sections computed at different snapshots from the equilibrium trajectory of Na(DME) ₄ . EOM-EA-CCSD/aug-cc-pVDZ.	117
4.27 Anisotropy parameters and total cross-sections computed at different snapshots from the equilibrium trajectory of Na(DME) ₆ . ωB97X-D/6-31+G(d).	117
4.28 Anisotropy parameters and total cross-sections computed using the EOM-EA-CCSD Dyson orbitals and Koopmans' theorem (Kohn-Sham and Hartree-Fock SOMOs) for Na(NH ₃) (upper panel) and Na(DME) (lower panel).	120

4.29	Anisotropy parameters and total cross-sections computed using the EOM-EA-CCSD Dyson orbitals and Koopmans' theorem (Kohn-Sham and Hartree-Fock SOMOs) for Na(NH ₃) ₂ (upper panel) and Na(DME) ₂ (lower panel).	121
4.30	Anisotropy parameters and total cross-sections computed using the EOM-EA-CCSD Dyson orbitals and Koopmans' theorem (Kohn-Sham and Hartree-Fock SOMOs) for Na(NH ₃) ₃ (upper panel) and Na(DME) ₃ (lower panel).	122
4.31	Anisotropy parameters and total cross-sections computed using the EOM-EA-CCSD Dyson orbitals and Koopmans' theorem (Kohn-Sham and Hartree-Fock SOMOs) for Na(NH ₃) ₄ (upper panel) and Na(DME) ₄ (lower panel).	123
4.32	Anisotropy parameters and total cross-sections computed using the EOM-EA-CCSD Dyson orbitals and Koopmans' theorem (Kohn-Sham and Hartree-Fock SOMOs) for Na(NH ₃) ₅ (upper panel) and Na(DME) ₅ (lower panel).	124
4.33	Anisotropy parameters and total cross-sections computed using the EOM-EA-CCSD Dyson orbitals and Koopmans' theorem (Kohn-Sham and Hartree-Fock SOMOs) for Na(NH ₃) ₆ (upper panel) and Na(DME) ₆ (lower panel).	125
4.34	Anisotropy parameters and total cross-sections computed using the EOM-EA-CCSD Dyson orbitals and Koopmans' theorem (Kohn-Sham and Hartree-Fock SOMOs) for Na(NH ₃) ₇ (upper panel) and Na(DME) ₇ (lower panel).	126
4.35	Anisotropy parameters and total cross-sections computed using the EOM-EA-CCSD Dyson orbitals and Koopmans' theorem (Kohn-Sham and Hartree-Fock SOMOs) for Na(NH ₃) ₈	126
4.36	Anisotropy parameters and total cross-sections computed using the EOM-EA-CCSD Dyson orbitals and Koopmans' theorem (Kohn-Sham and Hartree-Fock SOMOs) for Na(NH ₃) ₉	127
4.37	Anisotropy parameters and total cross-sections computed using the EOM-EA-CCSD Dyson orbitals and Koopmans' theorem (Kohn-Sham and Hartree-Fock SOMOs) for Na(NH ₃) ₁₀	127
5.1	Different forms of arginine.	133
5.2	Isomers of arginine considered in this work. <i>ti</i> denotes tautomeric conformers, <i>c3</i> denotes canonical form, and <i>zj</i> denotes zwitterionic conformers.	135
5.3	Energies and Dyson orbitals of different isomers of arginine at the Franck-Condon (left columns) and relaxed (right columns) structures.	138
5.4	Stick spectra showing the lowest nine VIEs and the lowest AIE for <i>t1</i> , <i>t2</i> , <i>c3</i> , <i>t6</i> , and <i>z8</i> isomers of arginine.	139

5.5	Arginine with closest hydrogen-bonded water molecules. Left to right: one closest water molecule, three donor water molecules near the carboxyl group, three acceptor water molecules – in the upper row; six (a combination of three donor and three acceptor) water molecules, seven (six and one closest), ten (seven and three closest) molecules – in the lower row.	141
5.6	Dyson orbitals corresponding to the 9th ionized state computed at QM/MM level for arginine with different number of water molecules in QM. . . .	142
5.7	Dyson orbitals corresponding to the first ionized state computed at QM/MM level for arginine with different number of water molecules in QM. . . .	143
5.8	Dyson orbitals corresponding to the first ionized state of hydrated or micro-hydrated arginine with 7 water molecules. From left to right: QM/MM, QM/CPCM, QM only.	144
5.9	Computed photoelectron spectra of zwitterionic and protonated arginine in aqueous solution.	145
6.1	Second Dyson orbital for the bare (top) and doubly hydrated (bottom) phenol and phenolate.	153
6.2	Cartoon (a) and STM image (b) of CoPC and its anions adsorbed on a h-BN monolayer on Ir(111). Inset in (a) shows the chemical structure of CoPC.	154

Abstract

Photoionization and photodetachment spectroscopy are important experimental tools for studying electronic structure and dynamics. However, connecting the experimental observables with the underlying quantum mechanical picture and even interpretation of the experimental results are not straightforward without theoretical modeling. Despite great progress in computational methods, the most common analysis tools are still based on the Koopmans' theorem, employing canonical Hartree-Fock or Kohn-Sham orbitals. Although this approach often captures a qualitative picture, it has a limited predictive power, especially for systems beyond closed-shell species.

In Chapter 2, we present a derivation of the generalized one-electron wave function that provides a quantitative yet simple and transparent description of the electronic structure part of the problem. This description is applicable to a wide variety of possible experimental setups. We employ a high-level robust electronic structure approach, equation-of-motion coupled-cluster family of methods, and describe a black-box implementation for computing Dyson orbitals, an overlap of many-electron wave functions that differ by one electron. Our choice of electronic structure method enables analyzing multiple transitions from one calculation and provides a direct connection to Koopmans' theorem predictions.

In Chapter 3, we analyze limits of the simplest single-center expansion approach for modeling outgoing electron by comparing computed cross-sections with reliable experimental data. We show that the plane-wave description is valid for photodetachment from molecular anions, but molecular photoionization cross-section profiles often contain features observed both in plane-wave and in Coulomb-wave descriptions. We then proceed to utilize Coulomb waves with partial charge to show that a single fitted parameter makes it possible to quantitatively reproduce absolute cross-sections in a wide range of photon energies. Finally, we propose a simplified one-dimensional model for obtaining partial charge without fitting to experimental data.

In Chapter 4, we apply the formalism developed in Chapter 2 to describe solvated electrons. Our approach enables implicit inclusion of the effects of the bath (solvent) within an orbital (i.e., one-electron) picture. Analysis of Dyson orbital shapes suggests that in small sodium-doped ammonia and dimethyl ether clusters, the electron is surface-bound. The analysis of the computed properties reveals the effect of hydrogen bonding in solvent on stabilization of the charge-separated system. We further explain the experimentally observed trend in anisotropy parameter dependence on cluster size, including the appearance of “magic numbers”. We also make connections to popular mean-field orbital descriptions and illustrate the consequences of self-interaction error of Kohn-Sham density functional theory in this type of systems.

Finally, in Chapter 5 we consider photoionization of arginine in the gas phase and in water. This amino acid has long and complex side chain, which participates in multiple non-covalent inter- and intramolecular interactions. Our calculations suggest that while the photoionization in the gas phase results in fast fragmentation of the cations, the solvation stabilizes them, changing the photoionization picture qualitatively.

Chapter 1: Introduction and overview

1.1 Photoelectron spectroscopy and imaging

Photoionization and photodetachment experiments are widely used in physics and chemistry^{1–3}. Among many applications, they are valuable tools for characterization of transient reaction intermediates. Compared to conventional methods of electron scattering⁴ and electron transmission spectroscopy^{5,6}, photodetachment introduces a benefit of higher spectroscopic resolution. In addition, photodetachment can be employed to create transient species (such as molecules at transition states) that are otherwise unstable, thus enabling determination of their properties and spectroscopic signatures^{7–9}. Furthermore, photodetachment experiments utilize initially charged species and can be coupled with mass-spectroscopic pre-selection or various ion traps for precise speciation control¹⁰. The basics of photodetachment spectroscopy is schematically shown in Fig. 1.1; photoionization can be described by swapping labels M^- to M and M to M^+ .

In the simplest setup, a photoionization or photodetachment experiment delivers information about energy levels of the system and, indirectly, structural changes in the target ionized/detached states with respect to the initial one (as seen in Fig. 1.1, relative shape of the potential energy surface determines the observed progression). By using special detectors, one can detect photoelectrons in an angular-resolved manner^{11–13}, gaining additional insights into the nature of the underlying changes in wave functions.

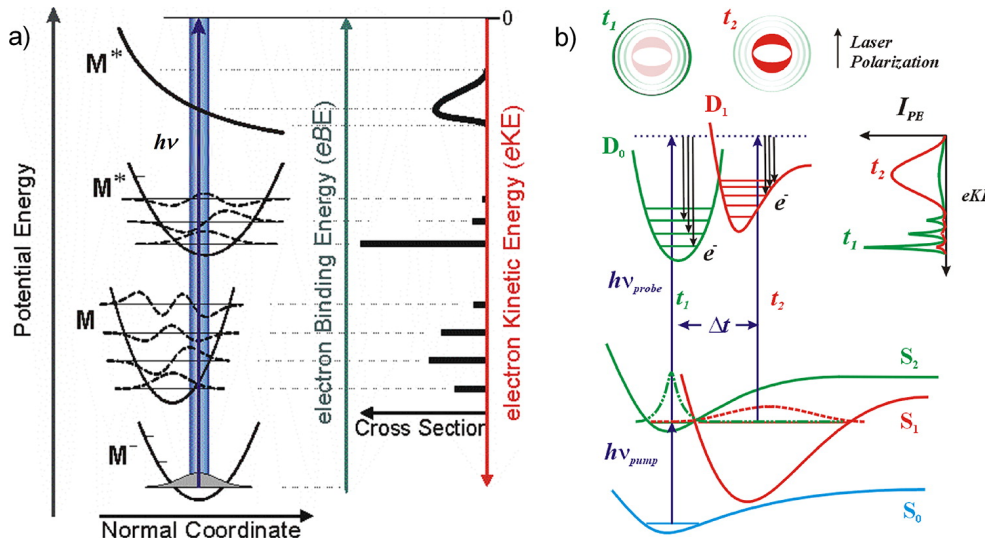


Figure 1.1: Various flavors of photoelectron spectroscopy. (a) Origin of photodetachment spectra. (b) Time-resolved photoelectron spectroscopy (bottom) and imaging (top). Adapted with permission from Ref. 135. Copyright 2012 American Chemical Society.

Further, pump-probe setup enables investigation of time dependent processes^{14–18}, providing a tool for experimentally monitoring excited state dynamics. Time-resolved photoelectron imaging (TRPEI) offers an additional advantage of being able to distinguish different channels with close ionization energies, such as, for example, ultrafast internal conversion in pyrazine¹⁹. The basic idea behind time-resolved photoelectron spectroscopy (TRPES) and TRPEI is illustrated in the right panel of Fig. 1.1.

Insights from theoretical modeling allow one to connect experimental observations with the underlying electronic-structure changes. Modeling spectra entails computing energies and intensities (as well as angular positions, in the case of photoelectron imaging, PEI). Calculation of relevant energies is relatively well-established²⁰ and can be carried out using numerous methods, ranging from Koopmans' theorem, to ΔE approaches (in which ionization energy, IE, is computed as a difference of total energies), to direct calculations of energy differences by equation-of-motion coupled-cluster²¹ (EOM-CC),

electron propagator²², or Green’s function²³ formalisms. Computing properties (i.e., cross-sections) is less developed. At the same time, measuring absolute cross-sections experimentally is very challenging. In general, it requires special setups for detecting both the species under study and a reference compound^{24–26}. For photodetachment, it is also possible to conduct measurements in ion traps apparati, as described in Refs. 27,28, providing an opportunity to perform state-selected studies²⁹ for specific rotational and vibrational states of target species. Total cross-sections at different photon energies are needed in many applications: for planning and interpreting mass-spectroscopic experiments, as parameters in kinetic models of atmospheric and interstellar chemistry^{30–36}, and for interpretation of photoionization and photodetachment spectra. In some TRPES experiments, having data on total cross-sections is particularly important owing to similar timescales of excited-state processes in different conformers³⁷. Differential cross-sections are needed to analyze the results of photoelectron imaging experiments.

In the absence of reliable theory, simplified models are often employed, commonly based on uncorrelated Hartree-Fock (HF) and Koopmans’ theorem predictions, same cross-section approximation³⁸, atomic and orbital hybridization-based representations^{39,40} of photoelectron angular distributions (PADs). Robust and easy-to-use theoretical approach is thus highly desired for modeling photodetachment/photoionization cross-sections. The starting point is the photoelectron matrix element, which describes probability of forming the final many-electron bound state Ψ^F and an outgoing electron with energy and direction determined by wave vector \mathbf{k} from the initial many-electron state Ψ^I . In the dipole approximation, the photoelectron matrix element has the following form:

$$|D_k^{IF}|^2 = |\langle \Psi_N^I | r | \Psi_{N-1}^F \Psi_k^{el} \rangle|^2, \quad (1.1)$$

where r is the dipole moment operator and Ψ_k^{el} is the wave function of the ejected electron.

There are several ways of computing D_k^{IF} , which differ in how they tackle Ψ_k^{el} . The Stieltjes imaging^{41,42} avoids explicit representation of Ψ_k^{el} . Instead, it utilizes an electronic structure method capable of describing excited electronic states and, by performing a series of calculations with highly diffuse basis sets, uses discretized representation of the continuum to reconstruct the state of the ejected electron. The Coulomb and exchange/correlation interactions of the outgoing electron with the remaining core are handled explicitly by this approach. The implementations based on linear-response coupled-cluster with single and double substitutions^{43,44} (LR-CCSD) and algebraic diagrammic construction^{45,46} (ADC) electronic structure methods have been reported; however, Stieltjes imaging is expensive due to basis set requirements (it was suggested⁴⁶ that using mixed Gaussian and B-splines basis is preferable) and is plagued by numerical convergence issues.

A practical alternative for computing photoelectron matrix element, Eq. (1.1), is to assume strong orthogonality and separate bound and outgoing electron states such that they can be described independently of each other. This gives rise to the following expression for the photoelectron matrix element:

$$D_k^{IF} = u \langle \Phi_{IF}^d | r | \Psi_k^{el} \rangle, \quad (1.2)$$

where u is a unit vector in the direction of the polarization of light. Here we contracted two many-electron wave functions, Ψ^I and Ψ^F , into a one-electron quantity (called

Dyson orbital), which represents in a compact way the difference between the initial and the final states:

$$\phi_{IF}^d(1) = \sqrt{N} \int \Psi_N^I(1, \dots, n) \Psi_{N-1}^F(2, \dots, n) d2 \dots dn. \quad (1.3)$$

This definition can be applied to any type of many-electron wave functions. For instance, using HF wave functions constructed from the canonical orbitals of one of the states, we recover Koopmans' theorem. To include electron correlation and orbital relaxation effects, which are neglected within Koopmans' theorem, one can use⁴⁷ density functional theory, DFT (note that for a hypothetic exact functional highest occupied molecular orbital (HOMO) within DFT is the exact Dyson orbital^{48,49}) or employ extended Koopmans' theorem⁵⁰. Other possibilities include using either⁵¹ complete active space self-consistent-field/complete active space configuration interaction (CASSCF/CAS-CI) or⁵² multistate second order perturbation theory (MS-PT2) treatment with an artificial restriction of using molecular orbital (MO) basis of the neutral molecule for constructing determinant expansion of both initial and final states. Alternatively, one can use linear-response time-dependent density functional theory (LR-TDDFT), computing overlaps of the molecular orbitals for neutral and cationic species^{19,53,54}, or direct methods such as electron propagator^{55–58} or EOM^{59,60}. The last two approaches are the most rigorous and, therefore, preferable when affordable. Propagator-based methods with the diagonal approximation (for self-energy operator matrix) and EOM-CC offer an advantage in the analysis of the Dyson orbitals by providing straightforward interpretation in terms of the canonical HF orbitals. EOM-CC methods feature conceptually transparent formulation and are robust, black box, numerically stable, single-reference, and capable of describing multiple states (i.e., closed- and open-shell with various multiplicities, ground and excited electronic states, etc.) in a balanced manner. Until present work, EOM-CC

Dyson orbitals were only implemented as transition densities in a pilot code^{59,60} using diffuse orbital trick⁶¹. The resulting code was slow and suffered from convergence problems. As part of this thesis, a proper implementation of Dyson orbitals within EOM-CC formalism was developed.

The second quantity entering Eq. (1.1) is wave function of the outgoing electron. There are several advanced theories of molecular photoionization, which are capable of reproducing experimental data⁶², but their applications are limited by the level of electron correlation in compatible electronic structure theories^{63–66}. More practical and simpler photoelectron models utilize single-center expansion, originating in the Cooper-Zare model⁶⁷, which was subsequently extended to molecular systems^{60,68}. These simple models are capable of explaining experimentally observed trends in cross-sections and angular distributions^{2,69–74}. Han and Yarkony pointed out that the strong orthogonality assumption might be too extreme⁷⁵ and developed a theoretical framework for determining the state of the ejected electron using the Lippmann-Schwinger equation⁷⁶, which accounts for non-orthogonality and exchange interactions with the core^{75,77–79}. However, there is no practical implementation of this formalism yet. Practical implementation of single-center expansion using plain or Coulomb-type outgoing waves, discussed above, is available in the *ezDyson* code⁸⁰. These descriptions are exact only in the cases of atomic photodetachment and photoionization, yet they clearly capture the physics of the photoejection processes in molecules.

Having photoelectron matrix element, Eq. (1.1), computed, one can obtain differential cross-section as

$$\frac{d\sigma}{d\Omega_k} = \frac{4\pi^2}{c} \cdot E \cdot |D_k^{IF}(\theta, \phi)|^2 \quad (1.4)$$

Integrating by angle ϕ , one obtains PAD, which, in turn, can be integrated by θ to yield the total cross-sections.

1.2 Solvent effects in photoionization and photodetachment

Understanding solvent effects is of fundamental importance. It is critical for modeling transient reaction intermediates, as most of chemistry and electrochemistry happen in solutions. Therefore, it is desirable to extend the techniques of photoelectron spectroscopy and imaging to study the effect of solvation on electronic structure (and dynamics) of solutes. The simplest yet very important type of experiments, which reveals underlying elementary chemical processes in condensed phase, considers⁸¹ clusters of solute with a single solvent molecule. As a starting point, one can consider different solvent molecules with the same solute and analyze differences in the spectra and images^{2,82}. Already at this level new – with respect to the isolated solute – phenomena can be observed, as shown in Fig. 1.2: shifts of IEs, changes in branching ratios of photodetachment channels, deviations from atomic-type PADs, and signatures of “thermal electrons” (i.e., indirect photodetachment channels due to the presence of solvent, see the discussion in Ref. 2 and references therein).

On the other end of the range of solvation experiments, there are studies in liquid microjets^{83,84}, which capture bulk properties. However, the experimental setup is complicated due to a limited penetration depth of photoelectrons^{85–87} and the interplay between surface effects^{54,88} and bulk solvation. In between these two limits, there are studies of microsolvated clusters, which enable observation of the dependence of various properties on cluster size^{81,89–91}. By means of extrapolation^{92–94}, these measurements provide an insight into bulk liquid and into the fundamental boundary between gas-phase clusters and solutions.

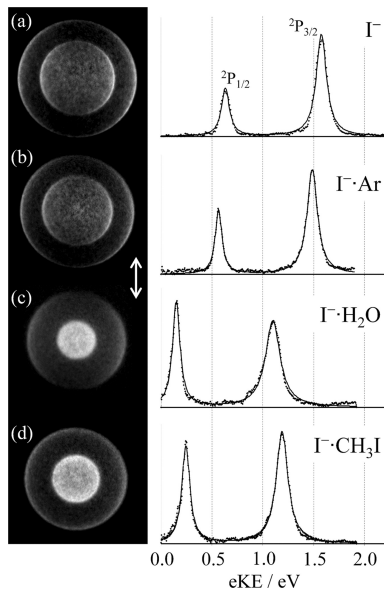


Figure 1.2: The effect of single solvent molecule forming a complex with I^- on PADs (left) as well as line positions and relative intensities in the photoelectron spectra (right). Adapted with permission from Ref. 2.

Although computational studies of solvated systems are more challenging than those in vacuum, they can provide unique insights. From the theoretical point of view, solvent effects can be divided⁹⁵ into direct (i.e., polarization of solute by solvent or specific solvent-solute interactions, such as hydrogen bonding) and indirect, caused by the changes in the geometry of solute upon solvation. Computational modeling allows one to discriminate between these effects as well as to quantify the contributions of various interactions into solvent-induced changes of properties. Intermolecular interactions can be divided into Coulomb, polarization, exchange-repulsion, dispersion, and charge-transfer⁹⁶. Since photoionization and photodetachment involve charged species either as an initial or as a final state, the Coulomb part dominates solvent-induced shifts, followed by polarization contribution. The latter was shown⁹⁷ to contribute as much as 15% into solvation energies. In photodetachment, charge transfer to solvent (CTTS) followed by autodetachment can also become operational, as was

shown experimentally^{98,99}. Theoretical approaches for describing solvent effects can be broadly divided into dielectric continuum models^{100–106} (reasonable for neutral species, but producing large errors for charged ones^{107–110}), quantum mechanics–molecular mechanics (QM/MM) approach^{111,112}, including quantum mechanics–effective fragment potential^{113–117} (QM/EFP), and explicit quantum mechanical treatment of solvent^{118,119}. The latter requires a large number of solvent shells for properties to converge^{116,120}, but it can be combined with the other two approaches to improve their performance^{121,122}. There are also developments in the area of density embedding (QM/QM type) schemes^{123,124}. To account for indirect solvent effects and finite temperature, equilibrium structural fluctuations are sampled via molecular dynamics (MD) simulations. The properties are subsequently averaged over the MD snapshots, giving rise to solvent-induced broadening.

Obviously, approximations and trade-offs are needed to make simulations feasible. Often, the computed properties are shifted for comparison with the experimental results. On the other hand, experiments in solutions entail considerable line broadening and often probe more than one microsolvated cluster (rather, a distribution of cluster sizes). Given the inherent complexity of the problem and the limits of both experimental and computational approaches, the best strategy is to combine theoretical and experimental efforts, in order to reveal the effects of solvation on IEs and the fundamental underlying mechanisms.

Solvated electrons represent an extreme example of solvated systems. In this case, post-ionization/detachment or post-excitation relaxation process emerge solely due to collective behavior of solvent molecules. Furthermore, adiabatic ionization energy (AIE) and adiabatic detachment energy (ADE) of solvated electrons have somewhat different physical meaning, since by removing an electron, the solute, one creates a

qualitatively different system: pure solvent.¹²⁵ Observed first as a mysterious blue color upon dissolving alkali metals in ammonia¹²⁶ and subsequently as a bronze-colored metallic state at higher metal concentrations¹²⁷, solvated electrons were later found in many processes involving electron generation and/or transfer in the presence of solvent, such as electrochemistry¹²⁸, biological radiation damage^{129–131}, atmospheric aerosol nucleation¹³², a family of mild reduction reactions in organic chemistry¹³³, as well as radiolysis of water, ammonia, alcohols, and amines¹³⁴. There are two type of systems containing solvated electrons: neat clusters¹³⁵ and (metal-)doped clusters¹³⁶. The former have been thoroughly investigated experimentally, both in liquid jets and in anionic clusters, and there are numerous theoretical studies on the subject, as reviewed in Refs. 132, 135, 137 and Refs. 138–140, respectively. The combined experimental and theoretical efforts revealed the existence of several isomers shown in Fig. 1.3: surface-bound, cavity-type, and partially embedded; dipole-bound anions can be observed under certain conditions, too. The extrapolation by the cluster size^{141–144}, which is shown in Fig. 1.4, results in detachment energies close to the bulk values.

In contrast, doped clusters hitherto received rather limited theoretical attention^{149, 150}. Modeling of solvated electrons in these systems is highly desirable to complement and explain experimental observations^{151, 152}. EOM-CC Dyson orbitals, which represent correlated one-electron wave function and implicitly include an effect of remaining $N - 1$ electrons, provide an ideal tool for studying solvated electrons (i.e., a system with one electronic degree of freedom strongly affected by the bath) in small solvent clusters at high and robust level of theory.

In this thesis, we present a theoretical approach for modeling photoionization and photodetachment processes, with a special emphasis on the electronic structure part of the problem. Chapter 2 presents the derivation of the EOM-CC Dyson orbitals and the

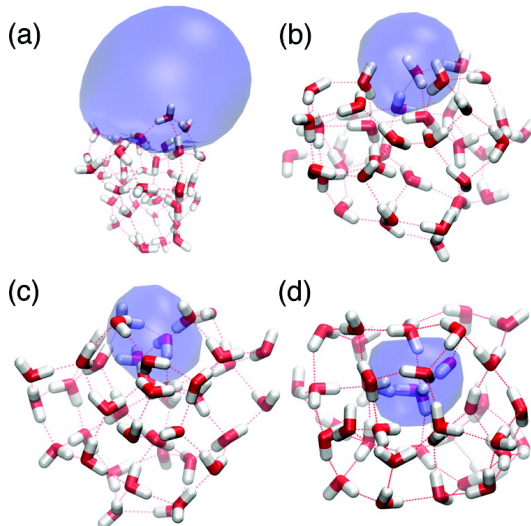


Figure 1.3: Examples of the four main types of solvated electrons observed in $(\text{H}_2\text{O})_{40}$: (a) a dipole-bound surface isomer, (b) a surface isomer, (c) a partially embedded surface isomer, and (d) a cavity isomer. The isosurfaces encapsulate 70% of the electron density. Adapted with permission from Ref. 145. Copyright 2011 American Chemical Society.

implementation within the new generation of the EOM-CC codes in the Q-Chem electronic structure package¹⁵³. In Chapter 3, we discuss an extension of the single-center expansion approach to utilizing Coulomb waves with a partial charge. This considerably improves the performance of the model, allowing one to quantitatively reproduce the experimental values of total cross-sections in a wide range of photon energies. Chapter 4 presents theoretical insights into the nature of solvated electrons in sodium-doped clusters, revealing the influence of hydrogen bonds in solvent, explaining the existence of “magic numbers” in clusters, and performing an evaluation of performance of DFT functionals for reproducing physical properties of such systems. In Chapter 5 we consider an extreme case of solvent effect, namely, when behavior of the solute upon ionization is qualitatively different from that in the gas phase. Finally, Chapter 6 proposes further advancements in method development and prospective applications of the developed formalisms.

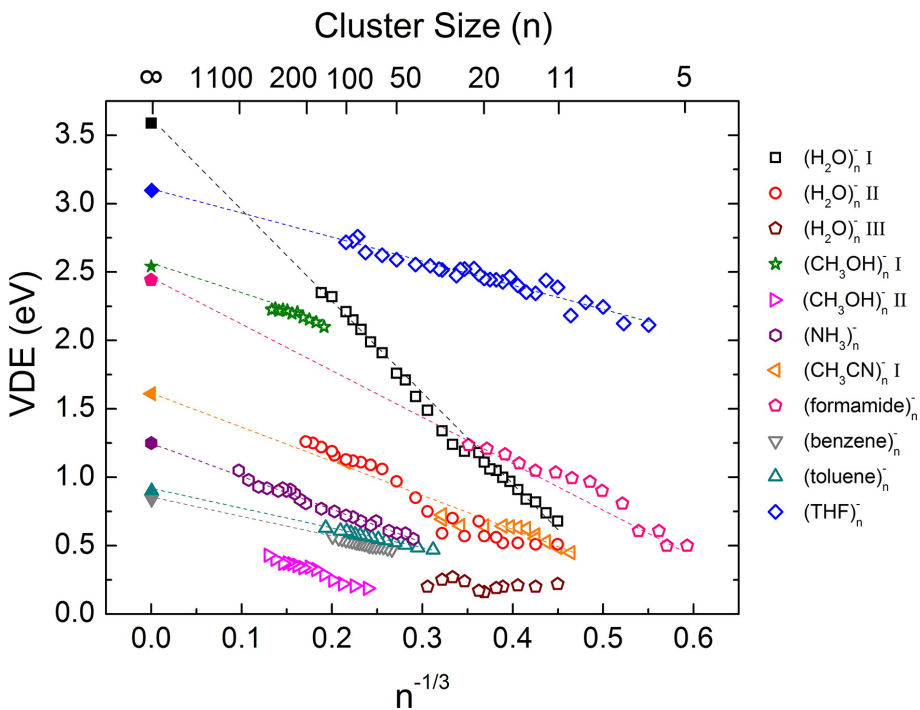


Figure 1.4: VDEs of solvated electrons in various solvent clusters as a function of cluster size. For water, three distinct isomeric series (labeled I, II, and III) were found¹⁴⁶; for methanol, two isomers (I and II) were detected¹⁴⁷. For acetonitrile, two isomers were observed¹⁴⁸, but only one is plotted here. Adapted with permission from Ref. 135. Copyright 2012 American Chemical Society.

1.3 Chapter 1 references

- [1] J. Simons. Detachment processes for molecular anions. In C.Y. Ng, editor, *Photoionization and Photodetachment*, volume 10, Part II of *Advanced Series in Physical Chemistry*. World Scientific Publishing Co., Singapore, 2000.
- [2] A. Sanov and R. Mabbs. Photoelectron imaging of negative ions. *Int. Rev. Phys. Chem.*, 27:53–85, 2008.
- [3] K.L. Reid. Picosecond time-resolved photoelectron spectroscopy as a means of gaining insight into mechanisms of intramolecular vibrational energy redistribution in excited states. *Int. Rev. Phys. Chem.*, 27:607–628, 2008.
- [4] D. J. Larson, C. J. Edge, R. E. Elmquist, N. B. Mansour, , and R. Trainham. Physics with negative ions in ion traps. *Phys. Scr.*, T22:183–190, 1988.
- [5] K. D. Jordan and P. D. Burrow. Temporary anion states of polyatomic hydrocarbons. *Chem. Rev.*, 87(3):557–588, 1987.
- [6] P. Burrow. Bibliography of studies in electron transmission spectroscopy, 2007. <http://digitalcommons.unl.edu/physicsburrow/6/>.
- [7] O. Welz, J.D. Savee, D.L. Osborn, S.S. Vasu, C.J. Percival, D.E. Shallcross, and C.A. Taatjes. Direct kinetic measurements of Criegee intermediate (CH_2OO) formed by reaction of CH_2I with O_2 . *Science*, 335:204–207, 2012.
- [8] D.M. Neumark. Probing the transition state with negative ion photodetachment: experiment and theory. *Phys. Chem. Chem. Phys.*, 7:433, 2005.
- [9] D.M. Neumark. Probing chemical dynamics with negative ions. *J. Chem. Phys.*, 125:132303, 2006.
- [10] A. R. McKay, M. E. Sanz, C. R. S. Mooney, R. S. Minns, E. M. Gill, and H. H. Fielding. Development of a new photoelectron spectroscopy instrument combining an electrospray ion source and photoelectron imaging. *Rev. Sci. Instrum.*, 81:123101, 2010.
- [11] D.W. Chandler and P.L. Houston. Two-dimensional imaging of state-selected photodissociation products detected by multiphoton ionization. *Annu. Rev. Phys. Chem.*, 87:1445–1447, 1987.
- [12] A.J.R. Heck and D.W. Chandler. Imaging techniques for the study of chemical reaction dynamics. *Annu. Rev. Phys. Chem.*, 46:335–372, 1995.

- [13] P.L. Houston. Snapshots of chemistry: Product imaging of molecular reactions. *Acc. Chem. Res.*, 28:453–460, 1995.
- [14] S. Ullrich, T. Schultz, M.Z. Zgierski, and A. Stolow. Electronic relaxation dynamics in DNA and RNA bases studied by time-resolved photoelectron spectroscopy. *Phys. Chem. Chem. Phys.*, 6:2796–2801, 2004.
- [15] D.M. Neumark. Time-resolved photoelectron spectroscopy of molecules and clusters. *Annu. Rev. Phys. Chem.*, 52:255–277, 2001.
- [16] A. Stolow, A.E. Bragg, and D.M. Neumark. Femtosecond time-resolved photoelectron spectroscopy. *Chem. Rev.*, 104:1719–1757, 2004.
- [17] T. Suzuki. Femtosecond time-resolved photoelectron imaging. *Annu. Rev. Phys. Chem.*, 57:555–592, 2006.
- [18] S. Lochbrunner, J.J. Larsen, J.P. Shaffer, M. Schmitt, T. Schultz, J.G. Underwood, and A. Stolow. Methods and applications of femtosecond time-resolved photoelectron spectroscopy. *J. Electron. Spectrosc. Relat. Phenom.*, 112(1-3):183–198, 2000.
- [19] G. Tomasello, A. Humeniuk, and R. Mitrić. Exploring ultrafast dynamics of pyrazine by time-resolved photoelectron imaging. *J. Phys. Chem. A*, 118(37):8437–8445, 2014.
- [20] J. Simons. Theoretical study of negative molecular ions. *Annu. Rev. Phys. Chem.*, 62:107–128, 2011.
- [21] A.I. Krylov. Equation-of-motion coupled-cluster methods for open-shell and electronically excited species: The hitchhiker’s guide to Fock space. *Annu. Rev. Phys. Chem.*, 59:433–462, 2008.
- [22] H.H. Corzo and J.V. Ortiz. Electron propagator theory: foundations and predictions. *Adv. Quantum Chem.*, 74:267–298, 2017.
- [23] A.R. Welden, J.J. Phillips, and D. Zgid. Ionization potentials and electron affinities from the extended Koopmans’ theorem in self-consistent Green’s function theory. *arXiv*, 2015. doi: arXiv:1505.05575.
- [24] B. Yang, J. Wang, T. A. Cool, N. Hansen, S. Skeen, and D. L. Osborn. Absolute photoionization cross-sections of some combustion intermediates. *Int. J. Mass Spectrom.*, 309:118–128, 2012.
- [25] M. Xie, Z. Zhou, Z. Wang, D. Chen, and F. Qi. Determination of absolute photoionization cross-sections of oxygenated hydrocarbons. *Int. J. Mass Spectrom.*, 293:28–33, 2010.

- [26] L.G. Dodson, L. Shen, J.D. Savee, N.C. Eddingsaas, O. Welz, C.A. Taatjes, D.L. Osborn, S.P. Sander, and M. Okumura. VUV photoionization cross sections of HO₂, H₂O₂, and H₂CO. *J. Phys. Chem. A*, 119:1279–1291, 2015.
- [27] S. S. Kumar, D. Hauser, R. Jindra, T. Best, S. Roucka, W. D. Geppert, T. J. Millar, and R. Wester. Photodetachment as a destruction mechanism for CN⁻ and C₃N⁻ anions in circumstellar envelopes. *Astrophys. J.*, 776:25, 2013.
- [28] T. Best, R. Otto, S. Trippel, P. Hlavenka, A. von Zastrow, S. Eisenbach, S. Jezouin, R. Wester, E. Vigren, M. Hamberg, and W. D. Geppert. Absolute photodetachment cross-section measurements for hydrocarbon chain anions. *Astrophys. J.*, 742:63, 2011.
- [29] S. Trippel, J. Mikosch, R. Berhane, R. Otto, M. Weidemuller, and R. Wester. Photodetachment of cold OH⁻ in a multipole ion trap. *Phys. Rev. Lett.*, 97:193003, 2006.
- [30] I. R. Slagle, F. Yamada, and D. Gutman. Kinetics of free radicals produced by infrared multiphoton-induced decompositions. 1. Reactions of allyl radicals with nitrogen dioxide and bromine. *J. Am. Chem. Soc.*, 103:149–153, 1981.
- [31] I. R. Slagle and D. Gutman. Kinetics of polyatomic free radicals produced by laser photolysis. 5. Study of the equilibrium methyl + oxygen = CH₃O₂ between 421 and 538 C. *J. Am. Chem. Soc.*, 107:5342–5347, 1985.
- [32] R. S. Timonen, E. Ratajczak, D. Gutman, and A. F. Wagner. The addition and dissociation reaction atomic hydrogen + carbon monoxide = oxomethyl. 2. Experimental studies and comparison with theory. *J. Phys. Chem.*, 91:5325–5332, 1987.
- [33] C. Fockenberg, H. J. Bernstein, G. E. Hall, J. T. Muckerman, J. M. Preses, T. J. Sears, and R. E. Weston. Repetitively sampled time-of-flight mass spectrometry for gas-phase kinetics studies. *Rev. Sci. Instrum.*, 70:3259–3264, 1999.
- [34] A. J. Eskola and R. S. Timonen. Kinetics of the reactions of vinyl radicals with molecular oxygen and chlorine at temperatures 200–362 K. *Phys. Chem. Chem. Phys.*, 5:2557–2561, 2003.
- [35] M. A. Blitz, A. Goddard, T. Ingham, and M. J. Pilling. Time-of-flight mass spectrometry for time-resolved measurements. *Rev. Sci. Instrum.*, 78:034103, 2007.
- [36] M. T. Baeza-Romero, M. A. Blitz, A. Goddard, and P. W. Seakins. Time-of-flight mass spectrometry for time-resolved measurements: Some developments and applications. *Int. J. Chem. Kinet.*, 44:532–545, 2012.

- [37] M. Ruckenbauer, S. Mai, P. Marquetand, and L. González. Revealing deactivation pathways hidden in time-resolved photoelectron spectra. *Sci. Rep.*, 6:35522, 2016.
- [38] J.W. Rabalais. *Principles of UltraViolet Photoelectron Spectroscopy*. John Wiley and Sons: New York, 1977.
- [39] A. Sanov. Laboratory-frame photoelectron angular distributions in anion photodetachment: Insight into electronic structure and intermolecular interactions. *Annu. Rev. Phys. Chem.*, 65:341–363, 2014.
- [40] D. Khuseynov, C.C. Blackstone, L.M. Culberson, and A. Sanov. Photoelectron angular distributions for states of any mixed character: An experiment-friendly model for atomic, molecular, and cluster anions. *J. Chem. Phys.*, 141:124312, 2014.
- [41] P.W. Langhoff. Stieltjes-Tchebycheff moment-theory approach to molecular photoionization studies. In V. McKoy T. Rescigno and B. Schneider, editors, *Electron Molecule and Photon Molecule Collisions*, pages 183–224. Plenum, New York, 1979.
- [42] I. Cacelli, R. Moccia, and A. Rizzo. Gaussian-type-orbital basis sets for the calculation of continuum properties in molecules: The differential photoionization cross section of molecular nitrogen. *Phys. Rev. A*, 57:1895–1905, 1998.
- [43] J. Cukras, P. Decleva, and S. Coriani. A coupled-cluster study of photodetachment cross sections of closed-shell anions. *J. Chem. Phys.*, 141:174315, 2014.
- [44] J. Cukras, S. Coriani, P. Decleva, O. Christiansen, and P. Norman. Photoionization cross section by Stieltjes imaging applied to coupled cluster Lanczos pseudo-spectra. *J. Chem. Phys.*, 139:094103, 2013.
- [45] M. Ruberti, R. Yun, K. Gokhberg, S. Kopelke, L.S. Cederbaum, F. Tarantelli, and V. Averbukh. Total molecular photoionization cross-sections by algebraic diagrammatic construction-Stieltjes-Lanczos method: Benchmark calculations. *J. Chem. Phys.*, 139:144107, 2013.
- [46] M. Ruberti, V. Averbukh, and P. Decleva. B-spline algebraic diagrammatic construction: Application to photoionization cross-sections and high-order harmonic generation. *J. Chem. Phys.*, 141:164126, 2014.
- [47] Y. Lin and C. Ning. Calculation of photodetachment cross sections and photoelectron angular distributions of negative ions using density functional theory. *J. Chem. Phys.*, 143:144310, 2015.

- [48] C.-O. Almbladh and U. von Barth. Exact results for the charge and spin densities, exchange-correlation potentials, and density-functional eigenvalues. *Phys. Rev. B*, 31:3231–3244, 1985.
- [49] M. Levy, J.P. Perdew, and V. Sahni. Exact differential equation for the density and ionization energy of a many-particle system. *Phys. Rev. A*, 30:2745–2748, 1984.
- [50] D. Vanfleteren, D.V. Neck, P.W. Ayers, R.C. Morrison, and P. Bultinck. Exact ionization potentials from wavefunction asymptotics: The extended Koopmans' theorem, revisited. *J. Chem. Phys.*, 130:194104, 2009.
- [51] H.R. Hudock, B.G. Levine, A.L. Thompson, H. Satzger, D. Townsend, N. Gador, S. Ulrich, A. Stolow, and T.J. Martínez. Ab initio molecular dynamics and time-resolved photoelectron spectroscopy of electronically excited uracil and thymine. *J. Phys. Chem. A*, 111:8500–8598, 2007.
- [52] T. Mori, W.J. Glover, M.S. Schuurman, and T.J. Martinez. Role of rydberg states in the photochemical dynamics of ethylene. *J. Phys. Chem. A*, 116:2808–2818, 2012.
- [53] A. Humeniuk, M. Wohlgemuth, T. Suzuki, and R. Mitríć. Time-resolved photo-electron imaging spectra from non-adiabatic molecular dynamics simulations. *J. Chem. Phys.*, 139(13):134104, 2013.
- [54] Y. Yamamoto, Y.-I. Suzuki, G. Tomasello, T. Horio, S. Karashima, R. Mitríć, and T. Suzuki. Time- and angle-resolved photoemission spectroscopy of hydrated electrons near a liquid water surface. *Phys. Rev. Lett.*, 112:187603, 2014.
- [55] G.M. Seabra, I. G. Kaplan, V. G. Zakrzewski, and J. V. Ortiz. Electron propagator theory calculations of molecular photoionization cross sections: The first-row hydrides. *J. Chem. Phys.*, 121:4143–4155, 2004.
- [56] G.M. Seabra, I. G. Kaplan, and J. V. Ortiz. Molecular photoionization cross sections in electron propagator theory: Angular distributions beyond the dipole approximation. *J. Chem. Phys.*, 123:114105, 2005.
- [57] A. M. Velasco, C. Lavin, I. Martin, J. Melin, and J. V. Ortiz. Partial photoionization cross sections of NH₄ and H₃O rydberg radicals. *J. Chem. Phys.*, 131:024104, 2009.
- [58] A. M. Velasco, C. Lavin, O. Dolgounitcheva, and J. V. Ortiz. Excitation energies, photoionization cross sections, and asymmetry parameters of the methyl and silyl radicals. *J. Chem. Phys.*, 141:074308, 2014.

- [59] C.M. Oana and A.I. Krylov. Dyson orbitals for ionization from the ground and electronically excited states within equation-of-motion coupled-cluster formalism: Theory, implementation, and examples. *J. Chem. Phys.*, 127:234106, 2007.
- [60] C.M. Oana and A.I. Krylov. Cross sections and photoelectron angular distributions in photodetachment from negative ions using equation-of-motion coupled-cluster Dyson orbitals. *J. Chem. Phys.*, 131:124114, 2009.
- [61] S.V. Levchenko and A.I. Krylov. Equation-of-motion spin-flip coupled-cluster model with single and double substitutions: Theory and application to cyclobutadiene. *J. Chem. Phys.*, 120(1):175–185, 2004.
- [62] J.G. Underwood and K.L. Reid. Time-resolved photoelectron angular distributions as a probe of intramolecular dynamics: Connecting the molecular frame and the laboratory frame. *J. Chem. Phys.*, 113:1067–1074, 2000.
- [63] G. Fronzoni, M. Stener, and P. Decleva. Valence and core photoionization dynamics of acetylene by TD-DFT continuum approach. *Chem. Phys.*, 298:141–153, 2004.
- [64] N. Rohringer, A. Gordon, and R. Santra. Configuration-interaction-based time-dependent orbital approach for ab initio treatment of electronic dynamics in a strong optical laser field. *Phys. Rev. A*, 74(4):043420, 2006.
- [65] X. Chu. Time-dependent density-functional-theory calculation of strong-field ionization rates of H₂. *Phys. Rev. A*, 82:023407, 2010.
- [66] A.P.P. Natalense and R. R. Lucchese. Cross section and asymmetry parameter calculation for sulfur 1s photoionization of SF₆. *J. Chem. Phys.*, 111:5344, 1999.
- [67] J. Cooper and R.N. Zare. Angular distribution of photoelectrons. *J. Chem. Phys.*, 48:942–943, 1968.
- [68] K.J. Reed, A.H. Zimmerman, H.C. Andersen, and J.I. Brauman. Cross sections for photodetachment of electrons from negative ions near threshold. *J. Chem. Phys.*, 64:1368–1375, 1976.
- [69] E. Surber, R. Mabbs, and A. Sanov. Probing the electronic structure of small molecular anions by photoelectron imaging. *J. Phys. Chem. A*, 107:8215–8224, 2003.
- [70] M.L. Weichman, J.B. Kim, J.A. DeVine, D.S. Levine, and D.M. Neumark. Vibrational and electronic structure of the α - and β -naphthyl radicals via slow photoelectron velocity-map imaging. *J. Am. Chem. Soc.*, 137:1420–1423, 2015.

- [71] P.V. Demekhin, A. Ehresmann, and V.L. Sukhorukov. Single center method: A computational tool for ionization and electronic excitation studies of molecules. *J. Chem. Phys.*, 134:024113, 2011.
- [72] R.F. Fink, M.N. Piancastelli, A.N. Grum-Grzhimailo, and K. Ueda. Angular distribution of Auger electrons from fixed-in-space and rotating C1s → 2π photoexcited CO: Theory. *J. Chem. Phys.*, 130:014306, 2009.
- [73] H. Siegbahn, L. Asplund, and P. Kelfve. The Auger electron spectrum of water vapour. *Chem. Phys. Lett.*, 35:330–335, 1975.
- [74] D.M. Bishop. Single-center molecular wave functions. *Adv. Quantum Chem.*, 3:25–59, 1967.
- [75] S. Han and D.R. Yarkony. A Lippmann-Schwinger approach for the determination of photoionization and photodetachment cross sections based on a partial wave Green's function expansion and configuration interaction wave functions. *Mol. Phys.*, 110:845–859, 2012.
- [76] R.R. Lucchese, K. Takatsuka, and V. McKoy. Applications of the Schwinger variational principle to electron–molecule collisions and molecular photoionization. *Phys. Rep.*, 131(3):147–221, 1986.
- [77] S. Han and D.R. Yarkony. On the determination of intensities for electron photodetachment and photoionization spectra involving states coupled by conical intersections: Total integral cross sections for polyatomic molecules. *J. Chem. Phys.*, 133:194107, 2010.
- [78] S. Han and D.R. Yarkony. Determining partial differential cross sections for low-energy electron photodetachment involving conical intersections using the solution of a Lippmann-Schwinger equation constructed with standard electronic structure techniques. *J. Chem. Phys.*, 134:174104, 2011.
- [79] S. Han and D.R. Yarkony. On the determination of partial differential cross sections for photodetachment and photoionization processes producing polyatomic molecules with electronic states coupled by conical intersections. *J. Chem. Phys.*, 134:134110, 2011.
- [80] S. Gozem and A.I. Krylov. ezDyson user's manual, 2015.
ezDyson, <http://iopenshell.usc.edu/downloads/>.
- [81] A.W. Castleman and K.H. Bowen. Clusters: Structure, energetics, and dynamics of intermediate states of matter. *J. Phys. Chem.*, 100:12911–12944, 1996.

- [82] H. Gomez, G. Meloni, J. Madrid, and D. M. Neumark. Anion photoelectron spectroscopy of solvated transition state precursors. *J. Chem. Phys.*, 119:872–879, 2003.
- [83] B. Winter and M. Faubel. Photoemission from liquid aqueous solutions. *Chem. Rev.*, 106:1176, 2006.
- [84] R. Seidel, B. Winter, and S.E. Bradforth. Valence electronic structure of aqueous solutions: Insights from photoelectron spectroscopy. *Annu. Rev. Phys. Chem.*, 67:283–305, 2006.
- [85] F. Buchner, T. Schultz, and A. Lubcke. Solvated electrons at the water–air interface: Surface versus bulk signal in low kinetic energy photoelectron spectroscopy. *Phys. Chem. Chem. Phys.*, 14:5837–5842, 2012.
- [86] S. Thürmer, R. Seidel, M. Faubel, W. Eberhardt, J.C. Hemminger, S.E. Bradforth, and B. Winter. Photoelectron angular distributions from liquid water: Effects of electron scattering. *Phys. Rev. Lett.*, 111:173005, 2013.
- [87] M. Goldmann, J. Miguel-Sanchez, A. H. C. West, B. L. Yoder, and R. Signorell. Electron mean free path from angle-dependent photoelectron spectroscopy of aerosol particles. *J. Chem. Phys.*, 142:224304, 2015.
- [88] M. Faubel, K. R. Siefermann, Y. Liu, and B. Abel. Ultrafast soft X-ray photoelectron spectroscopy at liquid water microjets. *Acc. Chem. Res.*, 45:120–130, 2012.
- [89] O. Bjorneholm, F. Federmann, S. Kakar, and T. Moller. Between vapor and ice: Free water clusters studied by core level spectroscopy. *J. Chem. Phys.*, 111(2):546–550, 1999.
- [90] F. Dong, S. Heinbuch, J. J. Rocca, and E. R. Bernstein. Dynamics and fragmentation of van der Waals clusters: $(\text{H}_2\text{O})_n$, $(\text{CH}_3\text{OH})_n$, and $(\text{NH}_3)_n$ upon ionization by a 26.5 eV soft X-ray laser. *J. Chem. Phys.*, 124(22):224319, 2006.
- [91] L. Belau, K. R. Wilson, S. R. Leone, and M. Ahmed. Vacuum ultraviolet (VUV) photoionization of small water clusters. *J. Phys. Chem. A*, 111:10075–10083, 2007.
- [92] S. Hartweg, B.L. Yoder, G.A. Garcia, L. Nahon, and R. Signorell. Size-resolved photoelectron anisotropy of gas phase water clusters and predictions for liquid water. *Phys. Rev. Lett.*, 2017. doi: arXiv:1612.02338.
- [93] R. Signorell, M. Goldmann, B. L. Yoder, A. Bodi, E. Chasovskikh, L. Lang, and D. Luckhaus. Nanofocusing, shadowing, and electron mean free path in the photoemission from aerosol droplets. *Chem. Phys. Lett.*, 658:1–6, 2016.

- [94] T. Suzuki. Time-resolved photoelectron spectroscopy of non-adiabatic electronic dynamics in gas and liquid phases. *Int. Rev. Phys. Chem.*, 31:265–318, 2012.
- [95] T. Helgaker, M. Jaszunski, and K. Ruud. Ab initio methods for the calculation of NMR shielding and indirect spin–spin coupling constants. *Chem. Rev.*, 99:293–352, 1999.
- [96] M.S. Gordon, D.G. Fedorov, S.R. Pruitt, and L.V. Slipchenko. Fragmentation methods: A route to accurate calculations on large systems. *Chem. Rev.*, 112:632–672, 2012.
- [97] K. Sneskov, T. Schwabe, J. Kongsted, and O. Christiansen. The polarizable embedding coupled cluster method. *J. Chem. Phys.*, 134:104108, 2011.
- [98] R. Mabbs, E. Surber, and A. Sanov. Photoelectron anisotropy and channel branching ratios in the detachment of solvated iodide cluster anions. *J. Chem. Phys.*, 122:054308, 2005.
- [99] L. Velarde, T. Habteyes, E. Grumbling, K. Pichugin, and A. Sanov. Solvent resonance effect on the anisotropy of $\text{NO}^-(\text{N}_2\text{O})_n$ cluster anion photodetachment. *J. Chem. Phys.*, 127:084302, 2007.
- [100] C.J. Cramer and D.G. Truhlar. Implicit solvation models: Equilibria, structure, spectra, and dynamics. *Chem. Rev.*, 99:2161, 1999.
- [101] M. Cossi, N. Rega, G. Scalmani, and V. Barone. Energies, structures, and electronic properties of molecules in solution with the C-PCM solvation model. *J. Comput. Chem.*, 24:669–681, 2003.
- [102] J. Tomasi, B. Mennucci, and R. Cammi. Quantum mechanical continuum solvation models. *Chem. Rev.*, 105:2999–3093, 2005.
- [103] C. J. Cramer and D. G. Truhlar. On the performance of continuum solvation methods. A comment on universal approaches to solvation modeling. *Acc. Chem. Res.*, 42:489–492, 2009.
- [104] A.W. Lange and J.M. Herbert. Polarizable continuum reaction-field solvation models affording smooth potential energy surfaces. *J. Phys. Chem. Lett.*, 1:556–561, 2009.
- [105] P. Slavíček, B. Winter, M. Faubel, S.E. Bradforth, and P. Jungwirth. Ionization energies of aqueous nucleic acids: Photoelectron spectroscopy of pyrimidine nucleosides and ab initio calculations. *J. Am. Chem. Soc.*, 131:6460–6467, 2009.

- [106] I. Duchemin, D. Jacquemin, and X. Blase. Combining the GW formalism with the polarizable continuum model: A state-specific non-equilibrium approach. *J. Chem. Phys.*, 144:164106, 2016.
- [107] B. Jagoda-Cwiklik, P. Slaviček, L. Cwiklik, D. Nolting, B. Winter, and P. Jungwirth. Ionization of imidazole in the gas phase, microhydrated environments, and in aqueous solution. *J. Phys. Chem. A*, 112:3499, 2008.
- [108] A.V. Marenich, C.J. Cramer, and D.G. Truhlar. Universal solvation model based on solute electron density and on a continuum model of the solvent defined by the bulk dielectric constant and atomic surface tensions. *J. Phys. Chem. B*, 113:6378–6396, 2009.
- [109] L. Sviatenko, O. Isayev, L. Gorb, F. Hill, and J. Lezczynski. Toward robust computational electrochemical predicting the environmental fate of organic pollutants. *J. Comput. Chem.*, 32:2195, 2011.
- [110] J. Zhang, H. Zhang, T. Wu, Q. Wang, and D. van der Spoel. Comparison of implicit and explicit solvent models for the calculation of solvation free energy in organic solvents. *J. Chem. Theory Comput.*, 2017. doi:10.1021/acs.jctc.7b00169.
- [111] M. Strajbl, G. Hong, and A. Warshel. Ab initio QM/MM simulation with proper sampling: “First principle” calculations of the free energy of the autodissociation of water in aqueous solution. *J. Phys. Chem. B*, 106:13333–13343, 2002.
- [112] H.M. Senn and W. Thiel. QM/MM methods for biomolecular systems. *Angew. Chem. Int. Ed.*, 48:1198–1229, 2009.
- [113] M.S. Gordon, M.A. Freitag, P. Bandyopadhyay, J.H. Jensen, V. Kairys, and W.J. Stevens. The effective fragment potential method: A QM-based MM approach to modeling environmental effects in chemistry. *J. Phys. Chem. A*, 105:293–307, 2001.
- [114] M.S. Gordon, L. Slipchenko, H. Li, and J.H. Jensen. Chapter 10. The effective fragment potential: A general method for predicting intermolecular interactions. In D.C. Spellmeyer and R. Wheeler, editors, *Annual Reports in Computational Chemistry*, volume 3, pages 177–193. Elsevier, 2007.
- [115] L.V. Slipchenko. Solvation of the excited states of chromophores in polarizable environment: Orbital relaxation versus polarization. *J. Phys. Chem. A*, 114:8824–8830, 2010.
- [116] D. Ghosh, O. Isayev, L.V. Slipchenko, and A.I. Krylov. The effect of solvation on vertical ionization energy of thymine: From microhydration to bulk. *J. Phys. Chem. A*, 115:6028–6038, 2011.

- [117] D. Ghosh. Hybrid Equation-of-Motion Coupled-Cluster/Effective Fragment Potential method: A route toward understanding photoprocesses in the condensed phase. *J. Phys. Chem. A*, 121:741–752, 2017.
- [118] K. Khistyayev, K.B. Bravaya, E. Kamarchik, O. Kostko, M. Ahmed, and A.I. Krylov. The effect of microhydration on ionization energies of thymine. *Faraday Discuss.*, 150:313–330, 2011.
- [119] E. Pluhařová, P. Slavíček, and P. Jungwirth. Modeling photoionization of aqueous dna and its components. *Acc. Chem. Res.*, 48:1209–1217, 2015.
- [120] J. Kessler, M. Dracinsky, and P. Bour. Parallel variable selection of molecular dynamics clusters as a tool for calculation of spectroscopic properties. *J. Comput. Chem.*, 34:366–371, 2013.
- [121] E. Pluhařová, P. Jungwirth, S. E. Bradforth, and P. Slaviček. Ionization of purine tautomers in nucleobases, nucleosides, and nucleotides: From the gas phase to the aqueous environment. *J. Phys. Chem. B*, 115:1294, 2011.
- [122] D. Ghosh, A. Roy, R. Seidel, B. Winter, S. Bradforth, and A.I. Krylov. A first-principle protocol for calculating ionization energies and redox potentials of solvated molecules and ions: Theory and application to aqueous phenol and phenolate. *J. Phys. Chem. B*, 116:7269–7280, 2012.
- [123] Q. Sun and G. K.-L. Chan. Quantum embedding theories. *Acc. Chem. Res.*, 49:2705–2712, 2016.
- [124] F. Libisch, C. Huang, and E. A. Carter. Embedded correlated wavefunction schemes: Theory and applications. *Acc. Chem. Res.*, 47:2768–2775, 2014.
- [125] J. M. Herbert. The quantum chemistry of loosely-bound electrons. *Rev. Comp. Chem.*, 28:391–517, 2015.
- [126] W. Weyl. Ueber metallammonium-verbindungen. *Ann. Phys.*, 197:601–612, 1864.
- [127] C.A. Kraus. Solutions of metals in non-metallic solvents; IV. Material effects accompanying the passage of an electrcal current through solutions of metals in liquid ammonia. Migration experiments. *J. Am. Chem. Soc.*, 30:1323–1344, 1908.
- [128] H.P. Cady. The electrolysis and electrolytic conductivity of certain substances dissolved in liquid ammonia. *J. Phys. Chem.*, 1:707–713, 1897.
- [129] E. Alizadeh and L. Sanche. Precursors of solvated electrons in radiobiological physics and chemistry. *Chem. Rev.*, 112:5578–5602, 2012.

- [130] J. Gu, J. Leszczynski, and H. F.Schaefer III. Interaction of electrons with bare and hydrated biomolecules: From nucleic acid bases to DNA segments. *Chem. Rev.*, 112:5603–5640, 2012.
- [131] E. Alizadeh, T.M. Orlando, and L. Sanche. Biomolecular damage induced by ionizing radiation: The direct and indirect effects of low-energy electrons on DNA. *Annu. Rev. Phys. Chem.*, 66:379, 2015.
- [132] B.C. Garrett, D.A. Dixon, D.M. Camaioni, D.M. Chipman, M.A. Johnson, C.D. Jonah, G.A. Kimmel, J.H. Miller, T.N. Rescigno, P.J. Rossky, S.S. Xantheas, S.D. Colson, A.H. Laufer, D. Ray, P.F. Barbara, D.M. Bartels, K.H. Becker, H. Bowen, S.E. Bradforth, I. Carmichael, J.V. Coe, L.R. Corrales, J.P. Cowin, M. Dupuis, K.B. Eisenthal, J.A. Franz, M.S. Gutowski, K.D. Jordan, B.D. Kay, J.A. LaVerne JA, S.V. Lymar, T.E. Madey, C.W. McCurdy, D. Meisel, S. Mukamel, A.R. Nilsson, T.M. Orlando, N.G. Petrik, S.M. Pimblott, J.R. Rustad, G.K. Schenter, S.J. Singer, A. Tokmakoff, L.S. Wang, C. Wittig, and T.S. Zwier. Role of water in electron-initiated processes and radical chemistry: Issues and scientific advances. *Chem. Rev.*, 105:355–389, 2005.
- [133] D. Caine. Reduction and related reactions of α,β -unsaturated carbonyl compounds with metals in liquid ammonia. *Organic Reactions*, 23:1–258, 2011.
- [134] G.V. Buxton. Chapter 1. An overview of the radiation chemistry of liquids. In M. Spotheim-Maurizot, M. Mostafavi, J. Belloni, and T. Douki, editors, *Radiation Chemistry: From Basics to Applications in Material and Life Sciences*, pages 3–16. EDP Sciences, 2008.
- [135] R. M. Young and D. M. Neumark. Dynamics of solvated electrons in clusters. *Chem. Rev.*, 112:5553–5577, 2012.
- [136] J. H. Litman, B. L. Yoder, B. Schlappi, and R. Signorell. Sodium-doping as a reference to study the influence of intracluster chemistry on the fragmentation of weakly-bound clusters upon vacuum ultraviolet photoionization. *Phys. Chem. Chem. Phys.*, 15:940–949, 2013.
- [137] M. Mostafavi and I. Lampre. Chapter 3. The Solvated Electron: A Singular Chemical Species. In M. Spotheim-Maurizot, M. Mostafavi, J. Belloni, and T. Douki, editors, *Radiation Chemistry: From Basics to Applications in Material and Life Sciences*, pages 33–52. EDP Sciences, 2008.
- [138] J.M. Herbert and L.D. Jacobson. Nature most squishy ion: The important role of solvent polarization in the description of the hydrated electron. *Int. Rev. Phys. Chem.*, 30:1–48, 2010.

- [139] L. Turi and P. J. Rossky. Theoretical Studies of Spectroscopy and Dynamics of Hydrated Electrons. *Chem. Rev.*, 112:5641–5674, 2012.
- [140] J. M. Herbert and M. P. Coons. The Hydrated Electron. *Annu. Rev. Phys. Chem.*, 68, 2017, doi: 10.1146/annurev-physchem-052516-050816.
- [141] K. R. Siefermann, Y. Liu, E. Lugovoy, O. Link, M. Faubel, U. Buck, B. Winter, and B. Abel. Binding energies, lifetimes and implications of bulk and interface solvated electrons in water. *Nat. Chem.*, 2:274–279, 2010.
- [142] Y. Tang, H. Shen, K. Sekiguchi, N. Kurahashi, T. Mizuno, Y. I. Suzuki, and T. Suzuki. Direct measurement of vertical binding energy of a hydrated electron. *Phys. Chem. Chem. Phys.*, 12:3653–3655, 2010.
- [143] A. Lubcke, F. Buchner, N. Heine, I. V. Hertel, and T. Schultz. Time-resolved photoelectron spectroscopy of solvated electrons in aqueous NaI solution. *Phys. Chem. Chem. Phys.*, 12:14629–14634, 2010.
- [144] A. T. Shreve, T. A. Yen, and D. M. Neumark. Photoelectron spectroscopy of hydrated electrons. *Chem. Phys. Lett.*, 493:216–219, 2010.
- [145] L.D. Jacobson and J. M. Herbert. Theoretical Characterization of Four Distinct Isomer Types in Hydrated-Electron Clusters, and Proposed Assignments for Photoelectron Spectra of Water Cluster Anions. *J. Am. Chem. Soc.*, 133:19889–19899, 2011.
- [146] J. R. R. Verlet, A. E. Bragg, A. Kammerath, O. Cheshnovsky, and D. M. Neumark. Observation of large water-cluster anions with surface-bound excess electrons. *Science*, 307:93–96, 2005.
- [147] A. Kammerath, J. R. R. Verlet, G.B. Griffin, and D. M. Neumark. Photoelectron imaging of large anionic methanol clusters: $(\text{MeOH})_n^-$ (n=70–460). *J. Chem. Phys.*, 125:171102, 2006.
- [148] M. Mitsui, N. Ando, S. Kokubo, A. Nakajima, and K. Kaya. Coexistence of solvated electrons and solvent valence anions in negatively charged acetonitrile clusters, $(\text{CH}_3\text{CN})_n^-$ (n=10–100). *Phys. Rev. Lett.*, 91:153002, 2003.
- [149] K. Hashimoto and K. Daigoku. Ground and low-lying excited states of $\text{Na}(\text{NH}_3)_n$ and $\text{Na}(\text{H}_2\text{O})_n$ clusters: Formation and localization of solvated electron. *Chem. Phys. Lett.*, 469:62–67, 2009.
- [150] E. Zurek, P.P. Edwards, and R. Hoffmann. A molecular perspective on lithium-ammonia solutions. *Angew. Chem. Int. Ed.*, 48(44):8198–8232, 2009.

- [151] A.H.C. West, B.L. Yoder, D. Luckhaus, C.-M. Saak, M. Doppelbauer, and R. Signorell. Angle-resolved photoemission of solvated electrons in sodium-doped clusters. *J. Phys. Chem. Lett.*, 6:1487–1492, 2015.
- [152] A.H.C. West, B.L. Yoder, D. Luckhaus, and R. Signorell. Solvated electrons in clusters: Magic numbers for the photoelectron anisotropy. *J. Phys. Chem. A*, 119:1237612382, 2015.
- [153] Shao, Y.; Gan, Z.; Epifanovsky, E.; Gilbert, A.T.B.; Wormit, M.; Kussmann, J.; Lange, A.W.; Behn, A.; Deng, J.; Feng, X., et al. Advances in molecular quantum chemistry contained in the Q-Chem 4 program package. *Mol. Phys.*, 113:184–215, 2015.

Chapter 2: Theory

2.1 Equation-of-motion coupled-cluster family of methods

Wave-function-based *ab initio* methods are constructed by representing electronic wave function Ψ in a basis of Slater determinants¹. A complete set of determinants gives rise to the exact solution, this is called full configuration interaction (full CI, FCI). The method scales exponentially with the number of electrons and one-electron basis functions and is, therefore, applicable only to the smallest systems. On the opposite extreme, one can take only one, leading determinant: this constitutes Hartree-Fock (HF) method, which scales polynomially as $O(N^4)$. The difference between this solution and the exact wave function is called electron correlation. The approximate electronic structure methods aim to capture as much correlation as possible while maintaining reasonable computational cost.

Within single-reference approaches, one defines HF determinant Φ_0 as a reference, divides orbitals into the occupied i, j, k, \dots and virtual a, b, c, \dots subspaces, and constructs other determinants in the FCI expansion as all possible μ -tuple excitations with respect to this reference:

$$|\Psi\rangle = |\Phi_0\rangle + \sum_{\mu} c_{\mu} |\Phi_{\mu}\rangle = (1 + \sum_{\mu} \hat{C}_{\mu}) |\Phi_0\rangle \quad (2.1)$$

Intuitively, it is tempting to truncate expression (2.1) at some low level of μ . This gives rise to truncated CI methods. Although physically motivated, this approach lacks size-extensivity, meaning that the energy of a system of non-interacting fragments is not equal to the sum of fragment energies and the wave function is not separable. Apart from being fundamentally wrong, the lack of size-extensivity leads to deteriorating performance with the increase of the system size. Truncating FCI expansion such that size-consistency is preserved is possible via exponential *ansatz*, giving rise to coupled-cluster (CC) methods^{2–5}.

$$|\Psi\rangle = e^{(\hat{T}_1 + \hat{T}_2 + \dots + \hat{T}_n)} |\Phi_0\rangle \quad (2.2)$$

where \hat{T}_i are called cluster operators. Without truncation, this ansatz is equivalent to the FCI expansion. Truncating at singles and doubles (SD) level (i.e., keeping only \hat{T}_1 and \hat{T}_2) allows to recover $\sim 95\%$ of electron correlation while maintaining polynomial scaling with respect to the number of basis orbitals, $O(N^6)$. In the second-quantization language, cluster operators are defined as

$$\hat{T}_1 = \sum_{ia} t_i^a \hat{a}^\dagger \hat{i}, \quad (2.3)$$

$$\hat{T}_2 = \frac{1}{4} \sum_{ijab} t_{ij}^{ab} \hat{a}^\dagger \hat{b}^\dagger \hat{i} \hat{j}, \quad (2.4)$$

...

Solving CCSD equations entails finding t -amplitudes, t_i^a and t_{ij}^{ab} , which is done by projection

$$\langle \Phi_\mu | \bar{H} - E_{CC} | \Phi_0 \rangle = 0, \quad (2.5)$$

where we introduced similarity-transformed Hamiltonian $\bar{H} = e^{-\hat{T}} H e^{\hat{T}}$. Applying the CI-type operators on top of the CCSD reference gives rise to the equation-of-motion coupled-cluster (EOM-CC) family of methods⁶.

$$|\Psi\rangle = \hat{R}e^{\hat{T}}|\Phi_0\rangle \quad (2.6)$$

$$\bar{H}\hat{R} = E\hat{R} \quad (2.7)$$

The EOM amplitudes and the corresponding energies are found by diagonalizing the similarity-transformed Hamiltonian, \bar{H} , in the space of target configurations. Different choices of the reference and the type of EOM operators \hat{R} enable access to different types of electronic states, which is illustrated in Fig. 2.1. If \hat{R} conserves the number of electrons of each spin, one obtains the description of electronically excited states, the EOM-EE-CCSD method:

$$\hat{R}^{EE} = r_0 \hat{I} + \sum_{ia} r_i^a \hat{a}^\dagger \hat{i} + \frac{1}{4} \sum_{ijab} r_{ij}^{ab} \hat{a}^\dagger \hat{b}^\dagger \hat{j} \hat{i} \quad (2.8)$$

Here \hat{I} is a unit operator, which allows ground state reference to contribute to the final excited state, and r are right EOM amplitudes. By using one-particle ($1p$) and two-particles-one-hole ($2p1h$) operators, an electron is added to the reference, which describes electron attachment (EOM-EA-CCSD). Likewise, employing $1h$ and $1p2h$ operators describes electron removal, i.e., ionization, and the respective method is called EOM-IP-CCSD.

$$\hat{R}^{EA} = \sum_a r^a \hat{a}^\dagger + \frac{1}{2} \sum_{iab} r_i^{ab} \hat{a}^\dagger \hat{b}^\dagger \hat{i} \quad (2.9)$$

$$\hat{R}^{IP} = \sum_i r_i \hat{i} + \frac{1}{2} \sum_{ija} r_{ij}^a \hat{a}^\dagger \hat{j} \hat{i}$$
(2.10)

All EOM variants need stable vacuum state, i.e., they only work well for the cases when the reference determinant provides good approximation for the reference state. This is not the case for open-shell singlets, diradicals, and triradicals, where multi-reference character of low-multiplicity states is considerable. Starting then from well-behaving high-spin reference and applying spin-flipping EOM operator gives rise to EOM-SF-CCSD method, which enables balanced treatment of these challenging target states.

$$\hat{R}^{SF} = \sum_{ia} r_i^a \hat{a}_\beta^\dagger \hat{l}_\alpha + \dots$$
(2.11)

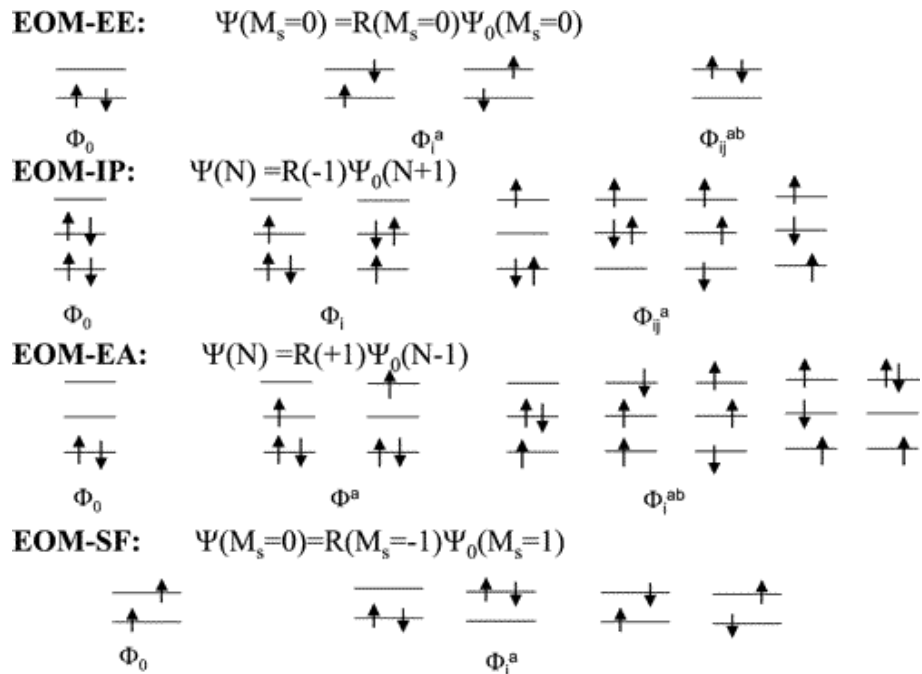


Figure 2.1: Various EOM operators describing electronic excitations, ionizations, electron attachment and open-shell singlets. Adapted with permission from Ref. 7. Copyright 2006 American Chemical Society.

Similarity-transformed Hamiltonian \bar{H} is no longer a Hermitian operator, therefore it has left and right eigenvectors, $\langle \Phi_0 | \hat{L}^\dagger$ and $\hat{R} | \Phi_0 \rangle$. They form a biorthogonal set:

$$\bar{H}\hat{R}|\Phi_0\rangle = E\hat{R}|\Phi_0\rangle, \quad (2.12)$$

$$\langle \Phi_0 | \hat{L}^\dagger \bar{H} = \langle \Phi_0 | \hat{L}^\dagger E, \quad (2.13)$$

$$\langle \Phi_0 | (\hat{L}^\dagger)^K \hat{R}^M | \Phi_0 \rangle = \delta_{KM}, \quad (2.14)$$

where K and M label the K th and M th EOM states. Left eigenvectors have the same form as the right ones, Eqs. (2.8,2.9,2.10,2.11), except for R_0 , and \hat{L}^\dagger can be described as de-excitations (which is equivalent to excitations for the *ket* states). Having r -amplitudes, one can compute EOM energies Ω (excitation, ionization, electron attachment, or spin-flip) directly as a set of differences with respect to the reference state

$$(\bar{H} - E_{CC}\hat{I})\hat{R} = \hat{R}\Omega \quad (2.15)$$

Solving for left l -amplitudes is necessary for calculating properties. Due to bi-orthogonality, the left and right expectation values of operator \hat{A} are not identical, and the corresponding physical property should be computed as a geometric average:

$$\hat{A}^{MK} = \sqrt{\langle \Phi_0 | \hat{L}^{M\dagger} e^{-\hat{T}} \hat{A} e^{\hat{T}} \hat{R}^K | \Phi_0 \rangle \langle \Phi_0 | \hat{L}^{K\dagger} e^{-\hat{T}} \hat{A} e^{\hat{T}} \hat{R}^M | \Phi_0 \rangle} \quad (2.16)$$

2.2 Dyson orbitals

Dyson orbitals, Eq. (2.17), are defined for any two wave functions that differ by one electron

$$\phi_{IF}^d = \sqrt{N} \int \Psi_N^I(1, \dots, n) \Psi_{N-1}^F(2, \dots, n) d2 \dots dn \quad (2.17)$$

Within EOM-CCSD one can take EOM-IP-CCSD wave function to describe the final state, and the CCSD wave function to describe the ground state. Alternatively, one can use EOM-EE-CCSD for an excited state or EOM-SF-CCSD for a tricky open-shell state as an initial wave function. Different options are available for an initial doublet state, which can be conveniently accessed via EOM-EA-CCSD and combined with CCSD ground closed-shell singlet, or EOM-EE-CCSD excited, or EOM-SF-CCSD open-shell final states.

Since both CCSD and all EOM-CCSD flavors are built over the same reference determinant, Dyson orbitals can be expanded over a set of the reference molecular orbitals:

$$\phi^d = \sum_p \gamma_p \phi_p \quad (2.18)$$

where index p, q, r, \dots denotes any – occupied or virtual – orbital. Following the convention from Refs. 8, 9, we label the coefficients of expansion (2.18) for the left and right Dyson orbitals as:

$$\gamma_p^R = \langle \Psi^N | \hat{p}^\dagger | \Psi^{N-1} \rangle \quad (2.19)$$

$$\gamma_q^L = \langle \Psi^{N-1} | \hat{q} | \Psi^N \rangle \quad (2.20)$$

Programmable expressions for the EOM-CCSD Dyson orbitals are given below. For practical purposes, it is convenient to derive and compute occupied and virtual sets of the coefficients separately.

- CCSD to EOM-IP-CCSD:

$$\gamma_a^R = \langle \Phi_0 e^{-T} (I + \Lambda) | \hat{a}^\dagger | R_{IP} e^T \Phi_0 \rangle = \sum_k \lambda_a^k r_k + \frac{1}{2} \sum_{klc} \lambda_{ca}^{lk} r_{kl}^c, \quad (2.21)$$

$$\begin{aligned} \gamma_i^R &= \langle \Phi_0 e^{-T} (I + \Lambda) | \hat{i}^\dagger | R_{IP} e^T \Phi_0 \rangle = \\ &= r_i + \sum_{kc} \lambda_c^k r_{ik}^c - \sum_c \gamma_c^R t_i^c - \frac{1}{2} \sum_k r_k \sum_{lcd} \lambda_{dc}^{lk} t_{li}^{dc}, \end{aligned} \quad (2.22)$$

$$\gamma_a^L = \langle \Phi_0 e^{-T} L_{IP} | \hat{a} | e^T \Phi_0 \rangle = \sum_k l^k t_k^a + \frac{1}{2} \sum_{klc} l_c^{kl} t_{kl}^{ac}, \quad (2.23)$$

$$\gamma_i^L = \langle \Phi_0 e^{-T} L_{IP} | \hat{i} | e^T \Phi_0 \rangle = l^i \quad (2.24)$$

- EOM-EE-CCSD or EOM-SF-CCSD to EOM-IP-CCSD (note the term from CC/IP):

$$\gamma_a^R = \langle \Phi_0 e^{-T} L_{EE} | \hat{a}^\dagger | R_{IP} e^T \Phi_0 \rangle = \sum_{kc} l_a^k r_k + \frac{1}{2} \sum_{klc} l_{ca}^{lk} r_{kl}^c, \quad (2.25)$$

$$\begin{aligned} \gamma_i^R &= \langle \Phi_0 e^{-T} L_{EE} | \hat{i}^\dagger | R_{IP} e^T \Phi_0 \rangle = \\ &= \sum_{kc} l_c^k r_{ik}^c - \sum_c \gamma_c^{R,virt} t_i^c - \frac{1}{2} \sum_{klcd} l_{dc}^{lk} t_{li}^{dc} r_k, \end{aligned} \quad (2.26)$$

$$\begin{aligned} \gamma_a^L &= \langle \Phi_0 e^{-T} L_{IP} | \hat{a} | R_{EEE} e^T \Phi_0 \rangle = \\ &= r_0 \gamma_a^{L,CC-IP} + \sum_{kc} l^k r_k^a + \frac{1}{2} \sum_{klc} l_c^{kl} r_{kl}^{ac} + \sum_{klc} l_c^{kl} t_k^a r_l^c, \end{aligned} \quad (2.27)$$

$$\gamma_i^L = \langle \Phi_0 e^{-T} L_{IP} | \hat{i} | R_{EEE} e^T \Phi_0 \rangle = l^i r_0 + \sum_{kc} l_c^{ik} r_k^c \quad (2.28)$$

- EOM-EA-CCSD to CCSD:

$$\gamma_i^R = \langle \Phi_0 e^{-T} L_{EA} | \hat{i}^\dagger | e^T \Phi_0 \rangle = - \sum_c l_c t_i^c + \frac{1}{2} \sum_{kcd} l_{dc}^k t_{ki}^{dc}, \quad (2.29)$$

$$\gamma_a^R = \langle \Phi_0 e^{-T} L_{EA} | \hat{a}^\dagger | e^T \Phi_0 \rangle = l_a, \quad (2.30)$$

$$\gamma_i^L = \langle \Phi_0 e^{-T} (I + \Lambda) | \hat{i} | R_{EA} e^T \Phi_0 \rangle = - \sum_c \lambda_c^i r^c + \frac{1}{2} \sum_{kcd} \lambda_{cd}^{ik} r_k^{dc}, \quad (2.31)$$

$$\gamma_a^L = \langle \Phi_0 e^{-T} (I + \Lambda) | \hat{a} | R_{EA} e^T \Phi_0 \rangle = \quad (2.32)$$

$$= r^a + \sum_{kc} \lambda_c^k r_k^{ca} + \sum_k t_k^a \gamma_k^L - \frac{1}{2} \sum_{ckld} \lambda_{dc}^{lk} t_{lk}^{da} r^c$$

- EOM-EA-CCSD to EOM-EE-CCSD or EOM-SF-CCSD (note the term from EA/CC):

$$\gamma_i^R = \langle \Phi_0 e^{-T} L_{EA} | \hat{i}^\dagger | R_{EE} e^T \Phi_0 \rangle = \quad (2.33)$$

$$= r_0 \gamma_i^{R, EA-CC} - \sum_c r_i^c l_c - \frac{1}{2} \sum_{lcd} r_{il}^{cd} l_{dc}^l - \sum_{lcd} t_i^c l_{dc}^l r_l^d,$$

$$\gamma_a^R = \langle \Phi_0 e^{-T} L_{EA} | \hat{a}^\dagger | R_{EE} e^T \Phi_0 \rangle = l_a r_0 + \sum_{kc} l_{ca}^k r_k^c, \quad (2.34)$$

$$\gamma_i^L = \langle \Phi_0 e^{-T} L_{EE} | \hat{i} | R_{EA} e^T \Phi_0 \rangle = - \sum_c l_c^i r^c - \frac{1}{2} \sum_{kcd} l_{cd}^{ik} r_k^{dc}, \quad (2.35)$$

$$\gamma_a^L = \langle \Phi_0 e^{-T} L_{EE} | \hat{a} | R_{EA} e^T \Phi_0 \rangle = \quad (2.36)$$

$$= \sum_{kc} r_k^{ca} l_c^k + \sum_k t_k^a \gamma_k^L - \frac{1}{2} \sum_{klcd} l_{dc}^{lk} t_{lk}^{da} r^c$$

2.3 Chapter 2 references

- [1] T. Helgaker, P. Jørgensen, and J. Olsen. *Molecular electronic structure theory*. Wiley & Sons, 2000.
- [2] J. Cizek. On the correlation problem in atomic and molecular systems. Calculation of wavefunction components in Ursell-type expansion using quantum-field theoretical methods. *J. Chem. Phys.*, 45:4256–4266, 1966.
- [3] G.D. Purvis and R.J. Bartlett. A full coupled-cluster singles and doubles model: The inclusion of disconnected triples. *J. Chem. Phys.*, 76:1910–1918, 1982.
- [4] M. Musiał and R. J. Bartlett. Coupled-cluster theory in quantum chemistry. *Rev. Mod. Phys.*, 79:291, 2007.
- [5] R.J. Bartlett. Coupled-cluster theory and its equation-of-motion extensions. *WIREs Comput. Mol. Sci.*, 2(1):126–138, 2012.
- [6] A.I. Krylov. Equation-of-motion coupled-cluster methods for open-shell and electronically excited species: The hitchhiker’s guide to Fock space. *Annu. Rev. Phys. Chem.*, 59:433–462, 2008.
- [7] A.I. Krylov. The spin-flip equation-of-motion coupled-cluster electronic structure method for a description of excited states, bond-breaking, diradicals, and triradicals. *Acc. Chem. Res.*, 39:83–91, 2006.
- [8] C.M. Oana and A.I. Krylov. Dyson orbitals for ionization from the ground and electronically excited states within equation-of-motion coupled-cluster formalism: Theory, implementation, and examples. *J. Chem. Phys.*, 127:234106, 2007.
- [9] C.M. Oana and A.I. Krylov. Cross sections and photoelectron angular distributions in photodetachment from negative ions using equation-of-motion coupled-cluster Dyson orbitals. *J. Chem. Phys.*, 131:124114, 2009.

Chapter 3: Photoelectron wave function in photoionization: Plane wave or Coulomb wave?

3.1 Photoelectron wave function in photoionization

Photoionization and photodetachment experiments are broadly used in chemical physics^{1–3}. Photoionization is often used as a tool to identify transient reaction intermediates, whereas photodetachment can be employed to create molecules that are reactive intermediates or otherwise unstable in order to study their properties and spectroscopic signatures^{4–6}. Such experiments provide detailed information about the energy levels of the target systems and, often equally important, about the underlying wave functions. However, the interpretation of the photoionization/photodetachment measurements is in many cases not straightforward and requires input from theory. For example, calculations of Franck-Condon factors (FCFs) allow one to connect the features in photoelectron kinetic energy distributions with specific structural changes induced by electron ejection. Particularly challenging is extracting information about the wave functions from the measured cross-sections and photoelectron angular distributions.

The information about electronic states of the system is encoded in the so-called photoelectron matrix element, D_k^{IF} :

$$D_k^{IF} = u \langle \phi_{IF}^d | r | \Psi_k^{el} \rangle, \quad (3.1)$$

where r is the dipole moment operator, u is a unit vector in the direction of the polarization of light, and Ψ_k^{el} is the wave function of the ejected electron. ϕ_{IF}^d is a Dyson orbital connecting the initial N -electron and the final $N-1$ -electron states (I and F, respectively)⁷⁻¹⁰:

$$\phi_{IF}^d(1) = \sqrt{N} \int \Psi_I^N(1, \dots, n) \Psi_F^{N-1}(2, \dots, n) d2 \dots dn. \quad (3.2)$$

Eqns. (4.2)-(4.1) are derived within the dipole approximation and assuming strong orthogonality between Ψ_k^{el} and ϕ_{IF}^d and Ψ_F^{N-1} . D_k^{IF} enters the expression of the total cross-section^{11, 12}:

$$\sigma_k = \frac{4\pi^2 k E}{c} |D_k^{IF}|^2 \quad (3.3)$$

Atomic units are used throughout this letter. E is the energy of the ionizing radiation, c is the speed of light, and k is the magnitude of the photoelectron wave vector related to its kinetic energy, E_k , by $k = \sqrt{2E_k}$. If several channels are open (i.e., when various final Ψ_F^{N-1} states are accessible at given energy), the total cross-section is simply a sum of the cross-sections computed for each channel using its respective Dyson orbital, ϕ_{IF}^d .

The calculation of the photoelectron matrix element in Eq. (4.2) requires the Dyson orbital and the photoelectron wave function. The Dyson orbital, which is a correlated analogue of a Hartree-Fock orbital describing the initial state of the ionized electron within Koopmans' theorem, contains all the information about molecular wave functions needed for computing the photoelectron matrix element⁸⁻¹⁰. Dyson orbitals¹⁰ can be computed within the equation-of-motion coupled-cluster (EOM-CC) framework¹³⁻¹⁵,

which provides accurate wave functions for closed-shell and various types of open-shell systems. EOM-CC Dyson orbitals include electron correlation and orbital relaxation effects that are neglected in Koopmans' approximation. In this Letter, we consider photoejection from closed-shell systems, a situation which usually can be accurately described by EOM-CC variant known as EOM-IP-CC (EOM-CC for ionization potentials)^{16–18}. We employ EOM-IP-CC with single and double substitutions (EOM-IP-CCSD).

By using accurate correlated Dyson orbitals, we can focus our attention on approximate treatments of the photoelectron wave function, Ψ_k^{el} . In particular, we test the ability of the simplest possible approximations, i.e., using plane or Coulomb waves, to reproduce experimental cross-sections. Our goal is to determine whether Eq. (4.2) obtained within strong orthogonality assumption and the simplest ansatz, single-center expansion of Ψ^{el} , can capture the correct physics of the problem.

Han and Yarkony pointed out that the strong orthogonality assumption might be too extreme¹⁹. While various theories of molecular photoionization are capable of providing a quantitatively accurate description of experimental data²⁰, applications are often limited by the level of electron correlation that can be employed^{21–24}. Alternatively, the Stieltjes imaging approach^{25,26} allows one to compute cross-sections for photoionization/photodetachment with, in principle, any excited-state electronic structure method by performing a series of necessarily expensive calculations using very diffuse basis sets. In Stieltjes calculations, the state of the ejected electron is approximated by the discretized representation of the continuum states. Since the target state of the system is described by the same many-electron method as the initial state, the strong orthogonality condition is not invoked and the Coulomb and exchange/correlation interactions

are described without the assumption of orthogonality. The application of the Stieltjes method with linear response CCSD (a formalism in which the target state energies are identical to EOM-CCSD but transition properties are computed in a different fashion) was shown to yield accurate cross-sections for photodetachment²⁷ and photoionization²⁸; however, numerical difficulties can be encountered in the effort to obtain converged results with this procedure. Averbukh and coworkers reported²⁹ good results for photoionization cross-sections of closed-shell molecules obtained using the Stieltjes method with the method known as Algebraic Diagrammatic Construction (ADC)³⁰. They observed that the accuracy of the calculations deteriorates at higher energies, which they attribute to using Gaussian bases for representing the continuum. By introducing mixed bases in the Stieltjes scheme, i.e., Gaussian and B-splines, they were able to achieve uniform performance over a large energy range³¹. These studies^{27–29,31} illustrate that correlated methods such as CCSD and ADC are capable of providing wave functions that are sufficiently accurate for obtaining cross-sections within the Stieltjes scheme. Thus, it is desirable to understand the limits of applicability of a simpler model of photoionization (strong orthogonality and single-center expansion) employing Dyson orbitals computed using high-level electronic structure methods. We note that the success of the Cooper-Zare model³² and its extension to molecular systems^{12,33} in fitting and explaining experimental trends in photoionization cross-sections and angular distributions^{2,34,35} suggests that the underlying assumptions do capture the essential physics of the problem. Similar single-center models have been successfully used in the context of photoionization^{36–39}. Han and Yarkony have developed a theoretical framework for determining the state of the ejected electron using the Lippmann-Schwinger equation accounting for non-orthogonality and exchange interactions with the core^{19,40–42}. Once the implementation of this much more rigorous framework becomes available, it

will become possible to validate approximate treatments such as those explored in this work against their results. However, in the meantime, we are restricted to calibrating our model against experiment, a strategy which we adopt in this Letter.

By completely neglecting interactions with the remaining core, the photoelectron can be treated as a plane wave (PW):

$$\Psi_k^{el} = \frac{1}{(2\pi)^{\frac{3}{2}}} e^{ik \cdot r} \quad (3.4)$$

The $(2\pi)^{-3/2}$ factor is the “continuum normalization” typically used for PWs⁴³.

It is convenient to express the PW as a sum of spherical partial waves⁴⁴:

$$e^{ik \cdot r} = 4\pi \sum_{l=0}^{\infty} \sum_{m=-l}^l i^l R_l(kr) Y_{lm}^*(\hat{r}) Y_{lm}(\hat{k}), \quad (3.5)$$

where \hat{r} and \hat{k} are the position vector and wave vector, respectively. Each spherical wave is characterized by its energy, $E_k = \frac{k^2}{2}$, and angular momentum parameters l and m . The wave function (3.5) is expressed as a product of radial and angular functions. The angular function corresponds to spherical harmonics (Y_{lm}), whereas the radial function for a PW can be expressed using spherical Bessel functions, $R_l(kr) = j_l(kr)$. The expansion origin is placed at the centroid of the Dyson orbital, which is equivalent to orthogonalizing Ψ^{el} to the Dyson orbital³³. In other words, the origin of the expansion in our approach is fixed such that strong orthogonality condition is partially satisfied (i.e., Ψ^{el} is orthogonal to ϕ^d). Note that for spherically symmetric species, in which single-center expansion is exact, the centroid of the Dyson orbital always coincides with the origin of the expansion.

The PW approximation assumes no electrostatic or exchange/correlation interactions between the ejected photoelectron and the remaining core, which can be justified

by a very large size of the free electron relative to the core. This is certainly a reasonable assumption in the case of photodetachment from anions, where the remaining core is neutral. However, in photoionization of neutral species, the core is positively charged, creating a long-range Coulomb potential that can meaningfully perturb the ejected electron. It is possible to account for these electrostatic interactions by using a Coulomb-distorted plane wave, also known as a Coulomb wave (CW). For a CW, the ionized core is treated as a point charge (i.e., which generates a spherically symmetric field), therefore affecting only the radial part of the photoelectron wave function without affecting the angular part. The CW can also be expanded as a sum of Coulomb partial waves using the same expression as Eq. (3.5); however, instead of using spherical Bessel functions, the radial part is described using a Coulomb radial wave function⁴⁵:

$$R_l(kr, \eta) = (2kr)^l e^{-\frac{\pi i \eta}{2}} \frac{|\Gamma(l+1+i\eta)|}{\Gamma(2l+2)} e^{-ikr} {}_1F_1(l+1-i\eta, 2l+2, 2ikr), \quad (3.6)$$

where Γ is the Gamma function and ${}_1F_1$ is the confluent hypergeometric function of the first kind. η is the Sommerfeld parameter, which is equal to $-Z/k$ in atomic units (taking the electron charge to be -1), where Z is the charge of the ionized core and k is the magnitude of the photoelectron wave vector. When $Z=0$, the CW becomes a PW since the Coulomb radial function becomes a spherical Bessel function. Fig. 3.1 shows the radial function, Eq. (3.6), for three different values of Z ; 0, 0.5, and 1.0. For the same kinetic energy, the CW is more compact along r and displays more oscillations than its PW counterpart. A more detailed comparison between CWs and PWs is presented in Fig. 3.7 in the supporting information (Appendix). Even for small kinetic energies, CWs rise quickly at the origin for small non-zero l , whereas PWs are much slower to rise. For $l=0$, the PW has a value of 1 at the origin, while CWs have a larger value (which is determined by the respective normalization constant) that becomes yet larger

as k becomes smaller. This can be explained by the fact that slow electrons have a larger probability to be close to the positive charge.

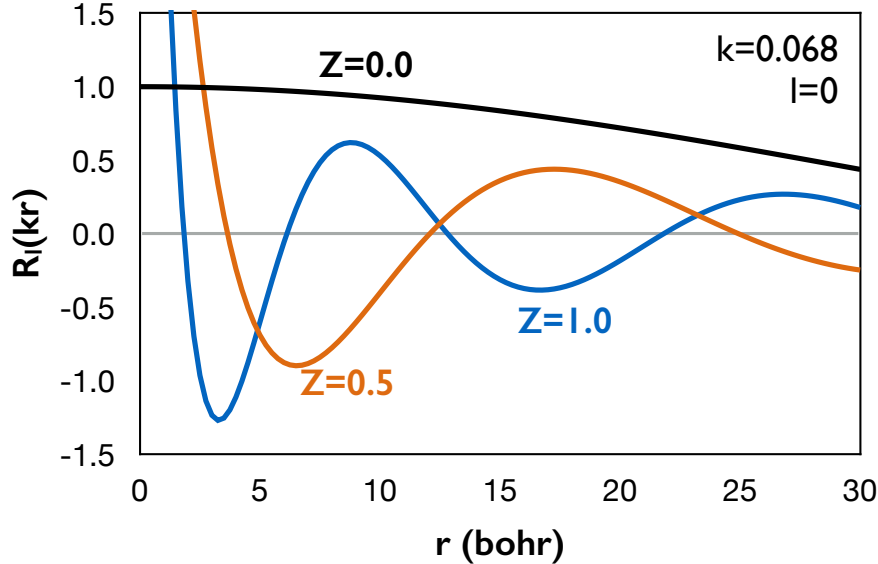


Figure 3.1: Coulomb radial function for $l=0$ and $k=0.068$ a.u. ($E_k=0.0625$ eV), with $Z=0$, 0.5, and 1.0 (black, orange, and blue curves, respectively). The Coulomb radial function with $Z=0$ is identical to the spherical Bessel function. In the systems studied here, Dyson orbitals do not extend beyond 12 bohr.

Here we consider several atomic and molecular systems for which reliable experimental cross-sections are available. We focus on systems with relatively small ionization-induced structural changes, such that FCFs can be reliably calculated using the double-harmonic Franck-Condon approximation, which allows us to focus on the electronic part of the problem, Eq. (4.2). We also do not consider systems that show evidence of ionization via autoionizing resonances; these cases can, in principle, be approached by the extension of EOM-CC theory to metastable electronic states⁴⁶. We

are particularly interested in the cross-sections near threshold (the origin of the ionization/photodetachment and a few eV above it) as this is a key “fingerprint” region that, for example, plays an important role in identifying isomers in reactive mixtures^{47–49}.

For all molecules studied in this work, structures are optimized at the DFT level of theory with the ω B97X-D functional⁵⁰. Dyson orbitals are computed in Q-Chem⁵¹, with the initial and final wave functions, Ψ_I^N and Ψ_F^{N-1} , described by CCSD and EOM-IP-CCSD, respectively. All optimizations and FCF calculations employ the aug-cc-pVTZ basis set. Dyson orbitals for neutral systems are also computed with aug-cc-pVTZ, unless indicated otherwise. Dyson orbitals for the anions are computed with the d-aug-cc-pVQZ basis set (additional augmentation has little to no effect for neutral systems). cross-section are computed with *ezDyson*^{33,52} using experimentally determined ionization energies. FCFs are computed by *ezSpectrum*⁵³. using DFT (ω B97X-D) structures and frequencies. The details about averaging over molecular orientations, accounting for electronic degeneracies of the initial and target states, and incorporating FCFs into the cross-sections calculations can be found in the *ezDyson* manual⁵².

The performance of the PW description with EOM-CCSD Dyson orbitals in calculations of the cross-sections for photodetachment from small atomic and molecular anions has been tested before³³. As illustrated in Fig. 3.2, the difference between those computed with PW and CW is huge. As one can see, the PW approach can reproduce the experimental cross sections well — the discrepancies between the computed and measured cross-sections are within the experimental uncertainties⁵⁴ (e.g., 30% for Li^-).

However, the same protocol applied for computing photoionization cross-sections for small neutral systems (such as He, Ne, Ar, H₂) leads to disastrous results. On the other hand, as illustrated in Fig. 3.3, the calculations using the CW representation (with Z=+1) yield very good agreement with the experiments, both in terms of the magnitude

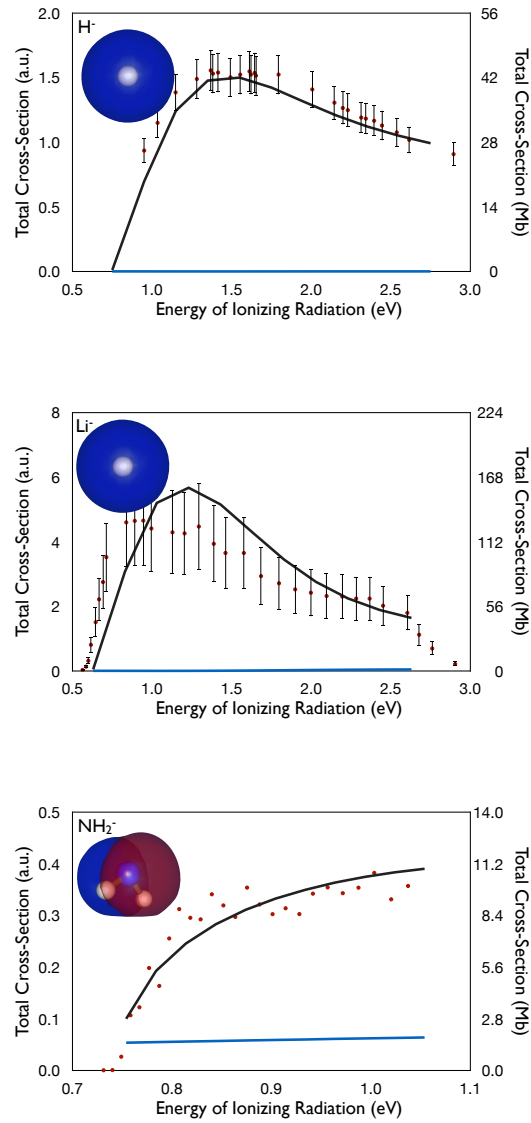


Figure 3.2: Absolute cross-sections for photodetachment from H^- , Li^- , and NH_2^- . Red dots are the experimental values from Refs. ⁵⁵ (H^-), ⁵⁴ (Li^-), and ⁵⁶ (NH_2^-). Black and blue curves denote cross-sections computed using PWs and CWs (with $Z=1$), respectively. For NH_2^- , only the relative cross-sections were measured experimentally and so they have been scaled to match absolute cross-sections obtained by calculations. FCFs are included for NH_2^- . The corresponding Dyson orbitals are shown in the top left corners.

and the shape (with the exception of the Cooper minimum in Ar⁵⁷ discussed below). The theoretical curves are practically on top of the experimental ones for He, Ne, and H₂. Likewise, the absolute partial cross-sections for the three different ionized states of water (Fig. 3.4) show much better agreement with experiment when computed using CWS. We emphasize that both partial cross-sections corresponding to three different valence ionized states and the total cross-section are reproduced well. We note that our calculations fail to reproduce the Cooper minimum in Ar⁵⁷, a spectral feature at around 47 eV observed in the photoionization spectrum as well as in high-harmonic spectra^{58–60}. The Cooper minimum arises due to the node in the Dyson orbital, which leads to the change of the sign in the photoelectron matrix element as the outgoing *d*-wave moves in at higher E_k . Thus, the position of the Cooper minimum is defined by the shape of the Dyson orbital and by Ψ_{el} . The calculations by Wörner *et al.*⁶⁰ failed to reproduce the Cooper minimum when using plane or Coulomb waves and an uncorrelated Dyson orbital. However, they were able to describe the minimum with free electron wave functions computed using effective central potential accounting for exchange interactions with the core. In the Stieltjes imaging calculations³¹, the position of the Cooper minimum was found to be very sensitive to the details of calculations (quantitative agreement with the experiment was only achieved when using a B-spline instead of Gaussian basis, which provides a better description of the continuum).

The better performance of CWS for photoionization of atomic neutral species is not surprising, and one may expect that CWS might also work well for larger neutral targets. However, as illustrated below, the performance is not uniform; in polyatomic systems a better agreement with experiment is sometimes observed for PWs. An optimal description of the photoelectron is often obtained with a CW parameterized with a partial charge, $Z \in [0, 1]$.

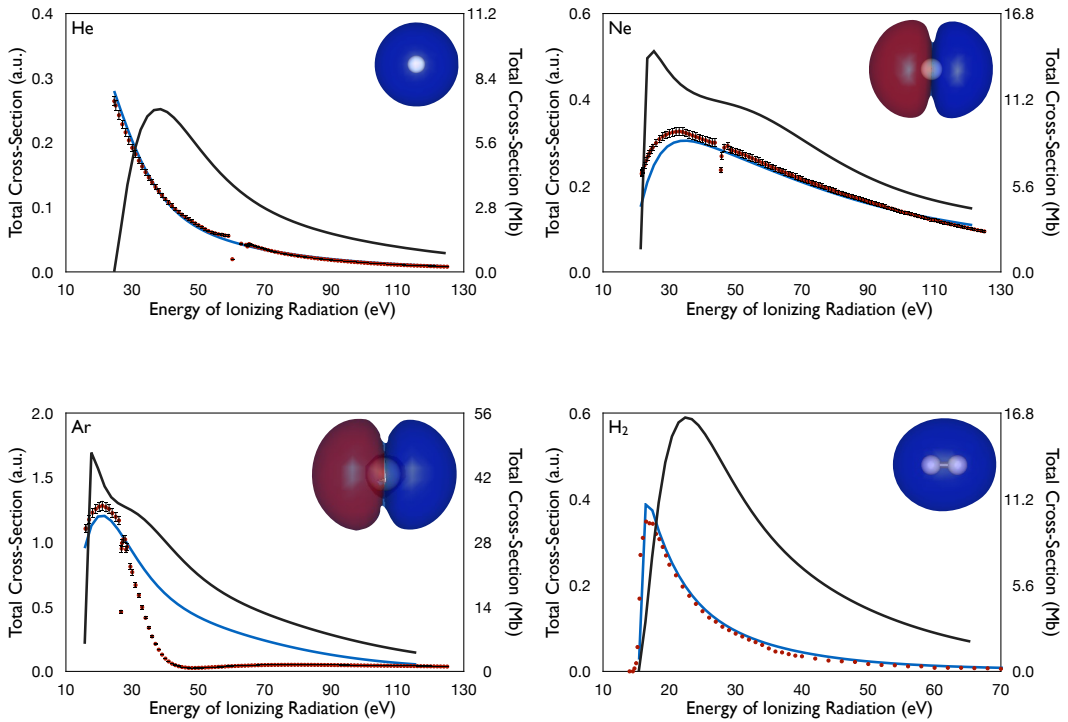


Figure 3.3: Absolute cross-sections for photoionization from He, Ne, Ar, and H₂. Red dots are experimental cross-sections^{58,61}. Black and blue curves denote cross-sections computed using PWs and CWS, respectively. FCFs are included for H₂. For neon and argon, the aug-cc-pV6Z basis set was employed. The corresponding Dyson orbitals are shown in the top right corners.

We begin with formaldehyde, for which accurate experimental results are available⁶³. The results are shown in Fig. 3.5. The CW gives a step-function like shape, whereas the calculation based on PWs results in a gradually rising curve, which can be rationalized by the more oscillatory behavior of the CWS (Fig. 3.1 and Fig. 3.7 in Appendix). The experimental cross-section exhibits features seen in both PW and CW ($Z = 1$) calculations; the sharp rise of the cross-section at the ionization threshold is a feature of the CW, whereas the continuing gradual rise with increasing energy is a feature of the PW. Neither PW nor CW ($Z=1$) provides a good agreement with the

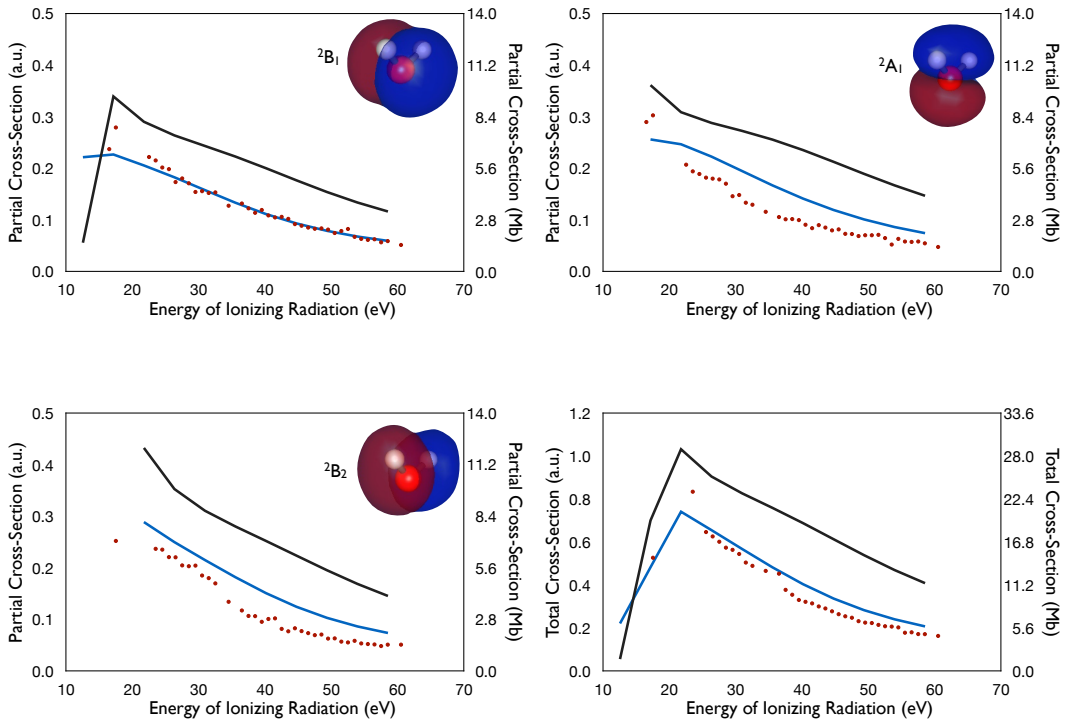


Figure 3.4: Absolute partial cross-sections for the three lowest ionized states of water, and the total absolute cross-section (excluding contributions from the core-ionized state). Red dots are the experimental cross-sections⁶². Black and blue curves denote the cross-sections computed using PWs and CWs, respectively. FCFs are not included.

experiment. However, using CW with $Z=0.25$ leads to an excellent agreement, once FCFs are included, both at threshold and at higher energies. A possible reason for this is that the effective charge in the center of expansion is different from 1, as the hole is delocalized. Fig. 3.8(a) in the Appendix shows the location of the center of the expansion and partial charges in CH_2O^+ — as one can see, the position of the Dyson orbital centroid is significantly offset relative to the carbon atom hosting most of the positive charge.

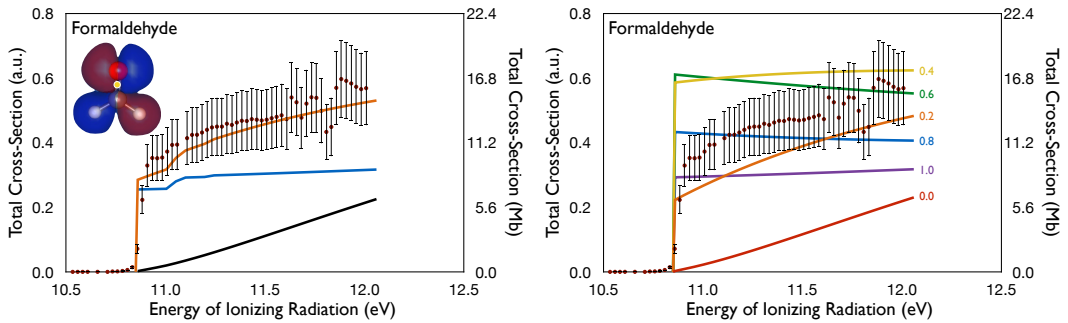


Figure 3.5: Left: Absolute cross-sections for formaldehyde photoionization. The experimental cross-section are shown as red dots⁶³. The computed values are shown by black (PW), blue (CW with $Z=+1$), and orange (CW with $Z=+0.25$). All computed curves include FCFs. **Right:** The cross-sections (without FCFs) using different values of Z .

Fig. 3.5 also shows the photoionization spectra of formaldehyde computed using different values of Z . It is clear that the energy dependence and absolute value of the electronic cross-section depends strongly on the effective charge. Interestingly, the changes in shape and magnitude of the cross-section profiles are not monotonic as Z changes from 0 to 1, such that spectra computed with CWs with intermediate values of Z do not lie between those computed with $Z=0$ and $Z=1$. These changes are driven by the shape of the photoelectron radial function, $R_l(kr)$. This is illustrated in Fig. 3.11 in the Appendix, where we plot $r_x \phi_{IF}^d$ along a one-dimensional cut for formaldehyde and $R_l(kr)$ for $l=1$ as a function of Z (we consider only $l=1$ since the outgoing electron is predominantly a p -wave in this case).

Fig. 3.6 and Fig. 3.9 (Appendix) show the computed and experimental cross-sections of other small organic molecules with relatively short FCF progressions. These molecules are ethylene, acetylene, propene, 1-butene, cis-2-butene, 1-butyne, methanol, and propyne. For ethylene and propene, two channels are accessible in the reported energy range. Mulliken charges for the ionized states in these systems are shown in Fig.

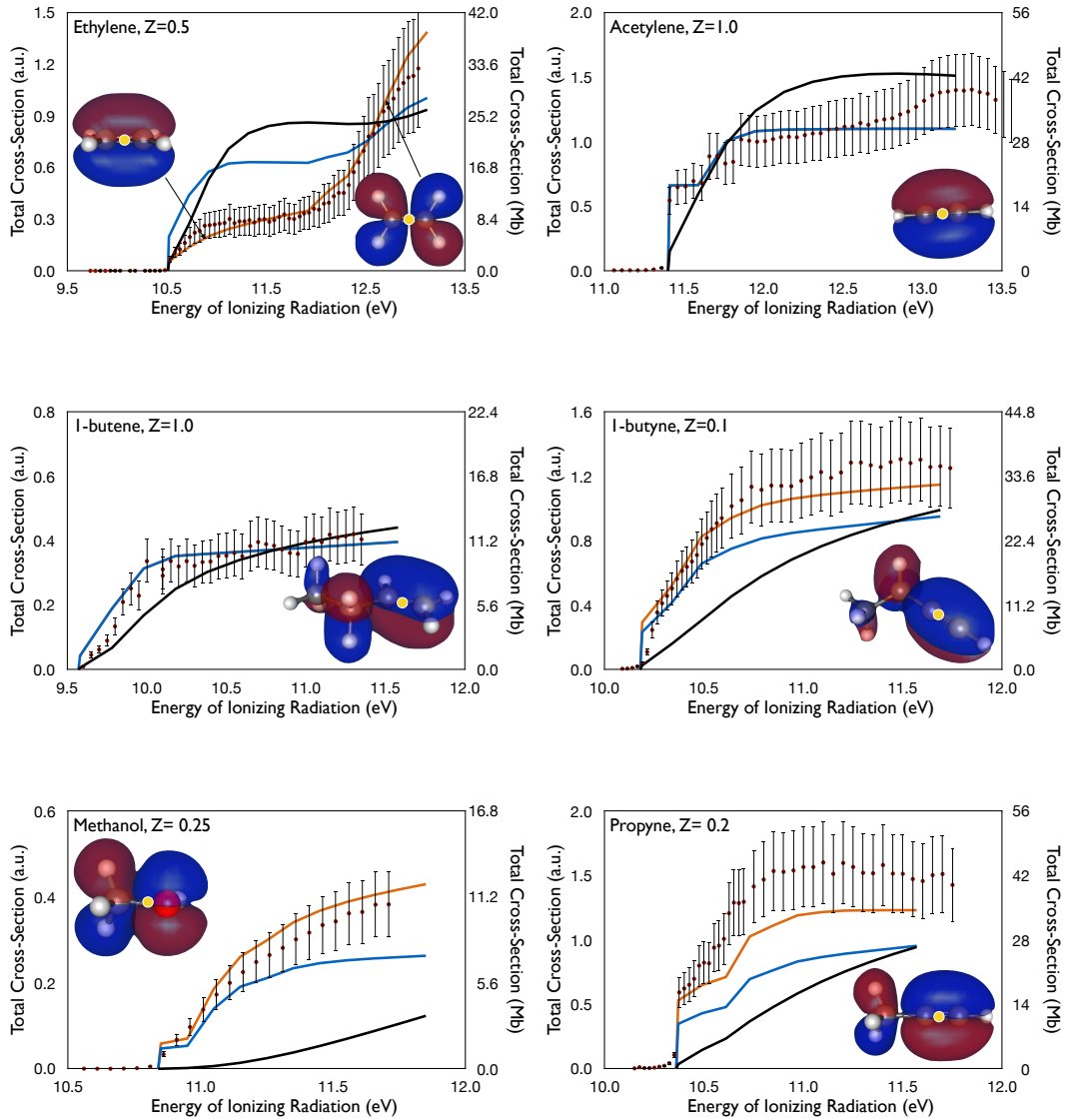


Figure 3.6: Absolute cross-sections for photoionization of ethylene, acetylene, 1-butene, 1-butyne, methanol, and propyne. For ethylene, two ionized states are accessed. The experimental cross-sections are shown as red dots. Experimental data are from Refs.⁶⁴ (for acetylene, ethylene, methanol, and propyne) and⁶⁵ (for 1-butene and 1-butyne). The computed values are shown using PW (black), CW (blue), and CW with a charge that gives the best fit with experiment (orange, if a good fit is not already obtained with PWs or CWs). All computed curves include FCFs. The Dyson orbitals and the center of expansion of the PW or CW (yellow circle) are also shown.

3.8 in Appendix (with hydrogen charges summed onto heavy atoms). While in some cases (e.g., acetylene and 1-butene) good agreement with experiment is obtained using CWs with $Z=1$, for most systems a better fit is obtained by using CWs with a partial effective charge. In the case of multiple channels (ethylene and propene), the resulting total cross-section can be reproduced by using the same effective charge for each channel, which is perhaps fortuitous since we would expect the appropriate choice of partial charge to be dependent on the final state accessed in photoionization. Fig. 3.10 compares the cross-section profiles computed with and without FCFs to elucidate the effect of FCFs on the cross-section profiles. Again, we emphasize good agreement between theory and experiment near the threshold, which can be important for identification of isomers.

To summarize, this work investigated photoionization/photodetachment cross-sections in small neutral (He, Ne, Ar, H₂) and anionic (H⁻, Li⁻, NH₂⁻) systems, as well as neutral molecular systems. We find that we can accurately reproduce the experimental spectra for these systems by using the formalism derived within the strong orthogonality assumption using EOM-IP-CCSD Dyson orbitals along with a single-center expansion of the wave function of the photoejected electron. However, whereas in the anions the photoelectron wave function can be treated as a PW, in the neutral systems the photo-electron must be treated using CWs (with $Z=1$) to account for the electrostatic interaction between the photoelectron and remaining core. Our results also illustrate that for photoionization from larger neutral molecules, a relatively simple single-center expansion of the free-electron wave function appears to provide a reasonable description of the state of the ejected electron, allowing one to compute cross-sections that are in good agreement with the experiment. However, the effective charge for the CW that gives the

best agreement with the experiment is not always unity. The experimental photoionization spectra often have features that resemble spectra computed both with PWs and with full ($Z=1$) CWs. For example, in formaldehyde the cross-section rises sharply at the threshold (as in the cross-sections computed with full CW), but then continues to rise gradually after that as in the PW. This is likely because the photoelectron wave is blind to the charge located far away from the expansion center (which is determined by the centroid of the Dyson orbital, in order to partially satisfy the strong orthogonality condition). This is an important result that shows that neither PW nor CW by themselves provide an adequate description of the ejected electron. Also, the generally good nature of the results suggests that our simple model, which is based on the strong orthogonality assumption, does capture the essential physics even though it neglects the non-spherical symmetry of the electrostatic potential, as well as the correlation and exchange interactions of the ejected electron with the core. Thus, we conclude that accurate photoionization cross-sections for molecules can be computed by using a modified central potential model that accounts for non-spherical charge distribution of the core by adjusting the charge in the center of the expansion. Contrary to the Stieltjes scheme^{28,29,31}, the present approach is vastly cheaper since it does not require calculations with very large basis sets, finding large number of approximate eigenstates (e.g., via block Lanczos diagonalization), or solving the moments problem to recover the cumulative oscillator strength for photoionization. This result is of both fundamental and practical importance. On the fundamental side, it shows that the strong orthogonality assumption is justified and that exchange and correlation interactions of the photoelectron with the core have relatively weak effects on the cross-section. On the practical side, this finding provides guidance for future theoretical developments. It suggests that this simple ansatz correctly captures underlying physical behavior and can, therefore, be used as a

starting point for developing a predictive model for computing photoionization cross-sections. What is needed is a procedure for determining the optimal charge Z . We propose variational optimization of this parameter by using numerical solutions of a one-particle Schrödinger equation with a non-spherical Coulomb potential described by the electrostatic potential, $V^{el}(R, r)$, of the ionized system:

$$\frac{\delta}{\delta Z} \left[\frac{\langle \Psi(Z) | H^C | \Psi(Z) \rangle_L}{\sqrt{\langle \Psi(Z) | \Psi(Z) \rangle_L \langle H^C \Psi(Z) | H^C \Psi(Z) \rangle_L}} \right] = 0, \quad (3.7)$$

where $H^C \equiv T_k + V^{el}(R, r)$ and $\Psi(Z)$ is CW with charge Z , and the integration is done over a finite box of size L . The expression in square brackets in Eq. (4.24) is maximized for $\Psi(Z)$ which is the closest approximation to an eigenstate of H^C . For example, if V^{el} is just the Coulomb potential created by point charge Z placed in the center of the expansion, the value of the expression in Eq. (4.24) equals 1 when $\Psi(Z)$ is a CW with charge Z , since that is the exact solution. The exploratory calculations for formaldehyde using this criterion (see Appendix) are encouraging. This full implementation and detailed benchmarks will be pursued in future work.

3.2 Appendix A: Detailed comparison between PW and CW for $l=0-5$, Mulliken charges in ionized species, photoionization cross-sections for selected molecules with and without FCFs, comparison between photoelectron radial functions with different Z with formaldehyde's Dyson orbital

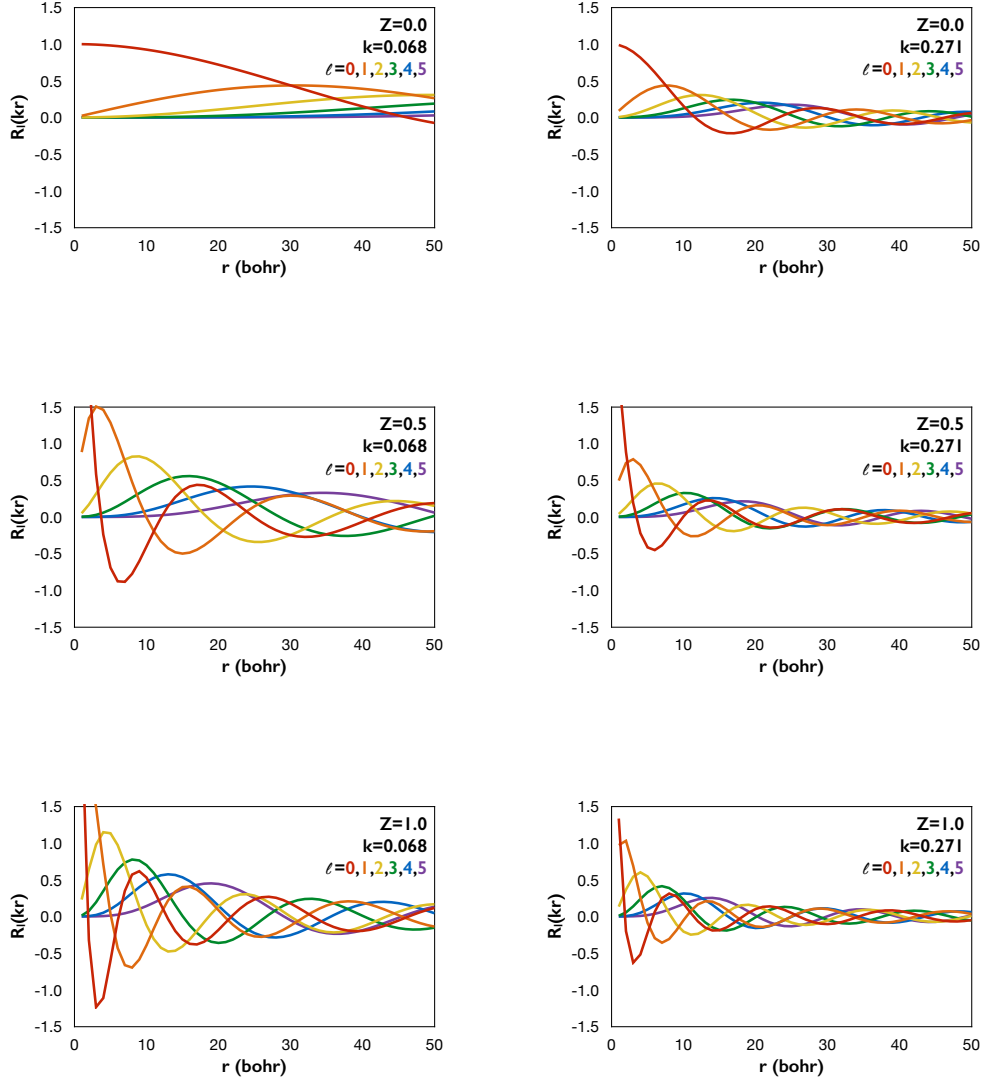


Figure 3.7: Coulomb radial functions for $l=0-5$ and for two different wave vector values, $k=0.068$ a.u. ($E_k=0.0625$ eV) and 0.271 a.u. ($E_k=1.0$ eV).

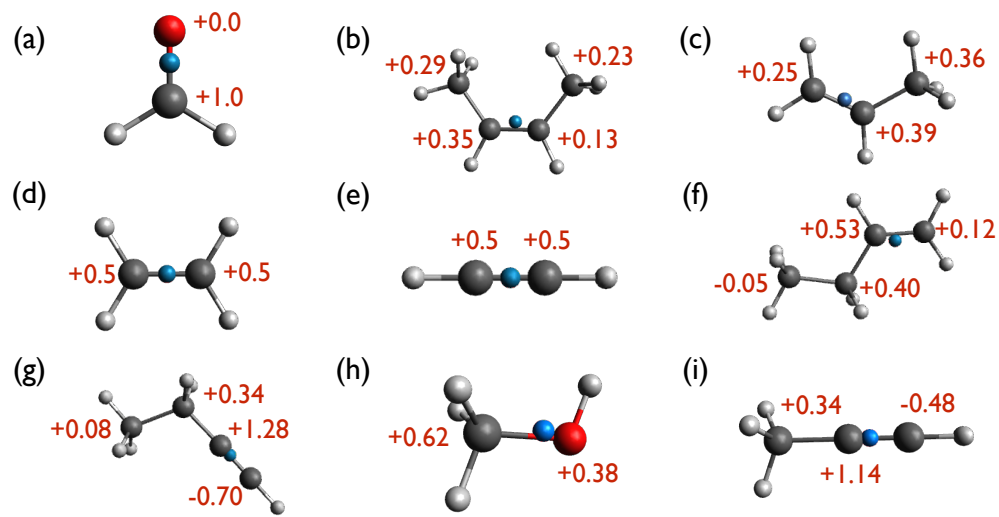


Figure 3.8: Mulliken charges (with hydrogen charges summed onto heavy atoms) for (a) formaldehyde, (b) *cis*-2-butene, (c) propene, (d) ethylene, (e) acetylene, (f) 1-butene, (g) 1-butyne, (h) methanol, (i) propyne. The blue spheres show the centers of the expansion of the photoelectron wave function.

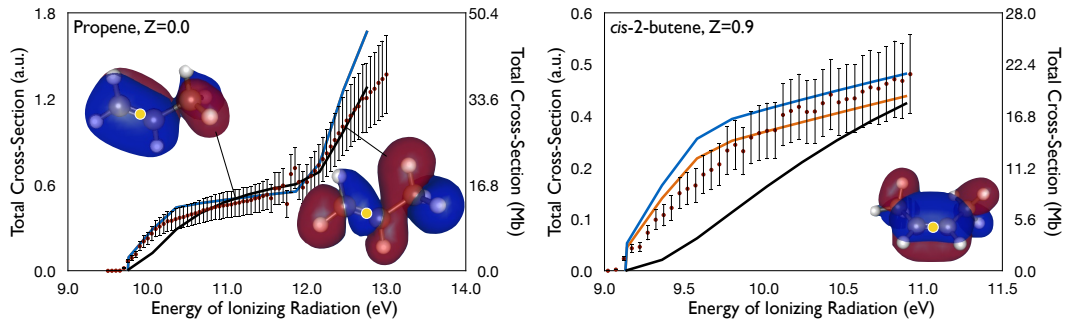


Figure 3.9: Absolute cross-sections for photoionization of propene and *cis*-2-butene. The experimental cross-sections are shown as red dots. The computed values are shown using plane wave (black), Coulomb wave (blue), and Coulomb wave with a charge that gives the best fit with experiment (orange, if a good fit is not already obtained with Coulomb or plane waves). The computed curves include FCFs. Note that our calculations indicate that the second ionized state of propene has vanishing FCFs and, therefore, does not contribute to the cross section. The state shown in this figure is the third ionized state of propene. The Dyson orbitals and the center of expansion of the plane or Coulomb wave (yellow circle) are also shown.

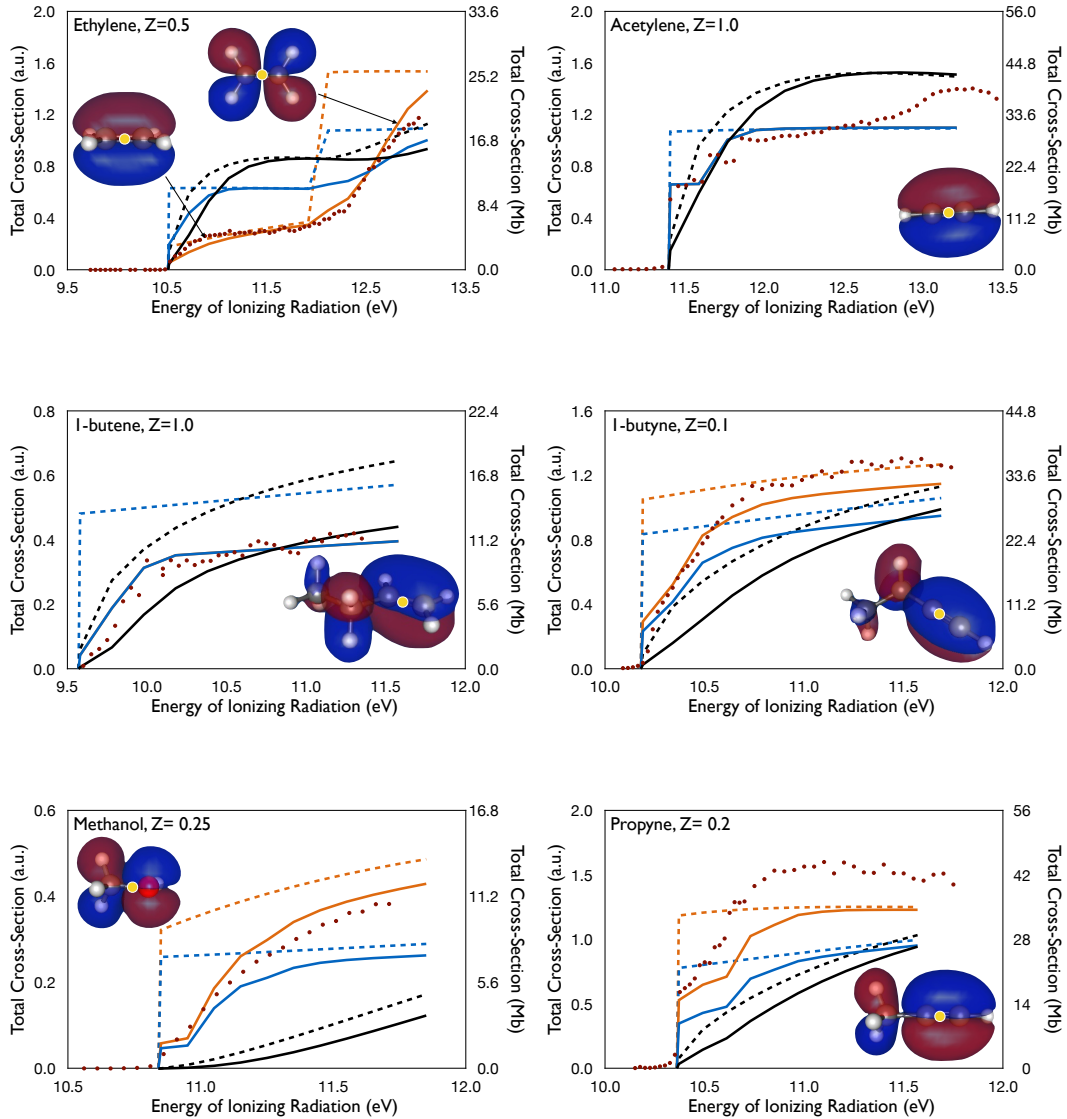


Figure 3.10: Absolute cross-sections for ethylene, acetylene, 1-butene, 1-butyne, methanol, and propyne. The computed values use a plane wave (black), Coulomb wave (blue), and a Coulomb wave with the charge that gives the best fit to the experiment (orange), if a good fit is not already obtained with Coulomb or plane waves. Solid and dashed lines denote the cross-sections computed with and without FCFs, respectively.

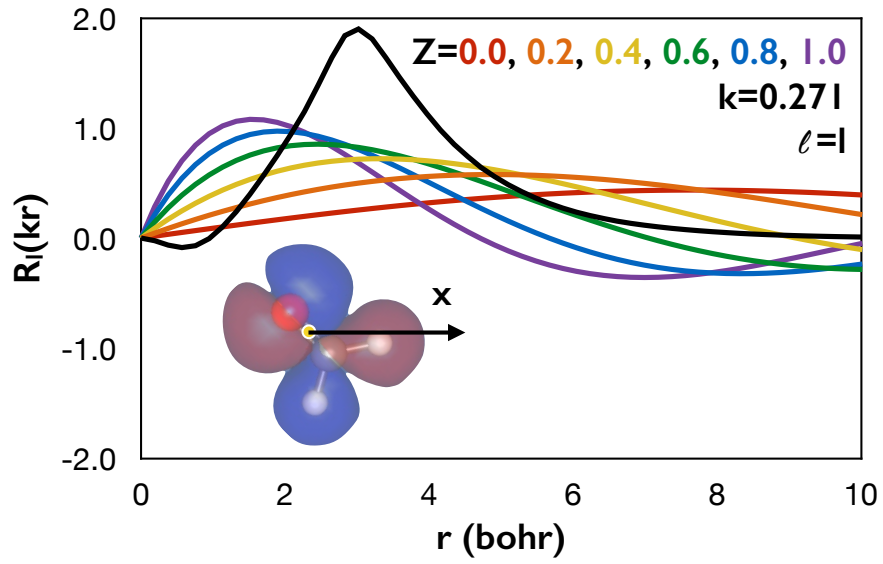


Figure 3.11: Coulomb radial functions for $l=1$ and for $k=0.271$ a.u. ($E_k=1.0$ eV) with varying Z . Black line shows a cut along the left Dyson orbital for formaldehyde in the x -direction (as shown in the figure). The value of the Dyson orbital is multiplied by x to give $r_x\phi_{IF}^d$ and magnified by a factor of 4 for clarity. As one can see, $l=0.4-0.6$ provide the biggest contribution to the cross-sections for formaldehyde.

3.3 Appendix B: Using variational optimization to determine the optimal charge: Formaldehyde example

Here we present a model calculation of the optimal charge, Z , using the variational criterion given by Eq. (4.24) in the main text. The physical rationale for Eq. (4.24) is that when $\Psi(Z)$ is an eigenstate of H^C , $H\Psi^Z$ is parallel to $\Psi(Z)$ leading to the maximal overlap between the two. We propose to solve this three-dimensional equation numerically, on the grid. V^{el} can be approximated by a Coulomb field due to the point charges, or described more accurately, using electron density of the cation. To provide proof-of-principle, here we present exploratory calculations performed with *Mathematica* using a one-dimensional model and point-charge potential. We use formaldehyde as a test case. As shown in Fig. 3.8, the formaldehyde cation has most of its positive charge localized on the carbon atom. The center of expansion of the photoelectron wave function is at the centroid of the Dyson orbital, which lies near the center of the carbon-oxygen bond. Thus, V^{el} can be approximated by a Coulomb attraction due to a +1 point charge displaced by a distance \mathbf{d} from the center of expansion of Ψ^{el} (\mathbf{d} here represents the distance to the carbon atom, or the hydrogen atoms, depending on where we assume the positive charge to be):

$$V(r) = \frac{-1}{\sqrt{r^2 + d^2}}. \quad (3.8)$$

The point charge is placed in a perpendicular dimension to \mathbf{r} , to avoid singularities in Ψ^{el} . In this arrangement, the potential energy term is spherically symmetric, which

preserves the separation of variables and allows us to reduce the problem to a one-dimensional Schrödinger equation for the radial part, $R(r)$:

$$\left[-\frac{1}{2} \frac{d^2}{dr^2} - \frac{1}{r} \frac{d}{dr} + \frac{l(l+1)}{2r^2} - \frac{1}{\sqrt{r^2 + d^2}} \right] R(r) = ER(r) \quad (3.9)$$

Since in formaldehyde the photoelectron is almost exclusively a p -wave, here we consider $l=1$.

In order to find a Coulomb radial function that best represents the solution to the radial equation above, we vary Z to find the CW, $R_c(Z, r)$, that best satisfies the eigenvalue problem in Eq. (3.9), i.e., the CW that changes the least upon applying the radial Hamiltonian. This is done by computing the following:

$$\left[-\frac{1}{2} \frac{d^2}{dr^2} - \frac{1}{r} \frac{d}{dr} + \frac{l(l+1)}{2r^2} - \frac{1}{\sqrt{r^2 + d^2}} \right] R_c(Z, r) = R_{c'}(Z, r) \quad (3.10)$$

$$\frac{\langle R_c(Z, r) | R_{c'}(Z, r) \rangle}{\sqrt{\langle R_c(Z, r) | R_c(Z, r) \rangle \langle R_{c'}(Z, r) | R_{c'}(Z, r) \rangle}} \quad (3.11)$$

We then maximize expression (3.11) by varying Z . If $R_c(Z, r)$ is an exact eigenfunction of Eq. (3.10), the overlap in Eq. (3.11) equals 1. Note that the eigenvalue is absorbed into $R_{c'}(Z, r)$.

Fig. 3.12 shows the value of Eq. (3.11) as a function of Z for the displaced point-charge model. The integration is performed over a grid size of 30 bohr. We consider $d=1.02$ bohr (corresponding to the distance between the centroid of the Dyson orbital in formaldehyde and the carbon atom). We also look at the effect of a point charge displaced by $d=2.93$ bohr (corresponding to the distance between the Dyson orbital centroid and the hydrogen atoms). We find in both cases that the best overlap is achieved for $Z = \sim 0.2$ – 0.3 , which is in good agreement with $Z=0.25$ obtained by from the best fit

of the computed cross-section to the experimental curve. Note that the optimal Z is not very sensitive to the magnitude of the wave vector k , which is consistent with the fact that the same value of Z reproduces almost the entire photoionization spectrum of formaldehyde.

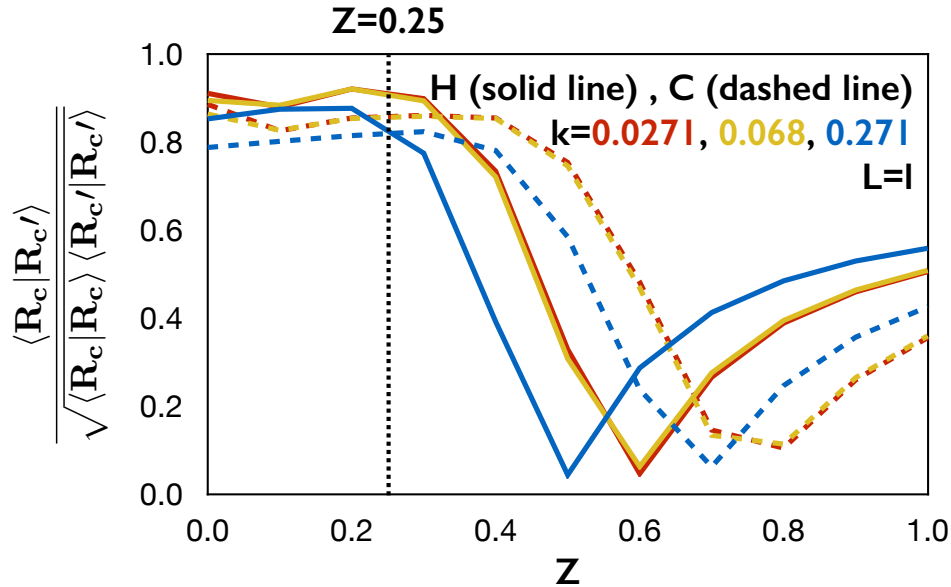


Figure 3.12: The value of Eq. (3.11) computed for CW with different values of Z using displaced point-charge Coulomb potential. Two values of d are considered: one corresponding to placing the charge on the carbon atom (dashed lines) and one at the distance of the hydrogens (solid lines). For both models, we consider Coulomb functions with different k spanning a 40-fold change in kinetic energy.

3.4 Chapter 3 references

- [1] J. Simons. Detachment processes for molecular anions. In C.Y. Ng, editor, *Photoionization and Photodetachment*, volume 10, Part II of *Advanced Series in Physical Chemistry*. World Scientific Publishing Co., Singapore, 2000.
- [2] A. Sanov and R. Mabbs. Photoelectron imaging of negative ions. *Int. Rev. Phys. Chem.*, 27:53–85, 2008.
- [3] K.L. Reid. Picosecond time-resolved photoelectron spectroscopy as a means of gaining insight into mechanisms of intramolecular vibrational energy redistribution in excited states. *Int. Rev. Phys. Chem.*, 27:607–628, 2008.
- [4] O. Welz, J.D. Savee, D.L. Osborn, S.S. Vasu, C.J. Percival, D.E. Shallcross, and C.A. Taatjes. Direct kinetic measurements of Criegee intermediate (CH_2OO) formed by reaction of CH_2I with O_2 . *Science*, 335:204–207, 2012.
- [5] D.M. Neumark. Probing the transition state with negative ion photodetachment: experiment and theory. *Phys. Chem. Chem. Phys.*, 7:433, 2005.
- [6] D.M. Neumark. Probing chemical dynamics with negative ions. *J. Chem. Phys.*, 125:132303, 2006.
- [7] J. Linderberg and Y. Öhrn. *Propagators in quantum chemistry*. Academic, London, 1973.
- [8] J.V. Ortiz. Toward an exact one-electron picture of chemical bonding. *Adv. Quantum Chem.*, 35:33–52, 1999.
- [9] H.R. Hudock, B.G. Levine, A.L. Thompson, H. Satzger, D. Townsend, N. Gador, S. Ulrich, A. Stolow, and T.J. Martínez. Ab initio molecular dynamics and time-resolved photoelectron spectroscopy of electronically excited uracil and thymine. *J. Phys. Chem. A*, 111:8500–8598, 2007.
- [10] C.M. Oana and A.I. Krylov. Dyson orbitals for ionization from the ground and electronically excited states within equation-of-motion coupled-cluster formalism: Theory, implementation, and examples. *J. Chem. Phys.*, 127:234106, 2007.
- [11] H.A. Bethe and E.E. Salpeter. *Quantum mechanics of one and two electron atoms*. Plenum, New York, 1977.

- [12] K.J. Reed, A.H. Zimmerman, H.C. Andersen, and J.I. Brauman. Cross sections for photodetachment of electrons from negative ions near threshold. *J. Chem. Phys.*, 64:1368–1375, 1976.
- [13] A.I. Krylov. Equation-of-motion coupled-cluster methods for open-shell and electronically excited species: The hitchhiker’s guide to Fock space. *Annu. Rev. Phys. Chem.*, 59:433–462, 2008.
- [14] K. Sneskov and O. Christiansen. Excited state coupled cluster methods. *WIREs Comput. Mol. Sci.*, 2:566, 2012.
- [15] R.J. Bartlett. Coupled-cluster theory and its equation-of-motion extensions. *WIREs Comput. Mol. Sci.*, 2(1):126–138, 2012.
- [16] J.F. Stanton and J. Gauss. Analytic energy derivatives for ionized states described by the equation-of-motion coupled cluster method. *J. Chem. Phys.*, 101(10):8938–8944, 1994.
- [17] J.F. Stanton and J. Gauss. A simple scheme for the direct calculation of ionization potentials with coupled-cluster theory that exploits established excitation energy methods. *J. Chem. Phys.*, 111:8785–8788, 1999.
- [18] P.A. Pieniazek, S.A. Arnstein, S.E. Bradforth, A.I. Krylov, and C.D. Sherrill. Benchmark full configuration interaction and EOM-IP-CCSD results for prototypical charge transfer systems: Noncovalent ionized dimers. *J. Chem. Phys.*, 127:164110, 2007.
- [19] S. Han and D.R. Yarkony. A Lippmann-Schwinger approach for the determination of photoionization and photodetachment cross sections based on a partial wave Green’s function expansion and configuration interaction wave functions. *Mol. Phys.*, 110:845–859, 2012.
- [20] J.G. Underwood and K.L. Reid. Time-resolved photoelectron angular distributions as a probe of intramolecular dynamics: Connecting the molecular frame and the laboratory frame. *J. Chem. Phys.*, 113:1067–1074, 2000.
- [21] G. Fronzoni, M. Stener, and P. Decleva. Valence and core photoionization dynamics of acetylene by TD-DFT continuum approach. *Chem. Phys.*, 298:141–153, 2004.
- [22] N. Rohringer, A. Gordon, and R. Santra. Configuration-interaction-based time-dependent orbital approach for ab initio treatment of electronic dynamics in a strong optical laser field. *Phys. Rev. A*, 74(4):043420, 2006.
- [23] X. Chu. Time-dependent density-functional-theory calculation of strong-field ionization rates of H₂. *Phys. Rev. A*, 82:023407, 2010.

- [24] A.P.P. Natalense and R. R. Lucchese. Cross section and asymmetry parameter calculation for sulfur 1s photoionization of SF₆. *J. Chem. Phys.*, 111:5344, 1999.
- [25] P.W. Langhoff. Stieltjes-Tchebycheff moment-theory approach to molecular photoionization studies. In V. McKoy T. Rescigno and B. Schneider, editors, *Electron Molecule and Photon Molecule Collisions*, pages 183–224. Plenum, New York, 1979.
- [26] I. Cacelli, R. Moccia, and A. Rizzo. Gaussian-type-orbital basis sets for the calculation of continuum properties in molecules: The differential photoionization cross section of molecular nitrogen. *Phys. Rev. A*, 57:1895–1905, 1998.
- [27] J. Cukras, P. Decleva, and S. Coriani. A coupled-cluster study of photodetachment cross sections of closed-shell anions. *J. Chem. Phys.*, 141:174315, 2014.
- [28] J. Cukras, S. Coriani, P. Decleva, O. Christiansen, and P. Norman. Photoionization cross section by Stieltjes imaging applied to coupled cluster Lanczos pseudo-spectra. *J. Chem. Phys.*, 139:094103, 2013.
- [29] M. Ruberti, R. Yun, K. Gokhberg, S. Kopelke, L.S. Cederbaum, F. Tarantelli, and V. Averbukh. Total molecular photoionization cross-sections by algebraic diagrammatic construction-Stieltjes-Lanczos method: Benchmark calculations. *J. Chem. Phys.*, 139:144107, 2013.
- [30] A. Dreuw and M. Wormit. The algebraic diagrammatic construction scheme for the polarization propagator for the calculation of excited states. *WIREs Comput. Mol. Sci.*, 5:82–95, 2015.
- [31] M. Ruberti, V. Averbukh, and P. Decleva. B-spline algebraic diagrammatic construction: Application to photoionization cross-sections and high-order harmonic generation. *J. Chem. Phys.*, 141:164126, 2014.
- [32] J. Cooper and R.N. Zare. Angular distribution of photoelectrons. *J. Chem. Phys.*, 48:942–943, 1968.
- [33] C.M. Oana and A.I. Krylov. Cross sections and photoelectron angular distributions in photodetachment from negative ions using equation-of-motion coupled-cluster Dyson orbitals. *J. Chem. Phys.*, 131:124114, 2009.
- [34] E. Surber, R. Mabbs, and A. Sanov. Probing the electronic structure of small molecular anions by photoelectron imaging. *J. Phys. Chem. A*, 107:8215–8224, 2003.
- [35] M.L. Weichman, J.B. Kim, J.A. DeVine, D.S. Levine, and D.M. Neumark. Vibrational and electronic structure of the α - and β -naphthyl radicals via slow photo-electron velocity-map imaging. *J. Am. Chem. Soc.*, 137:1420–1423, 2015.

- [36] P.V. Demekhin, A. Ehresmann, and V.L. Sukhorukov. Single center method: A computational tool for ionization and electronic excitation studies of molecules. *J. Chem. Phys.*, 134:024113, 2011.
- [37] R.F. Fink, M.N. Piancastelli, A.N. Grum-Grzhimailo, and K. Ueda. Angular distribution of Auger electrons from fixed-in-space and rotating $\text{C}1s \rightarrow 2\pi$ photoexcited CO: Theory. *J. Chem. Phys.*, 130:014306, 2009.
- [38] H. Siegbahn, L. Asplund, and P. Kelfve. The Auger electron spectrum of water vapour. *Chem. Phys. Lett.*, 35:330–335, 1975.
- [39] D.M. Bishop. Single-center molecular wave functions. *Adv. Quantum Chem.*, 3:25–59, 1967.
- [40] S. Han and D.R. Yarkony. On the determination of intensities for electron photodetachment and photoionization spectra involving states coupled by conical intersections: Total integral cross sections for polyatomic molecules. *J. Chem. Phys.*, 133:194107, 2010.
- [41] S. Han and D.R. Yarkony. Determining partial differential cross sections for low-energy electron photodetachment involving conical intersections using the solution of a Lippmann-Schwinger equation constructed with standard electronic structure techniques. *J. Chem. Phys.*, 134:174104, 2011.
- [42] S. Han and D.R. Yarkony. On the determination of partial differential cross sections for photodetachment and photoionization processes producing polyatomic molecules with electronic states coupled by conical intersections. *J. Chem. Phys.*, 134:134110, 2011.
- [43] D.M. Gingrich. *Practical Quantum Electrodynamics*. CRC Press, 2006.
- [44] J.J. Sakurai. *Modern Quantum Mechanics*. Addison-Wesley Publishing Company, 1995.
- [45] L.D. Landau and E.M. Lifshitz. *Quantum Mechanics: Non-relativistic theory*. Pergamon, Oxford, 1977.
- [46] T.-C. Jagau, D. Zuev, K.B. Bravaya, E. Epifanovsky, and A.I. Krylov. A fresh look at resonances and complex absorbing potentials: Density matrix based approach. *J. Phys. Chem. Lett.*, 5:310–315, 2014.
- [47] A. Bodi, P. Hemberger, D.L. Osborn, and B. Sztaray. Mass-resolved isomer-selective chemical analysis with imaging photoelectron photoion coincidence spectroscopy. *J. Phys. Chem. Lett.*, 4:2984–2952, 2013.

- [48] J.F. Lockyear, O. Welz, J.D. Savee, F. Goulay, A.J. Trevitt, C.A. Taatjes, D.L. Osborn, and S.R. Leone. Isomer specific product detection in the reaction of CH with acrolein. *J. Phys. Chem. A*, 11013–11026, 2013.
- [49] O. Welz, J. Zador, J.D. Savee, L. Sheps, D.L. Osborn, and C.A. Taatjes. Low-temperature combustion chemistry of n-butanol: Principal oxidation pathways of hydroxybutyl radicals. *J. Phys. Chem. A*, 117:11983–12001, 2013.
- [50] J.-D. Chai and M. Head-Gordon. Long-range corrected hybrid density functionals with damped atom-atom dispersion interactions. *Phys. Chem. Chem. Phys.*, 10:6615–6620, 2008.
- [51] Shao, Y.; Gan, Z.; Epifanovsky, E.; Gilbert, A.T.B.; Wormit, M.; Kussmann, J.; Lange, A.W.; Behn, A.; Deng, J.; Feng, X., et al. Advances in molecular quantum chemistry contained in the Q-Chem 4 program package. *Mol. Phys.*, 113:184–215, 2015.
- [52] S. Gozem and A.I. Krylov. ezDyson user's manual, 2015.
ezDyson, <http://iopenshell.usc.edu/downloads/>.
- [53] V.A. Mozhayskiy and A.I. Krylov. ezSpectrum.
ezSpectrum, <http://iopenshell.usc.edu/downloads/>.
- [54] H.J. Kaiser, E. Heinicke, R. Rackwitz, and D. Feldmann. Photodetachment measurements of alkali negative ions. *Z. Phys.*, 270:259–265, 1974.
- [55] S.J. Smith and D.S. Burch. Relative measurement of the photodetachment cross section for H^- . *Phys. Rev.*, 116:1125–1131, 1959.
- [56] K.C. Smyth and J.I. Brauman. Photodetachment of electrons from amide and arsenide ions: the electron affinities of $\text{NH}_2\cdot$ and $\text{AsH}_2\cdot$. *J. Chem. Phys.*, 56:4620–4625, 1972.
- [57] J.W. Cooper. Photoionization from outer atomic subshells. a model study. *Phys. Rev.*, 128:681–693, 1962.
- [58] J.A.R. Samson and W.C. Stolte. Precision measurements of the total photoionization cross-sections of He, Ne, Ar, Kr, and Xe. *J. Electron. Spectrosc. Relat. Phenom.*, 123:265–276, 2002.
- [59] J.P. Farrel, L.S. Spector, B.K. McFarland, P.H. Bucksbaum, M. Gühr, M.B. Gaarde, and K.J. Schafer. Influence of phase matching on the Cooper minimum in Ar high-order harmonic spectra. *Phys. Rev. A*, 83:023420, 2011.

- [60] H.J. Wörner, H. Niikura, J.B. Bertrand, P.B. Corkum, and D.M. Villeneuve. Observation of electronic structure minima in high-harmonic generation. *Phys. Rev. Lett.*, 102:103901, 2009.
- [61] C. Backx, G.R. Wight, and M.J. Van der Wiel. Oscillator strengths (10-70 eV) for absorption, ionization and dissociation in H₂, HD and D₂, obtained by an electron-ion coincidence method. *J. Phys. B*, 9:315, 1976.
- [62] K.H. Tan, C.E. Brion, P.E. Van Der Leeuw, and M.J. Van der Wiel. Absolute oscillator strengths (10-60 eV) for the photoabsorption, photoionization and fragmentation of H₂O. *Chem. Phys.*, 29:299–309, 1978.
- [63] L.G. Dodson, L. Shen, J.D. Savee, N.C. Eddingsaas, O. Welz, C.A. Taatjes, D.L. Osborn, S.P. Sander, and M. Okumura. VUV photoionization cross sections of HO₂, H₂O₂, and H₂CO. *J. Phys. Chem. A*, 119:1279–1291, 2015.
- [64] T.A. Cool, J. Wang, K. Nakajima, C.A. Taatjes, and A. McIlroy. Photoionization cross sections for reaction intermediates in hydrocarbon combustion. *Int. J. Mol. Sci.*, 247:18–27, 2005.
- [65] J. Wang, B. Yang, T.A. Cool, N. Hansen, and T Kasper. Near-threshold absolute photoionization cross-sections of some reaction intermediates in combustion. *Int. J. Mass Spectrom.*, 269:210–220, 2008.

Chapter 4: Probing electronic wave functions of sodium-doped clusters: Dyson orbitals, anisotropy parameters, and ionization cross-sections

4.1 Introduction

Photoionization and photodetachment experiments are broadly used in chemical physics^{1–3} for identification of transient reaction intermediates and for creating species that are otherwise unstable (radicals, molecules at transition states) in order to study their properties and spectroscopic signatures^{4–6}. Such experiments provide detailed information about the energy levels of the target systems and about the underlying wave functions. In particular, the cross-sections and photoelectron angular distributions encode the information about the Dyson orbital, a one-electron quantity characterizing the difference between the initial N and final $N-1$ electron wave functions (Ψ_I^N and Ψ_F^{N-1} , respectively)^{7–10}:

$$\phi_{IF}^d(1) = \sqrt{N} \int \Psi_I^N(1, \dots, n) \Psi_F^{N-1}(2, \dots, n) d2 \dots dn. \quad (4.1)$$

Within the dipole approximation and strong orthogonality assumption, Dyson orbitals contain all information about Ψ_I^N and Ψ_F^{N-1} needed for computing the so-called photo-electron matrix element:

$$D_k^{IF} = u \langle \phi_{IF}^d | r | \Psi_k^{el} \rangle, \quad (4.2)$$

where r is the dipole moment operator, u is a unit vector in the direction of the polarization of light, and Ψ_k^{el} is the wave function of the ejected electron. D_k^{IF} enters the expression of the total and differential cross-sections^{11,12} and is thus an experimental observable. Consequently, experimentally measured angular-resolved photoelectron spectra encode the information about the Dyson orbitals. However, reconstructing the orbital from the experimental measurements requires theoretical modeling^{10,13,14}. In addition to their connection to the experimental observables, Dyson orbitals are also of a qualitative value, as they enable simple molecular-orbital interpretation of the many-electron wave functions.

By virtue of Koopmans' theorem, Dyson orbitals within the Hartree-Fock or Kohn-Sham theory are just the canonical molecular orbitals. In the Koopmans' framework, possible multi-configurational character of the wave functions, dynamical electron correlation, and orbital relaxation are neglected (the latter can be included by computing Dyson orbitals using self-consistent field solutions of the N and $N-1$ electron systems). To account for these effects, Dyson orbitals¹³ can be computed within the equation-of-motion coupled-cluster (EOM-CC) framework^{15–17}, which provides accurate wave functions for closed-shell and various types of open-shell systems. In this paper, we consider photoionization from open-shell systems (doublet states), a situation which usually can be accurately described by the EOM-CC variant known as EOM-EA-CC (EOM-CC for electron attachment) in which the target closed-shell state is described

by the CC wave function and the initial open-shell state is described by EOM-EA. We employ EOM-EA-CC with single and double substitutions (EOM-EA-CCSD).

The focus of this paper is on quantifying the effect of electron correlation on the shape of the Dyson orbital and on the relevant experimental observables. In particular, we compare correlated EOM-EA-CCSD Dyson orbitals with Kohn-Sham and Hartree-Fock orbitals. As a model system, we consider sodium-doped clusters of ammonia and dimethylether (DME), which have been recently investigated experimentally^{18–20}. These systems^{18–22} provide a good model for solvated electrons^{23–26}.

Signorell and coworkers have reported^{18–20} angular-resolved photoelectron spectra of doped sodium clusters (water, ammonia, DME, methanol) of varying size (up to several hundreds of solvent molecules). In addition to trends in ionization energies (IEs), they characterized angular distributions of photoelectrons, providing a basis for determining how the shape of the solvated electron is affected by the cluster size and by the type of solvent.

In the case of one-photon photoionization from randomly oriented molecules, the photoelectron angular distribution (PAD) is completely characterized by a single parameter²⁷, β :

$$PAD(\theta) = \frac{\sigma}{4\pi} \left(1 + \frac{\beta}{2} (3\cos^2(\theta) - 1) \right). \quad (4.3)$$

The values of β range from 2 to -1: $\beta=2$ corresponds to the *p*-wave (ionization from *s*-like state) and $\beta=0$ corresponds to the fully isotropic photoelectron distribution.

Fig. 4.1 shows Dyson orbitals and the respective IEs for the four lowest electronic states of $\text{Na}(\text{NH}_3)_n$, $n=0-3$. As one can see, the unpaired electron resides on the surface of the clusters and its shape resembles an atomic *s* or *p* orbital. Compared to electrons solvated in neat clusters (such as $(\text{H}_2\text{O})_n^-$, Ref.²⁴), the binding energies are relatively high because the cluster core is positively charged, which is different from electrons

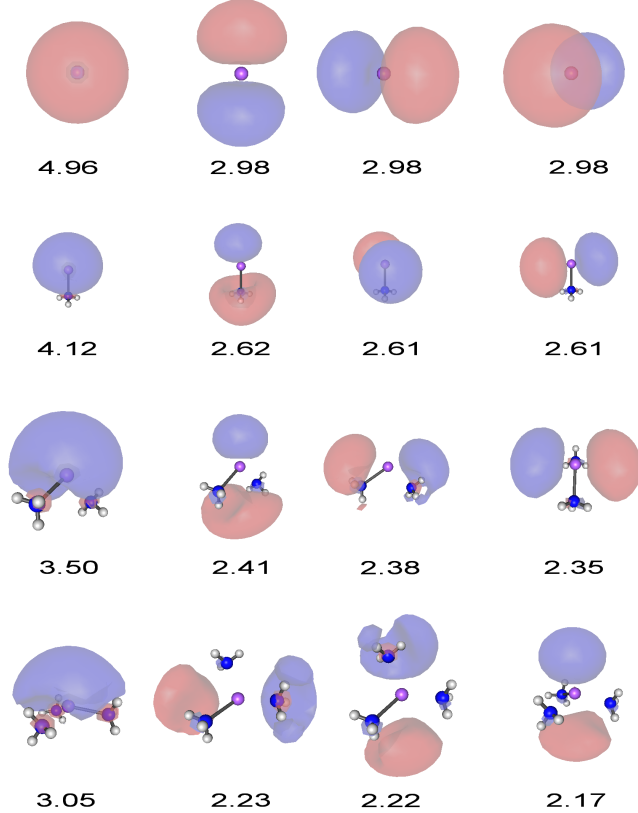


Figure 4.1: Dyson orbitals and the respective vertical ionization energies (eV) for the four lowest electronic states of bare sodium and $\text{Na}(\text{NH}_3)_n$, $n=1-3$, computed using the EOM-EA-CCSD/aug-cc-pVDZ wave functions.

in neutral clusters¹⁸. Thus, these Na-doped clusters are analogs of Rydberg molecular states in which a very diffuse electron is interacting with a positively charged core²⁸.

As one can see from Fig. 4.1, the solvent pushes the electron away from the positively charged Na and slightly distorts the shape of the orbital. It also breaks the degeneracy between the three p -states. By stabilizing the cation, solvation decreases the IE relative to bare Na, i.e., for the three smallest ammonia clusters, the IEs vary from 4.12-3.05 eV for the lowest electronic state, to be compared to 4.96 eV of bare Na.

Ref.¹⁸ reported that the IEs, as expected, decrease with the cluster size increase. Interestingly, the magnitude of the decrease is solvent-dependent and correlates with the

hydrogen-bonding ability of the solvents. Specifically, the steepest decrease in IE was observed for DME, and the smallest decrease was observed for water. The respective asymptotic values were around 1 eV (DME) and slightly below 4 eV (water). This trend was explained by an interplay between the stabilization of the cation and destabilization of the hydrogen-bond network of the solvent¹⁸. In solvents with strong hydrogen bonds (water, ammonia), the sodium cation perturbs the hydrogen-bond network, which partially offsets the energy gain due to the electrostatic interaction between $\text{Na}^{\delta+}$ and the solvent resulting in a smaller drop of vertical ionization energy (VIE). In other words, better solvation of $\text{Na}^{\delta+}$ leads to a weaker-bound solvated electron. This explanation is also consistent with the observed differences between vertical and adiabatic IEs, which can be loosely related to the solvent reorganization energies: in DME this difference is the smallest, indicating no significant reorganization of solvent upon electron ejection.

Anisotropy parameter β varied between 1.5 and slightly above zero in different solvents¹⁸. In DME clusters, the asymptotic β values were around 0.75, indicating substantial anisotropy even in very large clusters¹⁸. Taking into account reported isotropic distributions of photoelectrons from bulk-solvated Rydberg states²⁸, the results of Sig-norell and coworkers suggest that in the sodium-doped clusters the unpaired electrons reside on the surface of the cluster and no cavity states are formed¹⁸. The experimental results were complemented by calculations using DFT with the $\omega\text{B97X-D}$ functional¹⁸. The calculations agreed well with the observed trends in IEs and confirmed that the lowest state of the unpaired electron is indeed an *s*-type surface state. Larger deviations from a perfectly spherical shape were observed in larger clusters, consistently with the decrease in β with the cluster size increase. An earlier theoretical study investigated structures of solvated sodium clusters and pointed out the existence of multiple isomers²⁹ and also analyzed the shapes of their frontier orbitals.

Here we consider both energies and properties, with a focus on the shape of the electronic wave function and the related experimental observables such as photoelectron angular distributions. Using accurate Dyson orbitals as the reference, we assess the quality of Kohn-Sham DFT and Hartree-Fock orbitals. We analyze the shapes of Dyson orbitals, their spatial extent, and the average distance between the unpaired electron and Na (this quantity is related to the dipole moment of the cluster). To assess the effect of the changes in the shape of Dyson orbital on the experimental spectra, we compute anisotropies for the photoelectrons and total photoionization cross-sections. In addition to the lowest-energy structures, we analyze electronic properties along finite-temperature trajectories, to quantify the effect of thermal fluctuations on the observables.

4.2 Theoretical methods and computational details

4.2.1 Dyson orbitals within the equation-of-motion coupled-cluster framework

The EOM-CC approach provides an efficient and robust framework for computing multiple electronic states^{15–17,30–33}. The EOM-CC wave function has the following form:

$$|\Psi\rangle = Re^T |\Phi_0\rangle, \quad (4.4)$$

where linear EOM operator R acts on the reference CCSD wave function, $e^T |\Phi_0\rangle$. Operator T is an excitation operator satisfying the reference-state CC equations:

$$\langle \Phi_\mu | \bar{H} - E_{CC} | \Phi_0 \rangle = 0, \quad (4.5)$$

where Φ_μ are the μ -tuply excited determinants (with respect to the reference determinant, Φ_0) and $\bar{H} = e^{-T} H e^T$. μ is determined by the level of truncation of T , e.g., $\mu=1,2$ for CCSD. The reference determines the separation of the orbital space into the occupied and virtual subspaces. Here we use indices i, j, k, \dots and a, b, c, \dots to denote the orbitals from the two subspaces.

Different choices of the reference and the type of EOM operators enable access to different types of electronic states¹⁵. The character of target states is described with respect to the reference, Φ_0 . For solvated sodium clusters with one unpaired electron, the most appropriate choice is EOM-EA-CC (EOM-CC for electron-attached states). In the EOM-EA-CCSD variant, EOM operators R are of one-particle ($1p$) and two-particles-one-hole ($2p1h$) type:

$$R_1^{EA} = \sum_a r^a a^\dagger, \quad (4.6)$$

$$R_2^{EA} = \frac{1}{2} \sum_{iab} r_i^{ab} a^\dagger b^\dagger i, \quad (4.7)$$

and the reference corresponds to the closed-shell wave function (cationic, in the case of the sodium-doped clusters). Thus, in Eq. (4.1), Ψ_I^N and Ψ_F^{N-1} are the EOM-EA-CCSD and CCSD wave functions, respectively.

EOM amplitudes R and the corresponding energies are found by diagonalizing the similarity-transformed Hamiltonian, \bar{H} , in the space of target configurations defined by the choice of operator R and reference Φ_0 :

$$\bar{H}R = ER. \quad (4.8)$$

Since \bar{H} is a non-Hermitian operator, its left and right eigenstates, $\langle \Phi_0 | L^\dagger$ and $R|\Phi_0\rangle$, are not Hermitian conjugates, but form a biorthogonal set:

$$\bar{H}R|\Phi_0\rangle = ER|\Phi_0\rangle, \quad (4.9)$$

$$\langle \Phi_0 | L^\dagger \bar{H} = \langle \Phi_0 | L^\dagger E, \quad (4.10)$$

$$\langle \Phi_0 | L^M R^N |\Phi_0\rangle = \delta_{MN}, \quad (4.11)$$

where M and N denote the M th and N th EOM states and

$$L^{EA} = L_1^{EA} + L_2^{EA} = \sum_a l^a a^\dagger + \frac{1}{2} \sum_{iab} l_i^{ab} a^\dagger b^\dagger i. \quad (4.12)$$

The expansion coefficients, l^a , l_i^{ab} , r^a , and r_i^{ab} , are found by diagonalizing the corresponding matrix representation of \bar{H} . For energy calculations, only the knowledge of the right eigenstate is sufficient. However, in property calculations both the left and right eigenstates need to be computed. For example, the dipole moment for K th EOM-EA state is defined as follows:

$$\mu^K \equiv \langle \Phi_0 | L^{K\dagger} e^{-T} \mu e^T R^K |\Phi_0\rangle. \quad (4.13)$$

For transition properties, such as transition dipole moment (μ^{MN}) between two EOM-EA states, one needs to compute a geometric average:

$$\mu^{MN} = \sqrt{\langle \Phi_0 | L^{M\dagger} e^{-T} \mu e^T R^N |\Phi_0\rangle \langle \Phi_0 | L^{N\dagger} e^{-T} \mu e^T R^M |\Phi_0\rangle}. \quad (4.14)$$

Thus, in EOM-CC theory, we have left and right Dyson orbitals¹³. The differences between the two are small and for visualization we always show normalized right

orbitals^{13,34}; however, for cross-section calculations both right and left Dyson orbitals are needed^{10,14}.

To gain an insight into the electronic properties of solvated electrons, we analyze dipole moments, the spatial extent, and the shape of the underlying wave functions. The size of the wave function can be characterized by the expectation value of R^2 :

$$\langle \Psi^{EOM} | R^2 | \Psi^{EOM} \rangle = \langle \Psi^{EOM} | X^2 | \Psi^{EOM} \rangle + \langle \Psi^{EOM} | Y^2 | \Psi^{EOM} \rangle + \langle \Psi^{EOM} | Z^2 | \Psi^{EOM} \rangle. \quad (4.15)$$

Since the size of the electronic wave function increases with the system size, it is convenient to consider the difference between $\langle R^2 \rangle$ of the target EOM-EA state and the CCSD reference, as commonly done in the analysis of excited states³⁵:

$$\Delta R^\Psi \equiv \sqrt{|\langle \Psi^{EOM} | R^2 | \Psi^{EOM} \rangle - \langle \Psi^{CCSD} | R^2 | \Psi^{CCSD} \rangle|}. \quad (4.16)$$

In a similar fashion, one can consider changes in the individual Cartesian components, ΔR_α^Ψ , $\alpha=X,Y,Z$, which characterize the shape of the wave function. For example, the values of the ΔX , ΔY , and ΔZ are similar for *s*-like states, whereas *p*-like states can be identified by one large and two small components³⁵.

We also compute the properties of Dyson orbitals, which are more directly related to the unpaired electron¹³. The expectation values of \mathbf{R} give the centroid of the Dyson orbital, \mathbf{R}^d , and $\langle (\mathbf{R} - \mathbf{R}^d)^2 \rangle$ gives its size, \bar{R}^d :

$$R_\alpha^d \equiv \langle \phi^d | R_\alpha | \phi^d \rangle, \quad (4.17)$$

$$\bar{R}_\alpha^d \equiv \sqrt{\langle \phi^d | (R_\alpha - R_\alpha^d)^2 | \phi^d \rangle}, \quad (4.18)$$

$$\bar{R}^d = \sqrt{(\bar{R}_X^d)^2 + (\bar{R}_Y^d)^2 + (\bar{R}_Z^d)^2}, \quad (4.19)$$

where R_α denotes the three Cartesian components.

The distance between \mathbf{R}^d and the coordinates of the sodium atom, \mathbf{R}_{Na} , quantifies the offset between the Dyson orbital and the positively charged cluster core:

$$d_{eh} \equiv |\mathbf{R}^d - \mathbf{R}_{Na}|. \quad (4.20)$$

This distance between the average position of the unpaired electron and the positively charged hole can be compared with the dipole moment. Obviously, in bare Na, the two coincide and $d_{eh}=0$.

Note that the magnitudes of the individual Cartesian components of R^2 , \bar{R}^d , and μ depend on the choice of the coordinate system (or molecular orientation). Thus, in order to unambiguously describe the shape of the wave function, one should consider eigenvalues of the R^2 matrix rather than its diagonal matrix elements. However, the respective absolute values (ΔR^Ψ , \bar{R}^d , d_{eh}) are invariant to the molecular orientation, owing to the properties of the trace.

4.2.2 Cross-sections and photoelectron angular distributions

The expression for photodetachment/photoionization cross-section is¹¹:

$$\frac{d\sigma}{d\Omega_k} = \frac{4\pi^2}{c} \cdot E \cdot |D_k^{IF}(\theta, \phi)|^2, \quad (4.21)$$

where D_k^{IF} is the photoelectron dipole matrix element defined by Eq. (4.2).

To compute D_k^{IF} , one needs a Dyson orbital, Eq. (4.1), and the wave function of free electron, Ψ_k^{el} . The latter can be described by either a plane or a Coulomb wave expressed in the basis of spherical (partial) waves, $|E,l,m\rangle$ ³⁶:

$$\Psi_k^{el} = \sum_{l=0}^{\infty} \sum_{m=-l}^l |E,l,m\rangle \frac{1}{\sqrt{k}} Y_{lm}(\hat{k}). \quad (4.22)$$

Each partial wave can be written as a product of radial function R_{kl} and spherical harmonic Y_{lm} ³⁶:

$$|E,l,m\rangle = i^l \sqrt{\frac{2k}{\pi}} R_{kl}(r, Z) Y_{lm}(\theta, \phi). \quad (4.23)$$

The origin of the expansion is placed at the centroid of the Dyson orbital, which is equivalent to orthogonalizing the Dyson orbital to Ψ^{el} ^{10,14}. Radial functions, R_{kl} , depend on the effective charge Z . For $Z=0$ (as in the case of photodetachment from anions), R_{kl} is a spherical Bessel function and the photoelectron wave function is a plane wave. In photoionization of neutral species, the charge of the cationic core is +1 and R_{kl} is a Coulomb radial wave function with $Z=1$ ³⁷.

The performance of this model has been recently investigated using a benchmark set of anionic and neutral species¹⁴. In the case of neutral atoms and very small molecules, absolute total cross-sections are well reproduced by using Coulomb waves with $Z=1$. However, in polyatomic molecules the best agreement with experiment was achieved when using an effective charge $Z \in [0, 1]$, which accounts for non-point charge distribution in polyatomic cations (i.e., the outgoing electron is less sensitive to the charge located far away from the expansion center). The benchmarks¹⁴, which were performed in a broad energy range, provide numerical evidence in support of strong orthogonality assumption. In particular, the threshold behavior in anionic and neutral systems is correctly reproduced by the model¹⁴.

Once Dyson orbitals are computed, the calculations of the total and differential cross-sections can be performed by the *ezDyson* software³⁸. The details about averaging over molecular orientations and accounting for electronic degeneracies of the initial and target states can be found in the *ezDyson* manual³⁸.

To determine optimal charge Z , a variational approach was proposed in Ref.¹⁴:

$$\frac{\delta}{\delta Z} \left[\left| \frac{\langle \Psi(Z) | H^C | \Psi(Z) \rangle_L}{\sqrt{\langle \Psi(Z) | \Psi(Z) \rangle_L \langle H^C \Psi(Z) | H^C \Psi(Z) \rangle_L}} \right| \right] = 0, \quad (4.24)$$

where $H^C \equiv T_k + V^{el}(R, r)$ describes the Hamiltonian of the outgoing electron in the field of the cationic core characterized by Coulomb potential $V^{el}(R, r)$, $\Psi(Z)$ is the Coulomb wave with charge Z , and the integration is carried out over a finite box of size L . The expression in square brackets in Eq. (4.24) is maximized for $\Psi(Z)$ which is the best approximation to an eigenstate of H^C . While the general implementation of this approach is not yet available, in one-dimensional case one can easily optimize Z using Eq. (4.24) and a simple displaced point-charge model¹⁴. This procedure is employed here.

4.2.3 Computational details

Equilibrium geometries of the clusters were taken from Ref.¹⁸, where they were optimized with ω B97X-D/6-31+G(d). To investigate the effect of structural fluctuations on the electronic properties, we performed ab initio molecular dynamics (AIMD) calculations for selected clusters, followed by calculations of orbitals at selected snapshots. The AIMD calculations were performed using ω B97X-D/6-31+G(d) and $T=333$ K. The trajectories were initiated using optimized structures and the initial velocities were randomly sampled from the Maxwell-Boltzmann distribution at 333 K. AIMD trajectories

of 2.4 ps and 4.8 ps were calculated for Na(NH₃) and for Na(DME), respectively. For Na(NH₃)₄, Na(NH₃)₆ (in which several structural isomers are possible²⁹), Na(DME)₄, and Na(DME)₆ we computed longer trajectories (9.1-9.6 ps). The snapshots were taken each 120 fs for Na(NH₃), each 240 fs for Na(DME), and each 480 fs for all other systems. At selected snapshots, VIEs and properties were computed with EOM-EA-CCSD/aug-cc-pVDZ for all clusters except Na(DME)₆ for which ωB97X-D/6-31+G(d) was used. The method was chosen based on the overall performance of different functionals for the experimental observables in the entire range of photon energies (these results are shown in Fig. 4.33 and discussed in details below).

The following basis sets were used in the EOM-EA-CCSD calculations: 6-31+G(d) and n-aug-cc-pVXZ ($n=1-4$, X=D,T,Q). The effect of the basis set on the computed quantities (IE, β , σ_{tot} , \bar{R}) was investigated for NaX_{*n*}, *n*=1-3 (X=NH₃, DME). The results for Na(NH₃) are summarized in Appendix (Fig. 4.18). We observe a noticeable difference between the values computed with 6-31+G(d) and with Dunning's bases. The results computed with Dunning's bases show a systematic convergence with increasing the basis-set size (from aug- to q-aug-, from DZ to TZ to QZ). For NH₃ clusters, all quantities are converged with the triply augmented basis, while for DME, doubly augmented basis is sufficient for a given zeta. In general, for a given zeta, extra augmentation brings the results closer to those with higher zeta. These trends hold for various cluster sizes for the same solvent. In absolute terms, the changes beyond aug-cc-pVDZ are rather small – the variations in IEs and cross-sections do not exceed 0.03 eV and 10%, respectively. The β values at the experimental photon energy are also rather insensitive to the basis set increase beyond aug-cc-pVDZ. Thus, we employ the aug-cc-pVDZ basis for the rest of the calculations.

For larger clusters ($\text{Na}(\text{DME})_5$, $\text{Na}(\text{DME})_6$, and $\text{Na}(\text{DME})_7$), we employed a modified basis set (aug-cc-pVDZ on all heavy atoms and cc-pVDZ on H atoms) and froze the core and high-lying virtual orbitals (31, 37, and 43 virtual orbitals were frozen in $\text{Na}(\text{DME})_5$, $\text{Na}(\text{DME})_6$, and $\text{Na}(\text{DME})_7$, respectively). The errors introduced by these approximations were found to be negligible for $\text{Na}(\text{DME})_5$, as shown in Fig. 4.19 in Appendix.

All calculations were performed with the Q-Chem electronic structure program^{39,40}. Cross-sections and anisotropies were computed using the *ezDyson*^{10,38} code. The details for the cross-section and β calculations using *ezDyson* are given in the Appendix.

As shown in the Appendix (Fig. 4.17), the anisotropy parameter β depends on the effective charge Z at low energies. Even in small clusters (see Fig. 4.1), the Dyson orbitals are displaced from the positively charged core ($\text{Na}^{\delta+}$). As illustrated in Tables 4.1 and 4.2, the distance between the centroid of the Dyson orbital and the position of $\text{Na}^{\delta+}$ varies from 0.73 a.u. in the smallest cluster to 5.10 a.u. for $\text{Na}(\text{NH}_3)_9$. Because the positive charge is displaced from the center of expansion of the photoelectron wave function, we expect that the plane wave ansatz would be a reasonable approximation of Ψ^{el} for these systems, especially for larger clusters. To test this assumption, we computed optimal Z using a one-dimensional model based on Eq. (4.24). The results are shown in the Appendix (Fig. 4.16). We found that the optimal values of effective core charge Z are small. The deviation of optimal Z from zero is smaller for larger d and higher E_k , confirming that the quality of plane wave description improves for clusters with more solvent molecules. As one can see from Fig. 4.17, even for $n=1$ at the experimental energy of 4.66 eV, computed β 's show little variations whether a plane wave or a Coulomb wave with $Z=0.2\text{--}0.4$ is used, while the variations in the total absolute cross-sections can be larger — up to 50 % of the plane-wave value. Thus, for

these clusters one can use plane wave to represent Ψ^{el} ; this is done in all calculations below.

4.3 Results and discussion

4.3.1 Electronic properties of sodium-doped ammonia and DME clusters

Tables 4.1 and 4.2 collect the computed properties of the EOM-EA-CCSD states and the respective Dyson orbitals for the sodium-doped ammonia and DME clusters. As pointed out in Ref.¹⁸, these two solvents represent two very different situations. Ammonia can form hydrogen bonds, which are perturbed by the sodium cation. This effect counteracts energy gain due to solvation. Consequently, the solvent-induced change in IE is small and the electron is relatively weakly bound. In DME, which does not form hydrogen bonds, $\text{Na}^{\delta+}$ does not perturb the solvent and the electron binding energy is higher. We note that bulk DME does not dissolve Na, whereas bulk ammonia does, leading to production of the solvated electrons. Thus, the properties of solvated electrons produced in finite ammonia and DME clusters converge to different bulk limits.

Table 4.1: Electronic properties computed using the EOM-EA-CCSD/aug-cc-pVDZ wave functions for the $\text{Na}(\text{NH}_3)_n$ clusters, $n=1\text{-}10$. VIEs are given in eV and other quantities in a.u.

System	VIE	μ	ΔR^Ψ			\bar{R}^d			d_{eh}	f_L
			X	Y	Z	X	Y	Z		
$\text{Na}(\text{NH}_3)$	4.12	1.61	4.4	3.0	3.0	3.0	3.0	3.0	0.73	
	2.62	2.05	5.7	3.9	3.9	4.2	5.4	3.8	3.14	0.274
	2.61	0.97	4.1	5.5	3.5	5.2	3.7	3.4	0.02	0.295
	2.61	0.96	4.1	3.5	5.5	3.4	3.3	5.4	0.22	0.295

	1.69	-	-	-	-	-	-	-	-	0.034
Na(NH ₃) ₂	3.50	1.80	3.7	4.5	3.5	3.6	3.5	3.5	0.91	
	2.41	1.87	4.4	6.0	4.0	4.2	5.6	4.5	3.10	0.253
	2.38	0.48	6.8	4.2	3.9	4.6	4.7	5.9	0.52	0.318
	2.35	1.02	3.6	4.1	6.1	5.6	3.6	4.4	0.03	0.290
	1.52	-	-	-	-	-	-	-	-	0.032
Na(NH ₃) ₃	3.05	1.29	4.5	4.4	4.5	4.3	4.3	4.0	0.99	
	2.23	0.43	7.3	4.2	4.4	5.1	6.7	4.2	0.24	0.327
	2.22	0.50	4.4	7.3	4.4	6.7	5.1	4.2	0.39	0.326
	2.17	1.36	4.5	4.4	6.3	4.3	4.3	6.6	1.93	0.276
	1.36	-	-	-	-	-	-	-	-	0.027
Na(NH ₃) ₄	2.80	0.98	4.9	4.8	4.8	4.8	4.8	4.6	1.67	
	2.13	1.06	7.6	4.5	4.5	6.8	5.4	4.6	0.89	0.326
	2.10	0.45	4.6	7.6	4.6	5.5	6.4	5.1	0.71	0.332
	2.07	0.78	4.6	4.6	7.6	4.6	5.3	7.1	0.51	0.327
	1.20	-	-	-	-	-	-	-	-	0.001
Na(NH ₃) ₅	2.74	1.73	5.0	5.3	4.8	4.8	4.7	4.8	2.74	
	2.07	0.24	8.0	4.7	4.7	7.4	4.6	4.9	1.21	0.328
	2.04	2.51	4.9	7.7	4.8	4.8	6.3	5.9	1.71	0.295
	2.03	0.52	4.8	4.8	7.9	4.7	6.3	6.5	1.25	0.332
	1.25	-	-	-	-	-	-	-	-	0.000
Na(NH ₃) ₆	2.76	2.17	5.3	4.9	5.2	4.7	4.7	4.4	3.98	
	2.05	0.39	5.1	7.7	4.9	4.8	7.8	4.6	1.77	0.320
	2.04	0.49	7.5	4.8	5.7	7.4	4.9	5.6	2.21	0.332
	1.92	3.36	5.6	5.7	7.2	5.6	5.4	6.8	1.99	0.254
	1.24	-	-	-	-	-	-	-	-	0.010
Na(NH ₃) ₇	2.71	2.57	6.2	4.8	5.0	4.3	4.7	4.9	4.08	
	2.03	0.49	5.3	5.1	7.7	5.0	5.0	7.6	1.70	0.315
	1.98	0.59	5.9	7.7	5.1	5.5	7.6	4.9	2.00	0.322
	1.89	3.13	7.2	5.8	5.8	7.0	5.7	5.9	2.03	0.255
	1.21	-	-	-	-	-	-	-	-	0.010
Na(NH ₃) ₈	2.55	3.43	7.1	5.1	4.8	4.5	4.8	4.9	4.39	
	1.89	1.09	7.5	7.3	5.2	7.4	6.9	5.2	3.29	0.311

	1.86	1.45	5.8	5.1	8.1	5.3	5.0	7.8	2.06	0.294
	1.84	3.74	6.6	7.7	5.6	6.5	7.0	5.6	2.61	0.249
	1.18	-	-	-	-	-	-	-	-	0.004
Na(NH ₃) ₉	2.66	2.70	5.2	5.1	6.1	4.8	4.7	4.1	5.10	
	1.96	0.89	7.4	5.9	5.1	7.1	6.2	5.3	2.94	0.323
	1.92	1.10	6.5	7.4	5.6	6.5	7.2	4.8	2.91	0.318
	1.78	4.62	6.2	6.1	7.6	6.1	6.0	7.0	3.17	0.195
	1.28	-	-	-	-	-	-	-	-	0.011
Na(NH ₃) ₁₀	2.57	2.75	5.8	5.7	5.3	4.5	4.6	4.7	4.95	
	1.90	0.40	5.6	6.8	7.2	4.9	6.7	7.0	2.12	0.298
	1.83	4.39	6.3	7.3	6.5	5.4	6.6	6.2	3.81	0.216
	1.79	1.63	8.9	6.0	5.8	8.8	5.7	5.7	2.16	0.304
	1.27	-	-	-	-	-	-	-	-	0.025

Table 4.2: Electronic properties computed using the EOM-EA-CCSD/aug-cc-pVDZ wave functions for the Na(DME)_{*m*} clusters, *m*=1-7. Results for Na(DME)₅, Na(DME)₆, and Na(DME)₇ were obtained with modified basis set and reduced orbital space (see text). VIEs are given in eV and other quantities in a.u.

System	VIE	μ	ΔR^{Ψ}			\bar{R}^d			d_{eh}	f_L
			X	Y	Z	X	Y	Z		
Na(DME)	4.14	1.98	3.0	3.0	5.7	2.9	2.9	2.6	1.13	
	2.60	1.22	5.6	3.3	5.3	3.2	5.6	3.1	0.29	0.271
	2.55	1.18	3.3	5.7	5.3	5.6	3.3	3.2	0.21	0.276
	2.20	1.36	4.6	4.9	6.3	4.8	4.6	6.2	2.48	0.207
	1.80	-	-	-	-	-	-	-	-	0.100
Na(DME) ₂	3.56	2.78	3.3	6.0	3.2	3.0	2.6	3.2	1.86	
	2.32	1.53	3.9	5.2	6.2	3.6	3.4	6.2	0.39	0.233
	2.10	2.19	7.0	6.0	4.1	7.0	3.9	4.2	1.08	0.250
	2.01	4.22	5.8	5.9	6.0	5.7	5.4	6.0	5.91	0.057
	1.61	-	-	-	-	-	-	-	-	0.150
Na(DME) ₃	3.10	3.22	3.6	3.6	6.0	3.3	3.3	2.7	2.71	
	1.97	2.22	7.6	4.8	5.7	5.1	7.1	4.6	1.62	0.211

	1.95	2.10	4.9	7.7	5.7	7.1	5.3	4.8	1.32	0.210
	1.90	4.70	6.6	6.6	6.2	6.4	6.5	5.4	6.24	0.022
	1.50	-	-	-	-	-	-	-	-	0.090
Na(DME) ₄	2.69	3.92	4.0	3.9	6.4	3.3	3.6	2.9	3.50	
	1.89	5.06	6.8	6.5	6.7	6.0	5.7	6.5	6.80	0.012
	1.81	1.91	5.3	8.7	5.9	7.3	6.7	5.1	0.93	0.185
	1.74	1.29	9.5	5.7	6.2	5.8	5.7	9.2	0.67	0.140
	1.45	-	-	-	-	-	-	-	-	0.051
Na(DME) ₅	2.25	4.20	-	-	-	4.3	4.4	3.8	4.93	-
	1.77	-	-	-	-	6.6	6.3	6.8	5.37	-
	1.71	-	-	-	-	6.2	7.2	9.1	0.42	-
	1.66	-	-	-	-	9.9	6.2	6.0	0.38	-
Na(DME) ₆	1.89	0.00	-	-	-	7.2	7.2	7.2	0.00	-
Na(DME) ₇	1.84	2.76	-	-	-	6.9	7.3	6.9	3.34	-

Our results fully agree with those reported in Ref.¹⁸. Let us consider the trends in VIE for the lowest state. The VIE in the smallest cluster (one solvent molecule) are practically identical for NH₃ and DME: 4.12 eV and 4.14 eV. However, as the number of solvent molecules increases, the VIE drops slower in the ammonia clusters relative to DME. For example, in the cluster with four solvent molecules, the respective VIEs are 2.80 eV and 2.69 eV. The VIEs for the higher-lying states follow the same trend as for the lowest state.

The dependence of the IE on the cluster size is shown in Fig. 4.2. As one can see, VIEs in ammonia clusters decrease monotonically for small cluster sizes, up to $n=4$, for all four states; for larger n , the changes in VIE in ammonia clusters level off and slightly oscillate with increasing n . In DME clusters VIE is monotonically decreasing with the cluster size increase for clusters with up to 6 solvent molecules, and then levels off, too. Thus, for both solvents, the monotonic decrease is observed until the first solvation shell is formed. For the clusters with more solvent molecules, the emerging

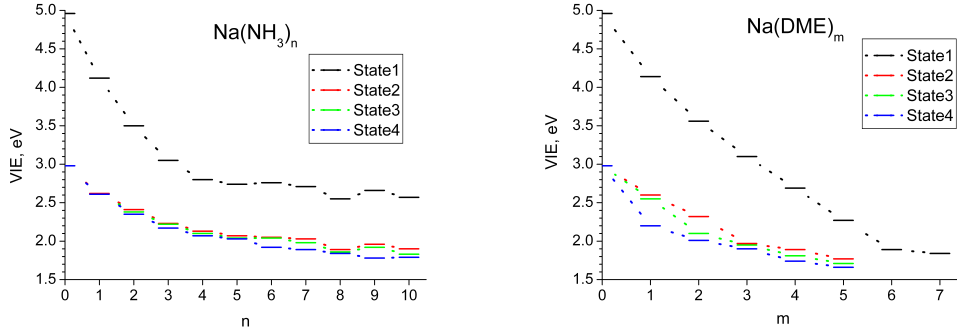


Figure 4.2: Dependence of vertical ionization energies on cluster size for the four lowest electronic states of bare sodium, $\text{Na}(\text{NH}_3)_n$, $n=1\text{-}10$, and $\text{Na}(\text{DME})_m$, $m=1\text{-}5$; EOM-EA-CCSD/aug-cc-pVDZ. The results for $\text{Na}(\text{DME})_{6,7}$ were computed with a smaller basis and reduced orbital space (see text).

shell structure starts to play a role. The shell structure has a more prominent effect on the PAD: for example, β for certain clusters shows magic numbers. That is, the values of β at certain cluster sizes lie far outside the overall trend¹⁹. In the previous work¹⁹, these magic numbers were associated with highly symmetric structures¹⁹. The connection between the cluster structure and experimental observables, as well as the origin of magic numbers in PADs, will be discussed in detail below for $\text{Na}(\text{NH}_3)_4$ and $\text{Na}(\text{DME})_6$.

The solvent affects higher-lying states even more: already in the smallest clusters, the $3p$ manifold is no longer degenerate. The splittings are small in terms of energies, however, oscillator strengths are more sensitive, as readily seen from Tables 4.1 and 4.2. The effect is more pronounced for DME clusters, where oscillator strength for one of the p -like excited states is an order of magnitude lower than for the other two, in contrast to three similar values observed in ammonia clusters. This drop in oscillator strength can be rationalized by the spatial separation between the s and p orbitals: for the states with low oscillator strength, $d_{eh} \approx 6$ bohr, which is much larger than d_{eh} for other states.

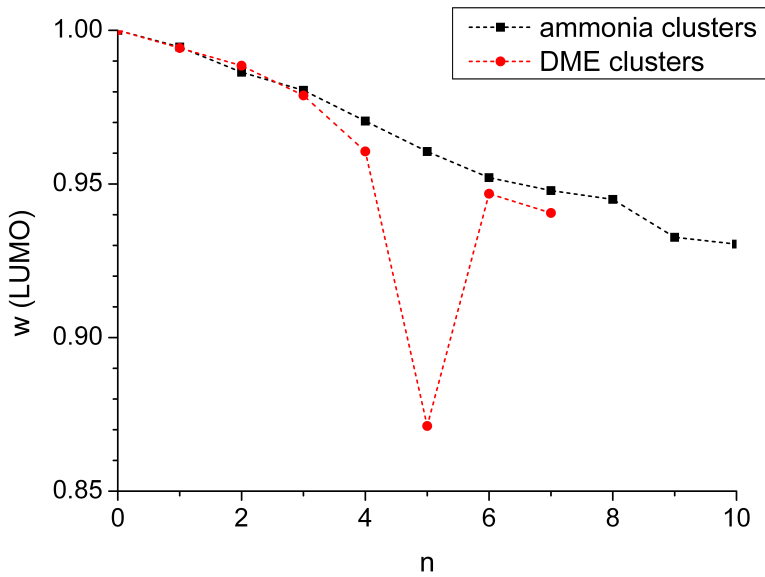


Figure 4.3: The effect of electron correlation on the composition of the the first Dyson orbital in $\text{Na}(\text{NH}_3)_n$, $n=0\text{-}10$, and $\text{Na}(\text{DME})_m$, $m=0\text{-}5$; EOM-EA-CCSD/aug-cc-pVDZ. The values for $\text{Na}(\text{DME})_{6,7}$ were computed with a smaller basis and reduced orbital space (see text). $w(\text{LUMO})$ is the weight of the Hartree-Fock LUMO in the normalized EOM-EA-CCSD Dyson orbital.

To illustrate the effect of electron correlation, it is instructive to quantify the differences between the Hartree-Fock and correlated Dyson orbitals. This can be done by considering the weight of the dominant Hartree-Fock molecular orbital in the EOM-EA-CCSD Dyson orbitals, i.e., the deviations from one quantify the deviation from the Koopmans' theorem (as applied to a positively charged core). Fig. 4.3 shows these values for the lowest electronic state. As one can see, in small clusters, the weight of the Hartree-Fock LUMO in the EOM-EA-CCSD Dyson orbital is very close to one, and then it gradually decreases with the cluster size. The effect of correlation appear to be more pronounced for DME clusters. We note that for DME clusters, even the order of the $3p$ -like states does not follow the Koopmans' theorem predictions.

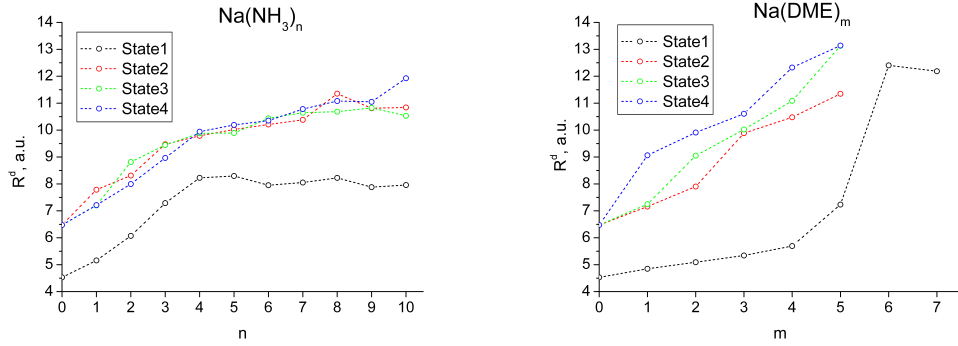


Figure 4.4: Dependence of sizes of Dyson orbitals, \bar{R}^d , on cluster size for the four lowest electronic states of $\text{Na}(\text{NH}_3)_n$, $n=0\text{-}10$, and $\text{Na}(\text{DME})_m$, $m=0\text{-}5$; EOM-EA-CCSD/aug-cc-pVDZ. The results for $\text{Na}(\text{DME})_{6,7}$ were computed with a smaller basis and reduced orbital space (see text).

Fig. 4.4 shows the dependence of the Dyson orbital size, \bar{R}^d , on the number of solvent molecules (a similar plot for the state size, ΔR^Ψ , is shown in Fig. 4.21). We observe a nearly monotonic increase of \bar{R}^d with the cluster size in both ammonia and DME, which correlates nicely with the decreasing IEs: lower IEs correspond to a weaker bound and, therefore, more diffuse electron. This general trend is also seen in ΔR^Ψ . ΔR^Ψ , however, depends on both the EOM-EA state and the reference CCSD state, while Dyson orbitals depend only on the unpaired electron state; therefore, \bar{R}^d provides a more direct measure of the diffuseness of the solvated electron.

As one can see from Fig. 4.4, the size of the unpaired electron in the *s*-like state increases from 4.5 bohr in bare Na to about 7.5 bohr in $\text{Na}(\text{NH}_3)_4$, and then remains nearly constant, consistently with the sharp initial drop in VIE, which levels off after $n=4$. We note small fluctuations at $n=8$ in both VIE and \bar{R}^d . The behavior of *p*-like states is similar, but their respective sizes are larger. As one can see from Table 4.1, *p*-states show clear asymmetry, in contrast to *s*-states. In the DME clusters (Fig. 4.4 and Table 4.2), the initial increase in \bar{R}^d is less steep. For example, for $n=4$, \bar{R}^d for ammonia and DME are about 8.2 and 5.7 bohr, respectively. In contrast to ammonia

clusters, the size continues to increase for $n=5$ and $n=6$, until the first solvation shell is completed. We note that the size of the electron (\bar{R}^d) is particularly large in $\text{Na}(\text{DME})_6$ and $\text{Na}(\text{DME})_7$ in which the first solvation shell is completed. In the smaller DME clusters (with an incomplete solvent shell), the size of the electron is smaller than in the ammonia clusters with the same number of solvent molecules, which can be explained by larger electron binding energy in DME. The observed spread in the p -orbitals sizes is due to the asymmetry. We note that the average size of a p -state does not always correlate with the respective VIE. For all cluster sizes, the asymmetry of the lowest state is small, confirming that this state retains s -like character.

Let us now consider the spatial separation between the average position of the unpaired electron (which is given by the centroid of the corresponding Dyson orbital) and the $\text{Na}^{\delta+}$ core, see Eq. (4.20). Fig. 4.5 shows d_{eh} for the lowest state. In bare Na, $d_{eh}=0$. In ammonia clusters, d_{eh} increases from 0.7 bohr in the smallest cluster up to 5.1 bohr in $\text{Na}(\text{NH}_3)_9$, then slightly decreases to 4.9 bohr in $\text{Na}(\text{NH}_3)_{10}$. In DME clusters, both μ and d_{eh} increase almost linearly, with the slope close to 1, up to $n=5$. In $\text{Na}(\text{DME})_6$, $d_{eh}=0$ due to highly symmetric structure resulting in the Dyson orbital enclosing the entire cluster. For the clusters with the same number of solvent molecules, the offset between the negative charge and $\text{Na}^{\delta+}$ is larger for DME clusters than for ammonia, probably because of the differences in the size of the solvent molecules, with the exception of $\text{Na}(\text{DME})_6$. For example, for $n=5$, d_{eh} is 2.7 bohr and 4.9 bohr in ammonia and DME, respectively. For both types of clusters, d_{eh} increases with the number of solvent molecules. (According to Fig. 4.16, this means that the quality of the plane-wave description of the outgoing electron improves for larger clusters.) For $\text{Na}(\text{DME})_6$, $d_{eh}=0$ because of its highly symmetric structure. We note that d_{eh} values are

rather different for the *s* and *p* states (see Tables 4.1 and 4.2), which reflects a different distribution of electron density.

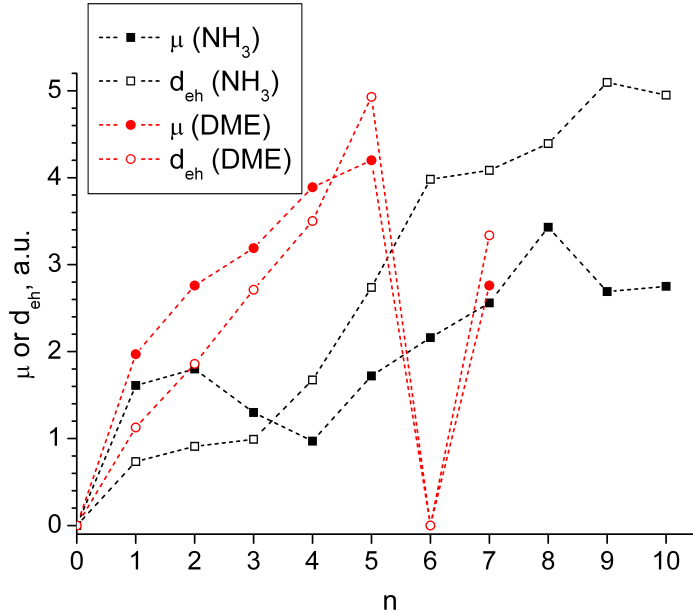


Figure 4.5: Effect of the solvent on dipole moments and the distance between Na and the centroid of Dyson orbitals, d_{eh} , for the lowest electronic state of $\text{Na}(\text{NH}_3)_{0-10}$ and $\text{Na}(\text{DME})_{0-4}$; EOM-EA-CCSD/aug-cc-pVDZ. The results for $\text{Na}(\text{DME})_{5-7}$ were computed with a smaller basis and reduced orbital space (see text).

The offset between the unpaired electron and the positively charged sodium core is related to the dipole moment. Fig. 4.6 shows d_{eh} versus μ for the ammonia and DME clusters. The ammonia clusters show a weak correlation between these two quantities. In contrast, the DME clusters show a much better correlation between d_{eh} and μ . This different behavior can be attributed to the electronic contributions of the solvent molecules. To quantify these contributions, we computed the dipole moment of the ammonia and DME clusters from which the sodium atom was removed (the positions of all solvent molecules were unchanged) and subtracted the result from total μ ; the resulting difference dipole moments are shown in Fig. 4.7. As one can see, there is

much better correlation between this quantity and d_{eh} , both in the ammonia and DME clusters. This is true for all four electronic states and the slopes are close to one in all cases. Larger effect of solvent in ammonia clusters is due to more polar nature of NH_3 .

Different trends in d_{eh} versus μ reflect fundamental differences between the DME and ammonia solvents. The results shown in Figs. 4.6 and 4.7 illustrate that a simplified picture of the unpaired electron interacting with the offset solvated core holds for DME clusters, but is inappropriate for ammonia clusters, where hydrogen-bond network of polar solvent molecules contributes significantly to the electronic properties of the cluster.

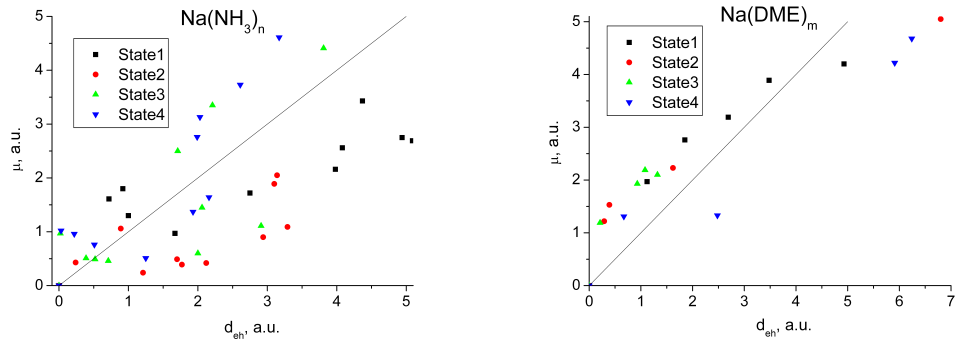


Figure 4.6: Dipole moments and the distance between Na and the centroid of Dyson orbitals, d_{eh} , for the four lowest electronic states of $\text{Na}(\text{NH}_3)_n$, $n=0-10$, and $\text{Na}(\text{DME})_m$, $m=0-5$; EOM-EA-CCSD/aug-cc-pVDZ. A line with slope=1 is plotted to guide the eye.

To quantify the shapes of Dyson orbitals (i.e., how close they are to an ideal s -orbital), we exploit the atomic selection rules for photoelectron states. Since for a pure s -state, the outgoing waves should have pure p character (p_0 for the light polarized along

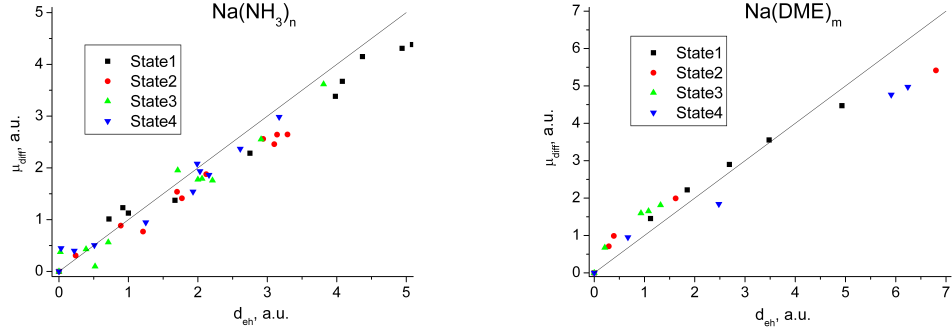


Figure 4.7: Difference dipole moments and distance between Na and the centroid of Dyson orbitals, d_{eh} , for the four lowest electronic states of $\text{Na}(\text{NH}_3)_n$, $n=0\text{-}10$, and $\text{Na}(\text{DME})_m$, $m=0\text{-}5$; EOM-EA-CCSD/aug-cc-pVDZ. A line with slope=1 is plotted to guide the eye.

the z -axis), the deviation of the weight of the p_0 amplitude from one provides a measure of the orbital distortion. Thus, we compute

$$w(p_0) = \frac{|C_{k10}|^2}{\sum_{l,m} |C_{klm}|^2}, \quad (4.25)$$

at k values corresponding to the experimental photon energy 4.66 eV ($k = \sqrt{2m(h\nu - IE)}$) and using z -polarized light. Fig. 4.8 shows that $w(p_0)$ is very close to one for small clusters and decreases with cluster size increase, with the exception of $\text{Na}(\text{NH}_3)_4$ and $\text{Na}(\text{DME})_6$, which both have the completed first solvation shell. There is a noticeable difference between ammonia and DME revealing stronger perturbation of Dyson orbitals by the solvent in DME. This evolution of the orbital character agrees with the trends in VIEs and state/orbital sizes described above.

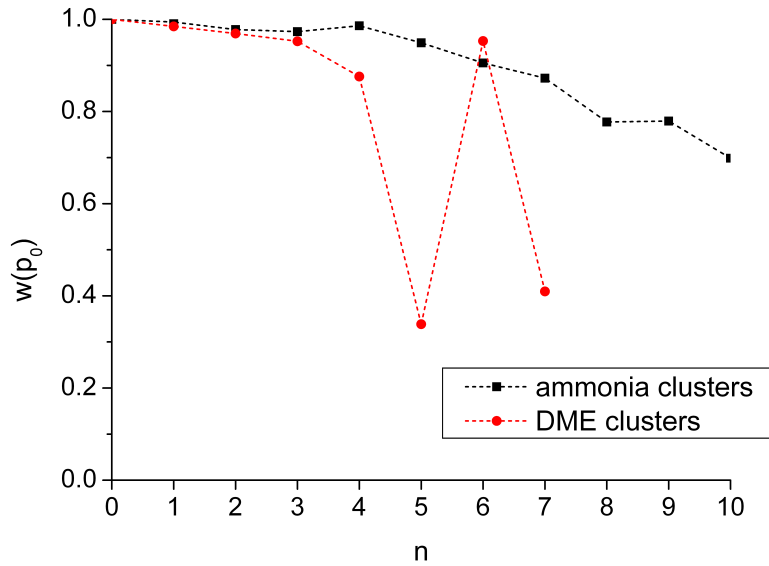


Figure 4.8: The weight of p_0 amplitude in the outgoing waves at $h\nu=4.66$ eV. $\text{Na}(\text{NH}_3)_n$, $n=0\text{-}10$, and $\text{Na}(\text{DME})_m$, $m=0\text{-}5$; EOM-EA-CCSD/aug-cc-pVDZ. The results for $\text{Na}(\text{DME})_{6,7}$ were computed with a smaller basis and reduced orbital space (see text).

4.3.2 Effect of structural fluctuations on electronic properties

The structures of the clusters are floppy and feature multiple local minima²⁹. The thermal fluctuations may affect the shape of the Dyson orbital and, consequently, experimental observables. To investigate these effects, we carried out AIMD simulations at $T=333$ K using ωB97X-D/6-31+G(d).

For $\text{Na}(\text{NH}_3)$, we computed a 2.4 ps trajectory from which snapshots were taken each 120 fs. For this small cluster, the structural fluctuations are small and do not lead to significant variations in electronic properties. IEs vary from 4.14 to 4.20 eV, to be compared with 4.12 eV at the equilibrium structure. Apart from the threshold variations, anisotropy parameters converge to $\beta \approx 2$ at the experimental photon energy (4.66 eV). Total cross-section is more sensitive to structural variations, with maximal variation of

0.65 a.u. ($\sim 15\%$) at the experimental energy and nearly constant difference throughout the entire range of photon energies (0.44 a.u. at 4.21 eV). More details are shown in Appendix.

For larger clusters, $\text{Na}(\text{NH}_3)_4$ and $\text{Na}(\text{NH}_3)_6$, we computed 9.6 ps trajectories from which snapshots were taken each 480 fs. $\text{Na}(\text{NH}_3)_4$ has highly symmetric structure, which does not show large dynamic distortions. $\text{Na}(\text{NH}_3)_6$ is particularly interesting, since it has closely lying conformers that are sampled in the course of thermal motion.

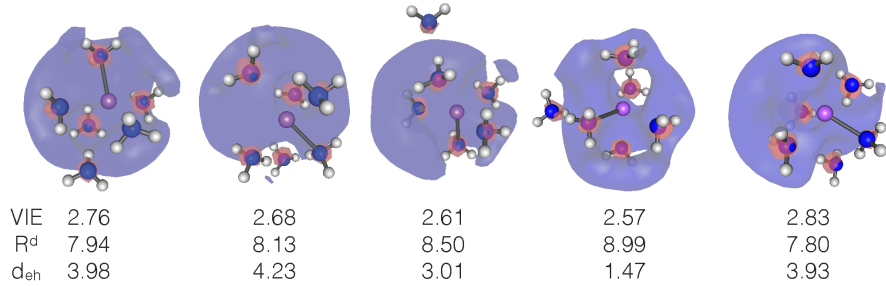


Figure 4.9: Snapshots along the equilibrium trajectory for $\text{Na}(\text{NH}_3)_6$. The respective VIE (eV), \bar{R}^d (bohr), and d_{eh} (bohr) are shown for each snapshot. The first picture corresponds to the minimum-energy structure.

Fig. 4.9 shows the Dyson orbitals and the respective VIE, \bar{R}^d , and d_{eh} for five selected snapshots for $\text{Na}(\text{NH}_3)_6$ (the first picture corresponds to the optimized structure). Additional data are given in Appendix (Table 4.4). The trajectory explores regions corresponding to the two different structures: (i) one with six solvent molecules in one coordination shell (as in snapshots 1, 2, and 5); and (ii) one with five solvent molecules in the first shell and one molecule in the second shell (snapshots 3 and 4). The shape of the Dyson orbital and, consequently, electronic properties show significant fluctuations among the snapshots. VIEs vary from 2.57 eV to 2.83 eV (to be compared with 2.76 eV in the optimized structure). The size of the Dyson orbital varies between 7 and 9 bohr. The hole-electron distance fluctuates between 1.5 to 4.5 bohr. These variations

in the shape of the unpaired electron lead to noticeable variations in the experimental observables: β (computed at 4.66 eV) fluctuates between 1.5 and 1.9 (see Fig. 4.26 in Appendix). For $\text{Na}(\text{NH}_3)_4$, in contrast, the thermal fluctuations of β are smaller, due to its more rigid structure (β at 4.66 eV fluctuates between 1.95-1.98, as shown in Appendix in Fig. 4.24).

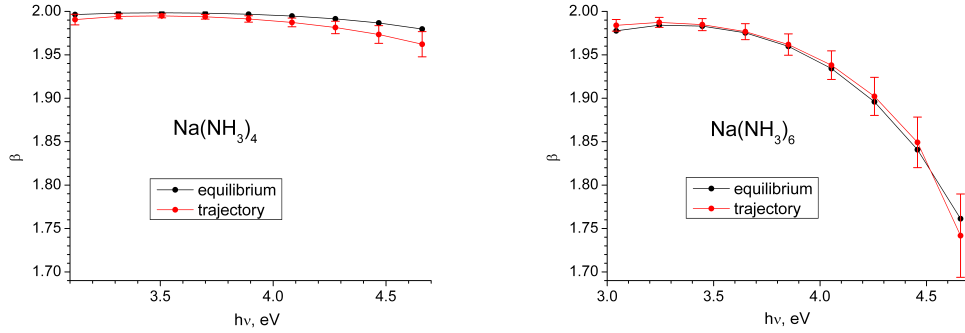


Figure 4.10: Dependence of anisotropy parameter on photon energy at the minimal-energy structure compared with equilibrium trajectory average (computed by averaging β over 21 snapshots) for $\text{Na}(\text{NH}_3)_4$, left, and $\text{Na}(\text{NH}_3)_6$, right.

Fig. 4.10 compares β computed for the minimum-energy structures against the values averaged over 21 snapshots for the two clusters. The difference between the two clusters is two-fold. First, thermal fluctuations of β are larger for $\text{Na}(\text{NH}_3)_6$ at all computed photon energies. Second, in $\text{Na}(\text{NH}_3)_6$ the thermal motions lead to random fluctuations in β around the value corresponding to the minimum energy structure, whereas in $\text{Na}(\text{NH}_3)_4$ thermal motions almost always result in the decrease of anisotropy. Consequently, for $\text{Na}(\text{NH}_3)_6$ the averaged value of β at 4.66 eV is 1.74 ± 0.05 is almost the same as β for the minimum-energy structure ($\beta=1.76$), whereas for $\text{Na}(\text{NH}_3)_4$ the minimum-energy structure value, 1.98, is an upper bound of trajectory-averaged 1.96 ± 0.02 . As discussed below, this difference contributes to the appearance of magic numbers in anisotropies.

Thermal fluctuations of β and σ for Na(DME)₄ (see Appendix) are similar in magnitude to those in Na(NH₃)₆, but their origin is different. In the ammonia clusters, the fluctuations mostly arise from the rearrangement of the solvent molecules around the Na core, whereas in DME they are dominated by the internal solvent degrees of freedom: i.e., the 9.6 ps trajectory for DME does not sample different conformers, but shows rotations of the CH₃ groups and CO vibrations. The effect of intra-molecular degrees of freedom comes into play already in the Na(DME) cluster; the snapshots from the respective equilibrium trajectory show small but noticeable variations in anisotropy parameters and total cross-sections at 4.66 eV (see Appendix, Fig. 4.23). The magnitude of these fluctuations is larger than in Na(NH₃).

For Na(DME)₆, selected snapshots for which are shown in Fig. 4.11, we also observe large fluctuations in the shape of the Dyson orbital and in its electronic properties, and the fluctuations are coming mostly from the solvent's internal degrees of freedom. Since the optimized structure is highly symmetric, small distortions have dramatic effect on the electronic wave function, e.g., the Dyson orbital becomes localized at lower-symmetry structures and the clusters develop large dipole moment, up to 14.5 Debay (to be compared with 0 Debay at the equilibrium structure). Consequently, the computed β for equilibrium structure is considerably different from β 's computed along the equilibrium trajectory. At the experimental energy, $\beta=1.83$ for equilibrium structure (EOM-EA-CCSD value of 1.88), whereas averaged value is 1.68 ± 0.06 . For comparison, consider Na(DME)₄ in which equilibrium β is 1.68 and thermally averaged β is 1.67 ± 0.07 . Detailed comparison is shown in Appendix.

These observations suggest that thermal fluctuations in larger clusters may cause significant fluctuations in properties, including the decrease in the average anisotropy relative to the values computed for the minimal-energy structures. Also, we expect

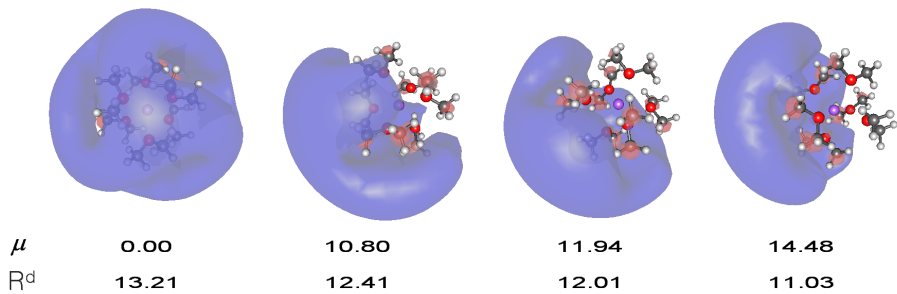


Figure 4.11: Snapshots along the equilibrium trajectory for $\text{Na}(\text{DME})_6$. The respective dipole moments (Debay) and \bar{R}^d (bohr) are shown for each snapshot. The first picture corresponds to the minimum-energy structure. All orbitals are shown with the same isovalue of 0.008.

larger variations for DME, because of the internal degrees of freedom. Highly symmetric structures are special: in $\text{Na}(\text{NH}_3)_4$ and $\text{Na}(\text{DME})_6$, the thermal motions result in lower β , whereas in clusters of other sizes, the equilibrium structure values are close to average values.

4.3.3 The effect of correlation on the shape of Dyson orbitals

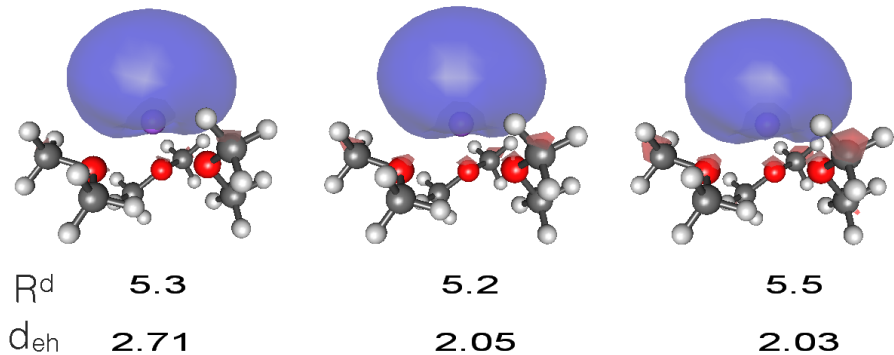


Figure 4.12: Dyson orbitals for $\text{Na}(\text{DME})_3$ computed with EOM-EA-CCSD (left), $\omega\text{B97X-D}/\text{Koopmans'}$ (middle), and B3LYP/Koopmans' (right). Orbitals are shown with the same isovalue of 0.025. The orbitals are computed using the aug-cc-pVDZ and 6-31+G(d) basis sets for EOM and DFTs, respectively.

Using $\text{Na}(\text{DME})_3$ as an example, Fig. 4.12 compares Dyson orbitals computed using EOM-EA-CCSD with the DFT orbitals (Kohn-Sham SOMOs of the neutral radicals) using the $\omega\text{B97X-D}$ and B3LYP functionals^{41–43}. The orbitals look very similar. The variations in the diffuseness of the orbitals (as quantified by \bar{R}^d) are small (0.1–0.2 bohr difference between EOM-EA and DFT), but the offset between the centroid of the orbital and $\text{Na}^{\delta+}$ varies quite noticeably, e.g., the difference between EOM-EA and B3LYP value is 0.7 bohr. DFT SOMOs are closer to the sodium core than the EOM Dyson orbitals, which can be explained by the self-interaction error affecting the description of the exchange interactions between the unpaired electron and solvent’s electrons. The trend in d_{eh} clearly correlates with the amount of the exact exchange: d_{eh} is the smallest for B3LYP. To analyze this effect further, we included the CAM-B3LYP functional (19% of short-range and 65% of long-range exact exchange contributions)⁴⁴, as an intermediate between B3LYP (19% globally)⁴³ and $\omega\text{B97X-D}$ (22% at short range and 100% at long range)^{41,42}. We also consider Hartree-Fock orbitals, which correspond to 100% exact exchange everywhere. In these calculations, we used unrestricted Hartree-Fock or DFT; $\langle S^2 \rangle$ values did not exceed 0.7504. The results are collected in Table 4.3 and visualized in Fig. 4.13.

Table 4.3: VIEs ($-\varepsilon$ as Koopmans’ theorem), dipole moments, and properties of the SOMO orbitals for the $\text{Na}(\text{NH}_3)_n$ and $\text{Na}(\text{DME})_m$ clusters ($n=1\text{--}10$, $m=1\text{--}7$) computed at the UHF/6-31+G(d) and DFT/6-31+G(d) levels of theory. Ionization energies are given in eV and other quantities in a.u.

System	Method	$-\varepsilon$	μ	\bar{R}^d			d_{eh}
				X	Y	Z	
$\text{Na}(\text{NH}_3)$	HF	4.05	2.04	2.7	3.0	3.0	1.12
	$\omega\text{B97X-D}$	4.05	1.97	2.8	2.9	2.9	1.03
	CAM-B3LYP	3.65	1.53	2.9	2.9	2.9	0.57

	B3LYP	2.83	1.31	3.0	2.9	2.9	0.36
Na(NH ₃) ₂	HF	3.35	2.66	3.3	3.1	3.5	1.76
	ωB97X-D	3.43	2.45	3.3	3.2	3.4	1.52
	CAM-B3LYP	3.07	1.67	3.4	3.3	3.4	0.70
	B3LYP	2.42	1.29	3.5	3.5	3.4	0.31
Na(NH ₃) ₃	HF	2.75	2.57	4.3	4.3	4.1	2.33
	ωB97X-D	2.91	2.32	4.1	4.1	3.9	2.06
	CAM-B3LYP	2.67	1.19	4.1	4.1	4.0	0.86
	B3LYP	2.15	0.81	4.2	4.1	4.0	0.46
Na(NH ₃) ₄	HF	2.39	1.48	5.4	5.4	5.2	2.23
	ωB97X-D	2.61	1.81	4.9	4.9	4.7	2.60
	CAM-B3LYP	2.45	0.92	4.7	4.7	4.5	1.67
	B3LYP	2.04	0.64	4.7	4.6	4.4	1.36
Na(NH ₃) ₅	HF	2.31	2.75	5.5	4.9	5.5	3.86
	ωB97X-D	2.56	2.78	4.9	4.3	4.9	3.95
	CAM-B3LYP	2.39	1.64	4.8	4.5	4.7	2.74
	B3LYP	1.99	1.10	4.7	4.6	4.6	2.13
Na(NH ₃) ₆	HF	2.34	3.11	5.2	5.4	4.7	4.97
	ωB97X-D	2.61	2.67	4.7	4.8	4.1	4.62
	CAM-B3LYP	2.42	1.85	4.7	4.7	4.2	3.80
	B3LYP	1.99	1.29	4.7	4.7	4.2	3.21
Na(NH ₃) ₇	HF	2.29	3.54	4.5	5.5	5.6	5.07
	ωB97X-D	2.56	3.10	4.0	4.8	4.9	4.73
	CAM-B3LYP	2.37	2.22	4.2	4.7	4.8	3.86
	B3LYP	1.93	1.55	4.4	4.6	4.8	3.15
Na(NH ₃) ₈	HF	2.15	4.48	4.8	5.4	6.0	5.12
	ωB97X-D	2.39	4.02	4.4	4.7	5.3	4.91
	CAM-B3LYP	2.18	3.01	4.7	4.7	5.1	4.09
	B3LYP	1.80	2.02	5.1	4.7	5.0	3.32
Na(NH ₃) ₉	HF	2.23	3.63	5.3	5.5	4.4	6.09
	ωB97X-D	2.56	2.87	4.7	4.8	4.0	5.42
	CAM-B3LYP	2.31	2.17	4.7	4.7	4.1	4.71
	B3LYP	1.90	1.54	4.8	4.7	4.3	3.98

Na(NH ₃) ₁₀	HF	2.18	3.80	5.0	5.0	5.2	6.03
	ω B97X-D	2.45	3.07	4.4	4.4	4.6	5.40
	CAM-B3LYP	2.23	2.27	4.6	4.6	4.7	4.60
	B3LYP	1.82	1.50	4.8	4.8	4.8	3.73
Na(DME)	HF	4.08	2.32	2.9	2.9	2.5	1.41
	ω B97X-D	4.08	2.18	2.8	2.8	2.5	1.30
	CAM-B3LYP	3.67	1.83	2.7	2.8	2.5	0.95
	B3LYP	2.78	1.70	2.8	2.8	2.6	0.84
Na(DME) ₂	HF	3.48	3.27	2.9	2.5	3.1	2.27
	ω B97X-D	3.51	2.99	2.9	2.6	3.1	2.03
	CAM-B3LYP	3.07	2.56	2.8	2.6	3.0	1.60
	B3LYP	2.29	2.34	2.9	2.7	3.1	1.39
Na(DME) ₃	HF	2.99	3.82	3.2	3.2	2.6	3.26
	ω B97X-D	3.05	3.40	3.1	3.1	2.7	2.85
	CAM-B3LYP	2.64	2.92	3.2	3.1	2.7	2.38
	B3LYP	1.88	2.59	3.3	3.3	2.9	2.03
Na(DME) ₄	HF	2.53	4.72	3.2	3.6	2.8	4.22
	ω B97X-D	2.67	4.14	3.2	3.5	2.9	3.69
	CAM-B3LYP	2.23	3.62	3.2	3.5	2.9	3.16
	B3LYP	1.58	3.04	3.6	3.8	3.4	2.52
Na(DME) ₅	HF	2.04	5.65	4.7	4.8	3.6	6.37
	ω B97X-D	2.26	4.64	3.9	4.1	3.4	5.43
	CAM-B3LYP	1.88	3.86	4.3	4.3	3.8	4.59
	B3LYP	1.44	2.42	4.8	4.8	4.9	2.91
Na(DME) ₆	HF	1.55	0.00	7.8	7.8	7.8	0.00
	ω B97X-D	1.66	0.00	7.6	7.6	7.6	0.00
	CAM-B3LYP	1.63	0.00	7.0	7.0	7.0	0.00
	B3LYP	1.44	0.00	6.7	6.7	6.7	0.00
Na(DME) ₇	HF	1.52	5.71	7.1	7.7	6.1	6.57
	ω B97X-D	1.66	5.63	7.0	7.5	5.9	6.53
	CAM-B3LYP	1.58	2.48	6.8	7.2	6.8	3.05
	B3LYP	1.39	1.18	6.7	6.9	6.7	1.60

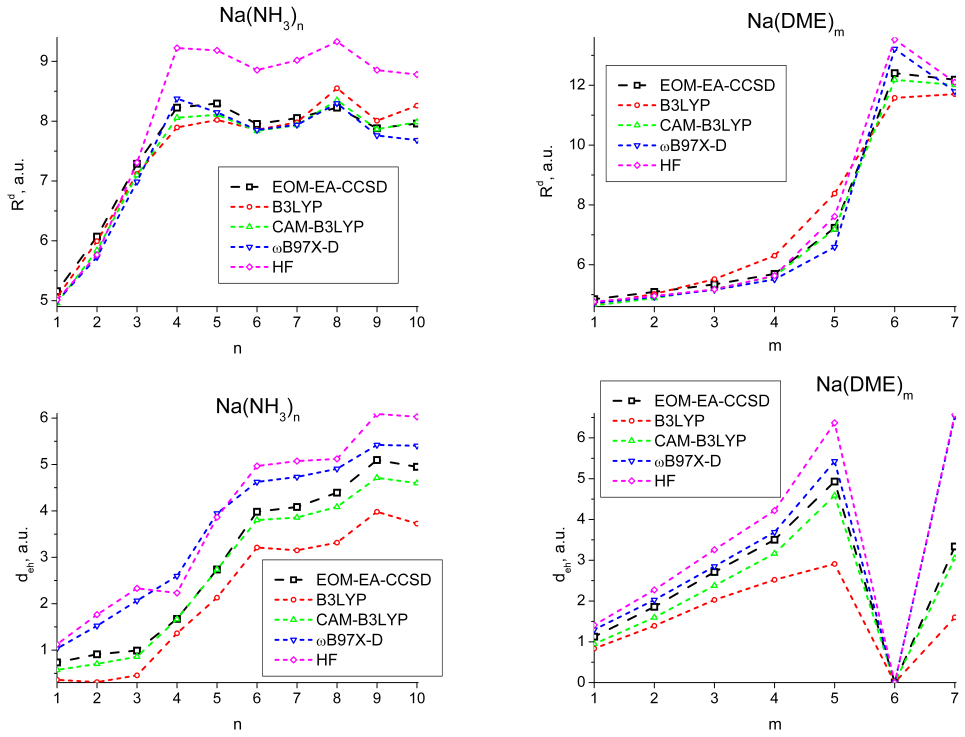


Figure 4.13: Sizes of Dyson orbitals and the distance between their centroids and $\text{Na}^{\delta+}$ for $\text{Na}(\text{NH}_3)_n$, $n=1-10$, and $\text{Na}(\text{DME})_m$, $m=1-7$; at the EOM-EA-CCSD/aug-cc-pVQZ (smaller basis and reduced orbital space for $m=6-7$, see text), $\omega\text{B97X-D}/6-31+\text{G(d)}$, CAM-B3LYP/6-31+G(d), B3LYP/6-31+G(d), and HF/6-31+G(d) levels of theory.

As Fig. 4.13 shows, the spread in the sizes of the orbitals is rather small (0.2-0.4 bohr) for the cluster sizes studied, except for the UHF results for ammonia clusters with more than four solvent molecules (these show 1 bohr deviation). The $\omega\text{B97X-D}$ and CAM-B3LYP curves are nearly parallel to the EOM curve, especially for $\text{Na}(\text{NH}_3)_n$, whereas the errors of B3LYP and HF show more variations with the cluster size. CAM-B3LYP provides nearly perfect agreement with EOM results in DME clusters. The variations in d_{eh} are much larger. We see that HF overestimates exchange repulsion, giving rise to the largest offset of the Dyson orbital. $\omega\text{B97X-D}$ values are closer to EOM-EA.

Interestingly, CAM-B3LYP gives d_{eh} values that are closest to EOM-EA. The separation between the unpaired electron and the sodium core arises due to repulsive exchange interactions between the unpaired electron and solvent's electron density. This interaction is correctly described by the Hartree-Fock exchange, but self-interaction error in DFT leads to the underestimated exchange repulsion. These results illustrate that both exchange and correlation are important for correctly describing the solvated electron. For DME, the differences between different methods are smaller for both \bar{R}^d and d_{eh} .

The effect of the orbital shape and IE values on β and σ is illustrated in Figs. 4.28-4.37 for clusters of various sizes. Let us first consider Na(NH₃) and Na(DME) (Fig. 4.28). The main differences between the methods are due to different threshold energies. Away from the threshold, e.g., at the experimental photon energy, all methods yield similar values of β . However, for total cross-sections even at 4.66 eV the B3LYP values still differ from EOM, ω B97X-D and Hartree-Fock perform well, while CAM-B3LYP results fall in between. Similar trends are observed for other small clusters. For larger clusters, we observe more significant discrepancies between β (and σ) values computed with different methods. The largest errors are observed for HF and B3LYP. CAM-B3LYP and ω B97X-D consistently show the smallest errors in β in the entire photon energy range. On average, CAM-B3LYP is often better for ammonia clusters, whereas ω B97X-D is better for DME. One exception is Na(DME)₅, where ω B97X-D shows relatively large errors. For σ , ω B97X-D delivers the best performance across the entire photon energy range.

To facilitate further comparison, we plot β and σ at experimental energy of 4.66 eV for different cluster sizes, which is shown in Fig. 4.14. Clearly, there is no perfect DFT functional for the task. However, qualitatively, all methods reproduce the EOM-EA-CCSD trends. For ammonia clusters, in terms of β , all methods perform similarly up

to $n=3$; B3LYP and CAM-B3LYP stay close to the EOM reference up to $n=5$. CAM-B3LYP continues to deliver the best performance for medium-size clusters, but then its performance deteriorates for larger clusters, for which ω B97X-D gives better results. Overall, however, the difference between DFT and reference EOM-EA-CCSD increases for larger clusters. For σ , ω B97X-D performs the best. Interestingly, the difference against EOM decreases for all DFT methods with the cluster size increase.

In DME clusters, the best performance for β is provided by CAM-B3LYP. All methods (except B3LYP) perform well for small clusters. The errors are large for $\text{Na}(\text{DME})_5$ for all methods, except CAM-B3LYP. We note that B3LYP underestimates β and HF overestimates it, which suggests that good performance of CAM-B3LYP is due to error cancellation. As pointed out above, this cluster shows relatively large deviations from Koopmans' theorem: as one can see from Fig. 4.3, the EOM-EA-CCSD Dyson orbitals are about 85% of Koopmans' character, which is a drop relative to commonly observed 95%. For largest clusters, all methods perform well. In terms of σ , ω B97X-D and HF show the best performance with an exception for $m=7$, where the best result is delivered by B3LYP and CAM-B3LYP. In general, all computed properties obtained at ω B97X-D and HF levels of theory appear to be very close in DME clusters of all sizes.

To further compare the shapes of the Kohn-Sham SOMOs and the EOM-CC Dyson orbitals, we again consider $w(p_0)$ at 4.66 eV. The computed values are shown in Fig. 4.15. The weights agree for small n , but start to differ for larger clusters. In the case of ammonia, CAM-B3LYP and ω B97X-D provide the best agreement, but overall the disagreement with EOM-EA is quite considerable. In the case of DME, however, CAM-B3LYP and HF are in a perfect agreement with the EOM reference, except for $n=7$, for which HF deviates from EOM-EA-CCSD and matches ω B97X-D.

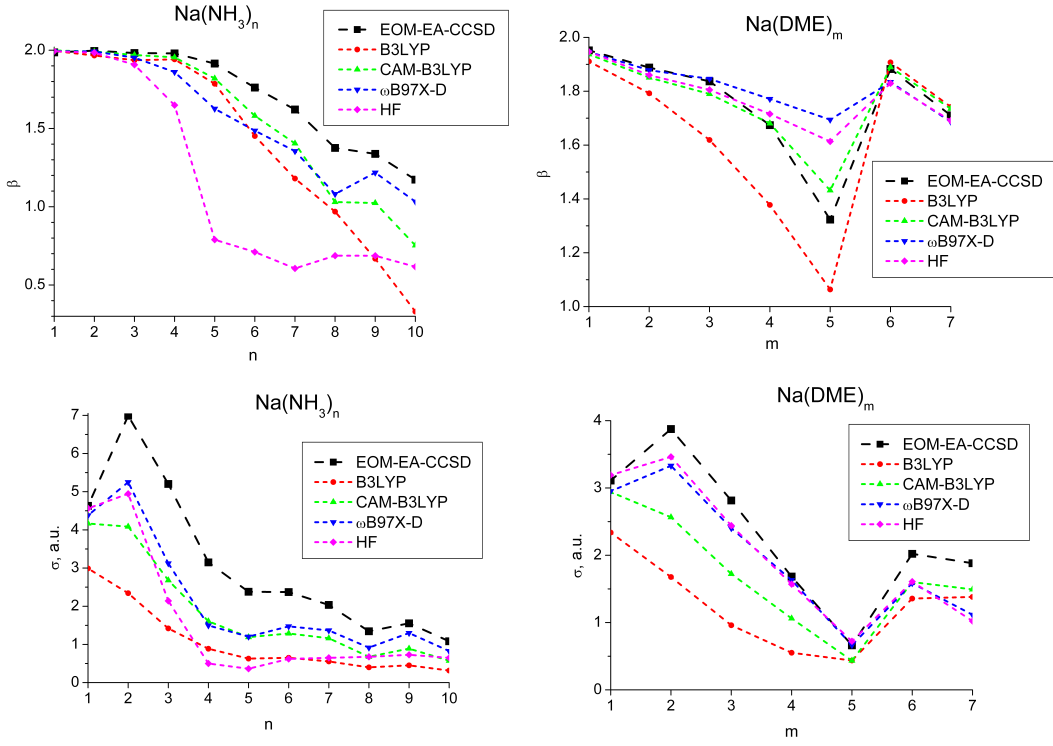


Figure 4.14: Anisotropy parameters (upper panel) and total cross-sections (lower panel) for different cluster sizes at energy of 4.66 eV computed using the EOM-EA-CCSD Dyson orbitals and Koopmans' theorem (DFT or HF SOMO).

Interestingly, in the case of ammonia, DFT and HF produce a less *s*-like orbitals (as compared to EOM-EA-CCSD), whereas in the case of $\text{Na}(\text{DME})_m$, the deviations are random. Overall, the performance of the methods in terms of orbital character follows that for anisotropy parameters.

To quantify the effect of the basis on the ω B97X-D orbitals (and, consequently, β and σ), we also considered the aug-cc-pVDZ basis set. The results for medium-size system, $\text{Na}(\text{NH}_3)_5$, are shown in Fig. 4.20 (the reference value is EOM-EA-CCSD/aug-cc-pVDZ). As one can see, at the DFT level aug-cc-pVDZ delivers only slightly better performance than 6-31+G(d). The effect of increasing the basis beyond aug-cc-pVDZ is negligible.

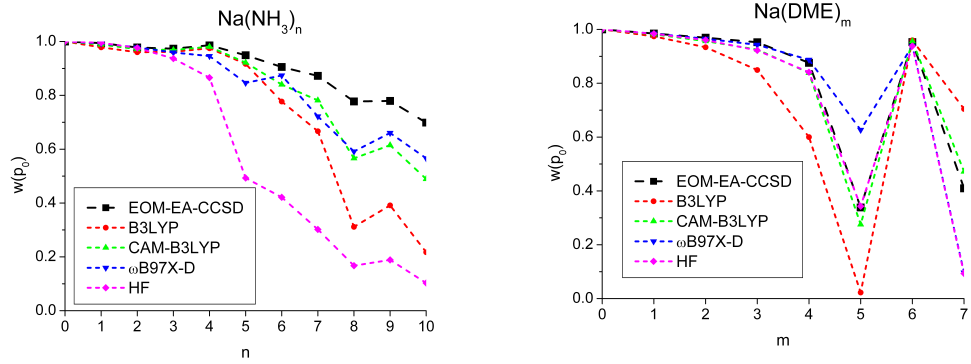


Figure 4.15: The weight of the p_0 amplitude in the outgoing waves at $h\nu=4.66$ eV. $\text{Na}(\text{NH}_3)_n$, $n=0\text{-}10$, and $\text{Na}(\text{DME})_m$, $m=0\text{-}7$; EOM-EA-CCSD/aug-cc-pVDZ (smaller basis and reduced orbital space for $m=6\text{-}7$, see text) versus DFT/6-31+G(d) and HF/6-31+G(d).

The increasing differences in the shapes of EOM-EA-CCSD Dyson orbitals and Kohn-Sham SOMOs with the cluster-size increase (as well as non-systematic errors of different DFT functionals in computed experimental observables) signal caution for applying DFT for larger clusters. Indeed, although for smaller clusters all trends are qualitatively similar, it is unclear how large the deviation between DFT and EOM-EA-CCSD might become for large clusters.

4.3.4 Comparison with experiment

The trends in computed VIEs, such as changes with the cluster size increase and difference between ammonia and DME, are in agreement with the experimental observations^{18–20}. The calculations using lowest-energy optimized structures show that the lowest electronic state has *s*-like character resulting in large β values. The *s*-like character gradually decreases in larger clusters, with cluster size increase, with DME clusters being affected earlier (Fig. 4.15), with an exception of a highly symmetric cluster, $\text{Na}(\text{DME})_6$.

For the cluster sizes studied, we observe that β -values (computed at the experimental photon energy using EOM-EA-CCSD) vary within 1.2-2.0 for ammonia ($n=1-10$) clusters and 1.3-2.0 for DME ($m=1-7$), which is shown in Fig. 4.14. Not surprisingly, the agreement with experiment is qualitative at best. The lack of quantitative agreement can be attributed partly to the thermal fluctuations (which are not captured by the calculations using a single structure) and partly to the experimental uncertainties, such as the spread of cluster sizes.

Signorell and coworkers have reported that PADs of small sodium-doped clusters exhibit magic numbers behavior¹⁹. Specifically, they observed higher β values for $\text{Na}(\text{NH}_3)_4$ and $\text{Na}(\text{DME})_6$, which they attributed to highly symmetric equilibrium structures of these complexes. The calculation with EOM-EA-CCSD shows the spike in β for $\text{Na}(\text{DME})_6$ (see Fig. 4.14). For $\text{Na}(\text{NH}_3)_4$, we see no spike, only a sharp drop for $\text{Na}(\text{NH}_3)_5$. Similar results are obtained using DFT (including the same functional and basis set as in Ref.¹⁹). Yet, the experimental β clearly show magic number at $n=4$ for ammonia. On the basis of our analysis of AIMD trajectories, we attribute this discrepancy to the dynamic fluctuations (see section 4.3.2). The effect of thermal fluctuations is different for $\text{Na}(\text{NH}_3)_4$ and $\text{Na}(\text{NH}_3)_6$ (Fig. 4.10, S9 and S10). We observe relatively small spread in values for $\text{Na}(\text{NH}_3)_4$, which appears to be more rigid, relative to $\text{Na}(\text{NH}_3)_6$ (Fig. 4.10): i.e., for $\text{Na}(\text{NH}_3)_4$ trajectory averaged $\beta=1.96\pm0.02$, with equilibrium β equal to 1.98, while for $\text{Na}(\text{NH}_3)_6$ trajectory averaged $\beta=1.74\pm0.05$, compared to equilibrium value of 1.76. A similar dynamical lowering might occur in $\text{Na}(\text{NH}_3)_3$, which will then lead to the spike in β for $\text{Na}(\text{NH}_3)_4$. For $\text{Na}(\text{DME})_6$ the spread of β 's at experimental energy is considerable along the trajectory, leading to

reduced value of β , which can wash out the appearance of magic numbers. Yet, equilibrium values of anisotropy parameter are significantly smaller for $m=5$ and 7, relative to $m=6$, and they are also expected to have considerable effect of thermal fluctuations.

Thus, in contrast to DME, the appearance of magic numbers in ammonia clusters is dynamic in nature: highly symmetric structures (such as $\text{Na}(\text{NH}_3)_4$) are more rigid and show less structural fluctuations relative to other clusters.

4.4 Conclusions

We presented detailed calculations of sodium-doped ammonia and DME clusters. Using the EOM-EA-CCSD method, we computed ionization energies and Dyson orbitals for the four lowest electronic states for clusters of different size. In all four states, the unpaired electron can be described as the unpaired electron of sodium, perturbed by the solvent and residing on the surface of the cluster. The lowest electronic state has *s*-like character, whereas the three higher states appear as distorted *p*-states. In larger clusters, the *s*-like character of the lowest state gradually decreases. The two solvents are fundamentally different: in DME, the binding energy of the unpaired electron is larger than in ammonia and its shape is less diffuse. The analysis of the electronic properties of the clusters reveals further differences between the two solvents: the electronic structure of the DME clusters can be loosely described as the unpaired electron interacting with a displaced solvated sodium core, whereas in ammonia clusters the hydrogen-bonded network of polar solvent molecules contributes significantly into the overall electronic properties (such as dipole moment) of the cluster.

Focusing on the experimental observables, we analyzed the effect of orbital shape on anisotropy parameters and total cross-sections. Our findings are in agreement with recent experimental work by Signorell and co-workers^{18–20}. In particular, we observe

that the lowest electronic state retains its *s*-like character in both solvents; however, the state becomes more distorted in larger clusters. We also quantified the effect of thermal motions on the shape of Dyson orbitals. The structural fluctuations lead to orbital distortions, which results in deviations between thermally averaged β values and the values computed for lowest-energy structures. Some clusters, such as $\text{Na}(\text{NH}_3)_4$, are more rigid than clusters of other sizes, which leads to smaller fluctuations in β ; this is responsible for observed magic numbers in anisotropies in ammonia¹⁹. Magic number appearance in $\text{Na}(\text{DME})_6$ can be explained by its highly-symmetric equilibrium structure.

We also quantified the effect of electron correlation on the orbital shape and experimental observables. The Kohn-Sham orbitals are very sensitive to the amount of Hartree-Fock exchange. The self-interaction errors in DFT lead to errors in describing repulsive exchange interactions between the unpaired electron and the solvent electron density, which results in smaller offsets between the density of the unpaired electron and $\text{Na}^{\delta+}$. The comparison against EOM-EA-CCSD shows that DFT and HF orbitals are qualitatively correct; however, the errors increase with the cluster size increase. $\omega\text{B97X-D}$ and CAM-B3LYP shows the best performance.

4.5 Appendix A: Calculations of total cross-sections and anisotropy parameters

In the *ezDyson* calculations³⁸, the important parameters are l_{max} , the highest angular momentum in the plane wave basis, and the grid size. We investigated the effect of these parameters on the computed anisotropy parameters and cross-sections for every case. The box of -20 to 20 Å was sufficient for all systems. For all EOM-EA-CCSD Dyson orbitals, $l_{max}=5$ was used, and the contributions from the waves with high l were shown to be negligible. For DFT SOMOs, l_{max} in the largest clusters was increased to 9, due to larger set of contributing outgoing waves, especially at higher photon energies.

Fig. 4.16 shows the dependence of the overlap of $\Psi^{el}(Z)$ and $H^{Coul}\Psi^{el}(Z)$ on the distance between the expansion origin for the free electron wave function and the positive charge assuming an outgoing *p*-wave (from an *s*-like state) in a one-dimensional model potential. By virtue of Eq. (24) from the main manuscript, the optimal value of Z would give the largest overlap of $\Psi^{el}(Z)$ and $H^{Coul}\Psi^{el}(Z)$. The distance d between the centroid of the unpaired electron and $\text{Na}^{\delta+}$ is varied within the range of values from Tables 4.1 and 4.2 from the main manuscript. We considered three different values of electron kinetic energy E_k : 0.5 eV, 1.5 eV, and 2.5 eV. As one can see, for $E_k=0.5$ eV the optimal values of effective charge Z are close to zero (and definitely do not exceed 0.4). The calculations using $E_k=1.5$ and 2.5 eV yield similar results. The deviation of optimal Z from 0 is smaller for larger d and higher E_k , suggesting that the quality of plane-wave description improves for clusters with more solvent molecules. As one can see from Fig. 4.17, even for $n=1$ at the experimental energy of 4.66 eV, computed β 's show little variations whether a plane wave or a Coulomb wave with $Z=0.2-0.4$ is used,

while the variations in the total absolute cross-sections can be larger — up to 50 % of the plane-wave value.

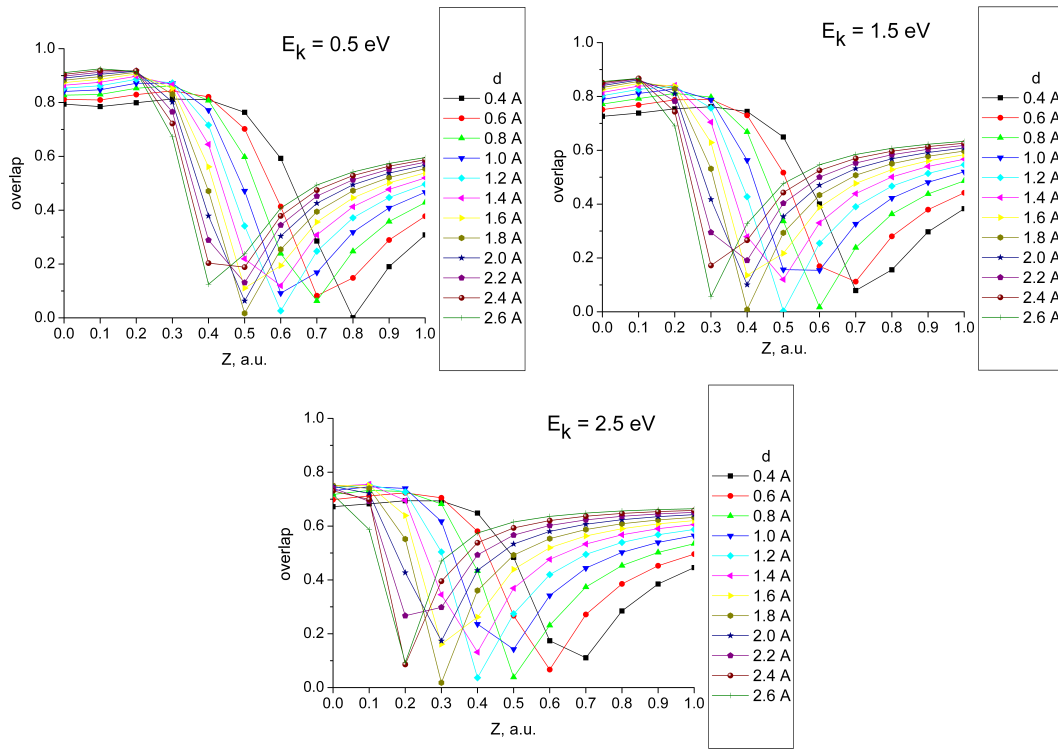


Figure 4.16: Optimizing effective core charge Z for the outgoing p -wave with $E_k=0.5 \text{ eV}, 1.5 \text{ eV}, \text{ and } 2.5 \text{ eV}$.

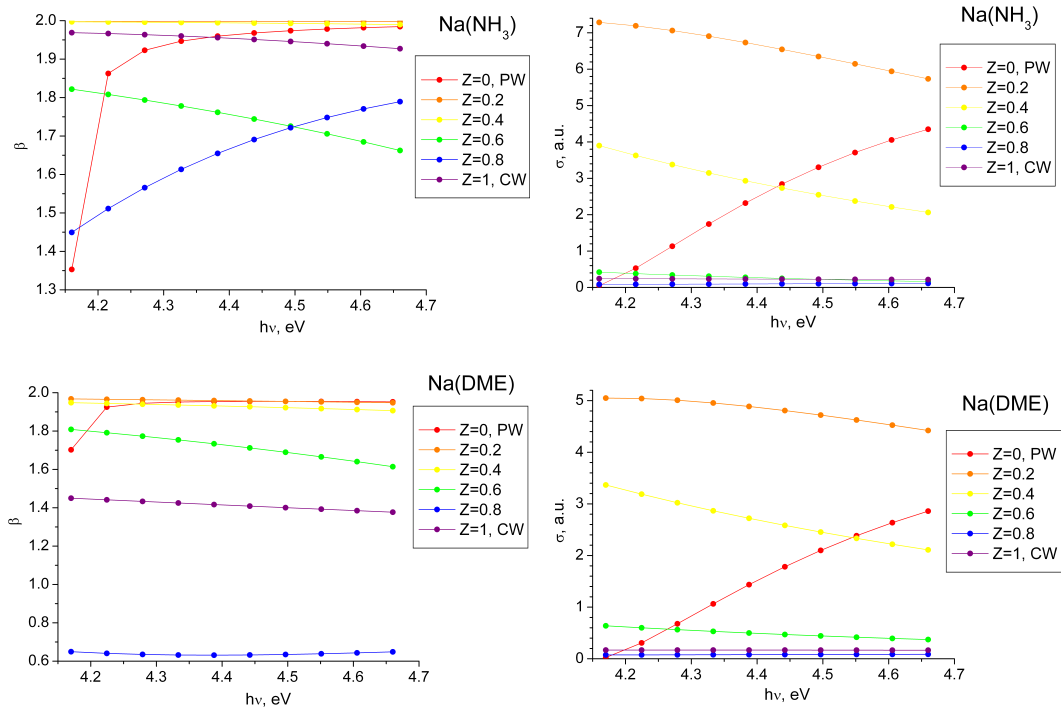


Figure 4.17: Dependence of anisotropy parameters and total cross-sections on photon energy for different values of effective charge Z for $\text{Na}(\text{NH}_3)$ (upper panels) and $\text{Na}(\text{DME})$ (lower panels).

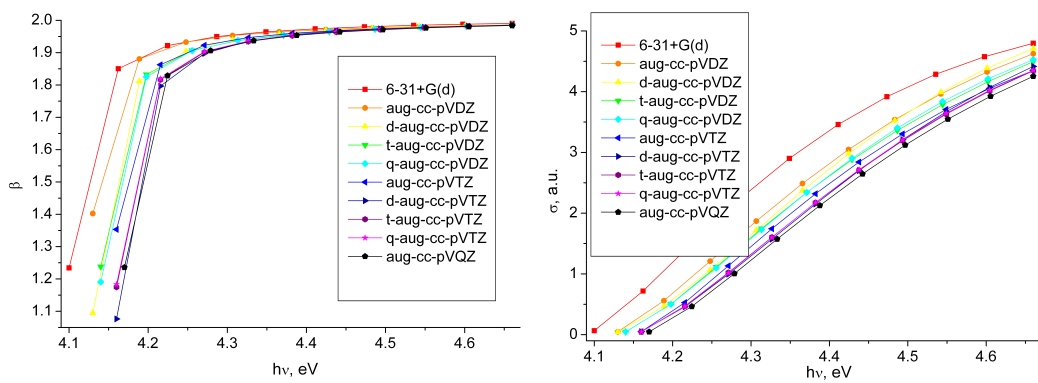


Figure 4.18: Dependence of anisotropy parameters and total cross-sections on photon energy and basis sets for $\text{Na}(\text{NH}_3)$.

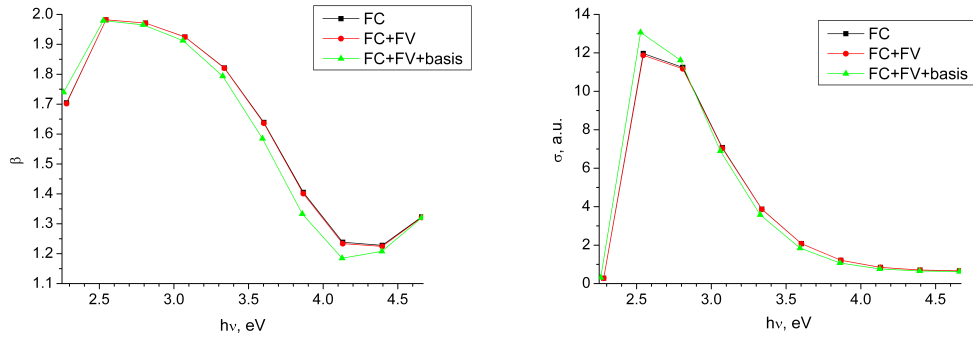


Figure 4.19: The effect of using reduced basis set and virtual orbital space on β and σ for $\text{Na}(\text{DME})_5$. FC denotes the EOM-EA-CCSD/aug-cc-pVDZ calculations with frozen core orbitals. FV denotes calculations with 31 frozen virtual orbitals. FV+basis denotes calculations with 31 frozen virtual orbitals and reduced basis set: aug-cc-pVDZ on heavy atoms and cc-pVDZ on H.

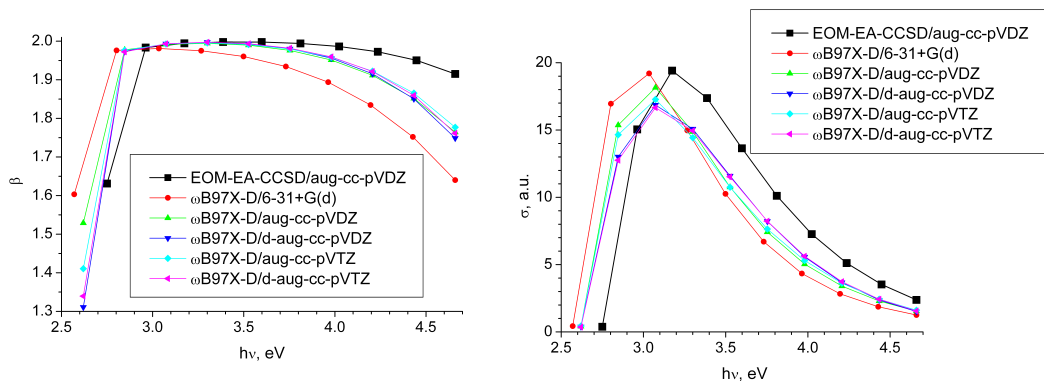


Figure 4.20: The effect of the basis set on β and σ for $\text{Na}(\text{NH}_3)_5$ computed with $\omega\text{B97X-D}$.

4.6 Appendix B: Wave function analysis

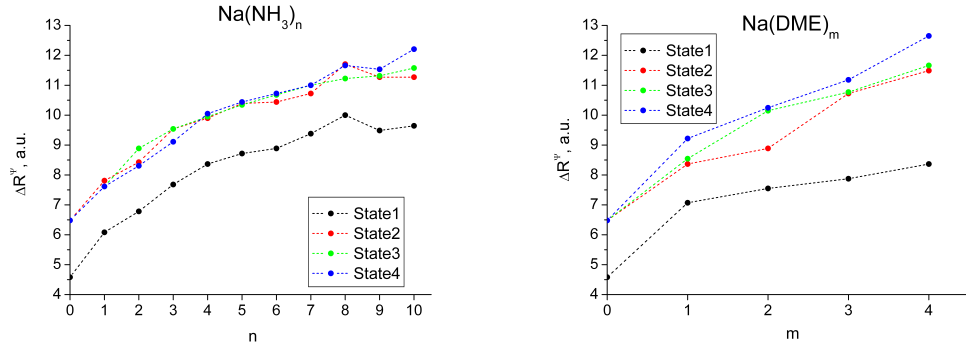


Figure 4.21: Dependence of states' size, ΔR^Ψ , on cluster size for the four lowest electronic states of $\text{Na}(\text{NH}_3)_n$, $n=0\text{-}10$, and $\text{Na}(\text{DME})_m$, $m=0\text{-}4$, at the EOM-EA-CCSD/aug-cc-pVDZ level of theory.

Koopmans' character of the EOM-EA states can be quantified by the weight of Hartree-Fock LUMO in the first Dyson orbital, $w(\text{LUMO}) = c_{\text{LUMO}}^{\text{left}} * c_{\text{LUMO}}^{\text{right}}$, where c are the coefficients of the normalized left and right Dyson orbitals. $w(\text{LUMO})$ are shown in Fig. 4.3 of the main manuscript. As we can see, with the increasing size of the system, the deviation from the Koopmans' picture increases, and the discrepancy is larger for DME clusters.

4.7 Appendix C: The effect of thermal fluctuations on the observables

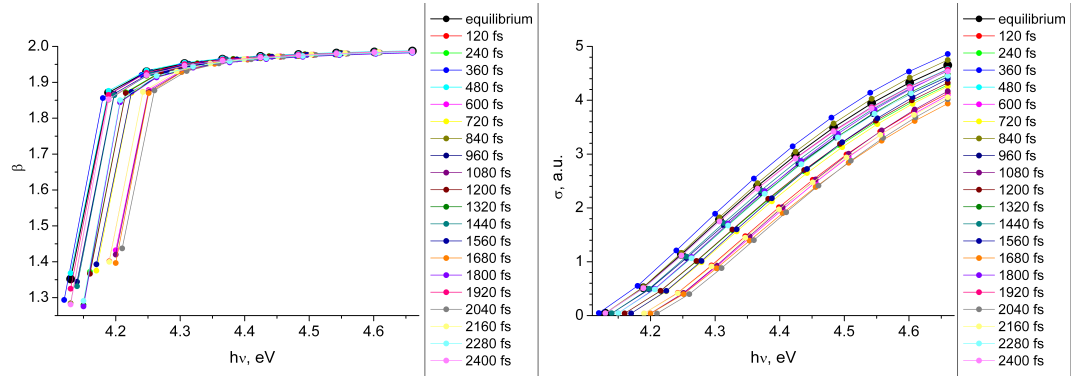


Figure 4.22: Anisotropy parameters and total cross-sections computed at different snapshots from the equilibrium trajectory of $\text{Na}(\text{NH}_3)$. EOM-EA-CCSD/aug-cc-pVDZ.

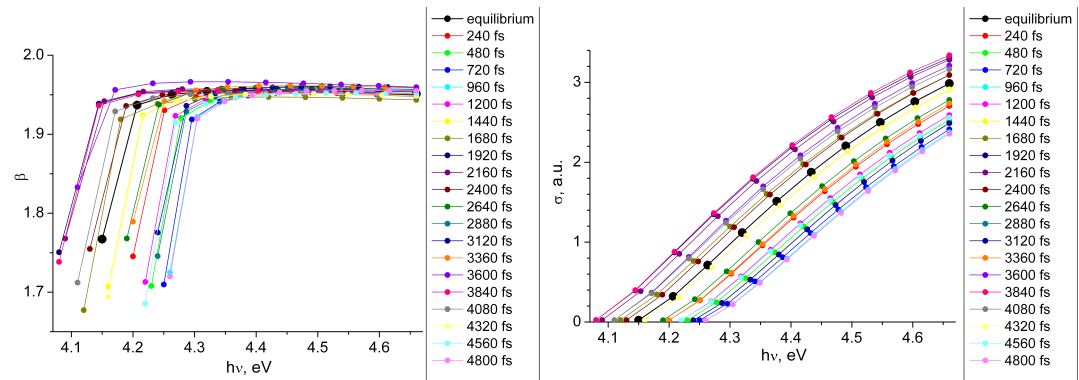


Figure 4.23: Anisotropy parameters and total cross-sections computed at different snapshots from the equilibrium trajectory of $\text{Na}(\text{DME})$. EOM-EA-CCSD/aug-cc-pVDZ.

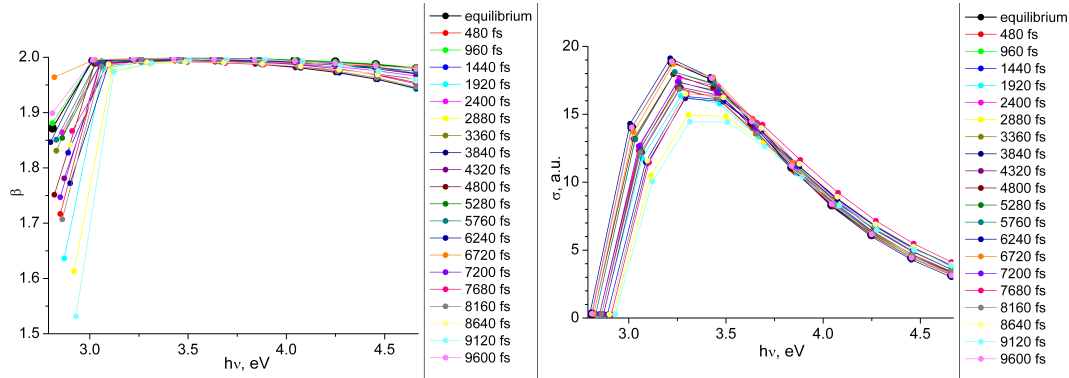


Figure 4.24: Anisotropy parameters and total cross-sections computed at different snapshots from the equilibrium trajectory of $\text{Na}(\text{NH}_3)_4$. EOM-EA-CCSD/aug-cc-pVDZ.

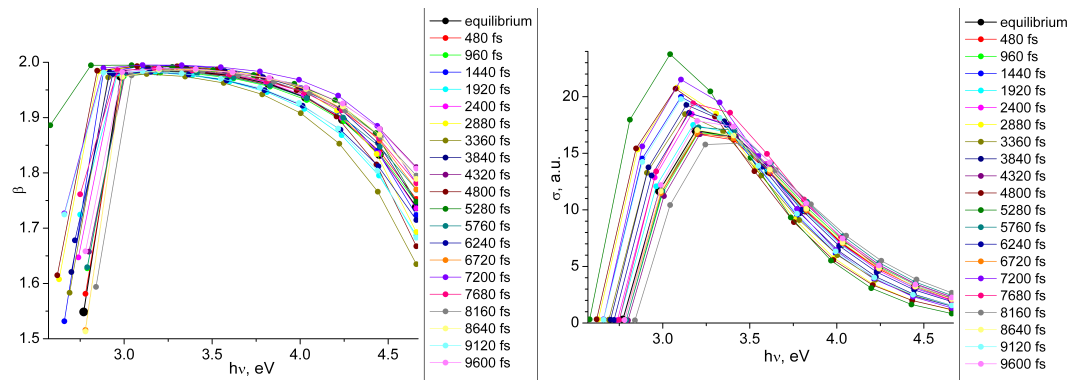


Figure 4.25: Anisotropy parameters and total cross-sections computed at different snapshots from the equilibrium trajectory of $\text{Na}(\text{NH}_3)_6$. EOM-EA-CCSD/aug-cc-pVDZ.

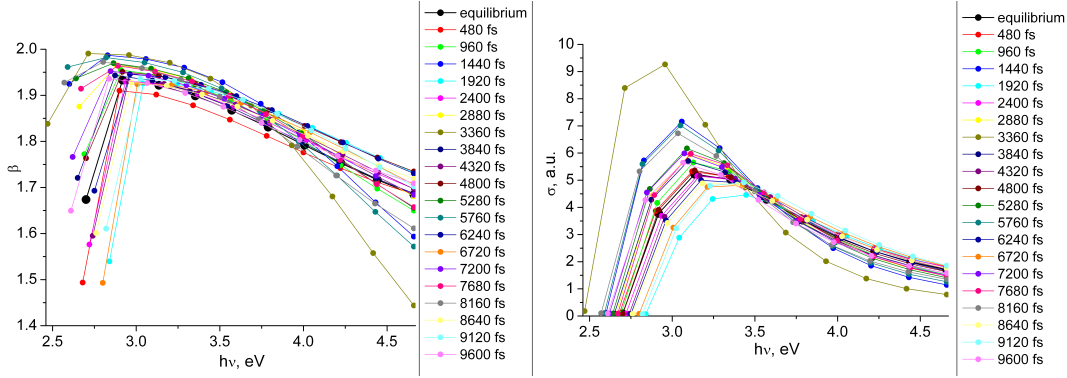


Figure 4.26: Anisotropy parameters and total cross-sections computed at different snapshots from the equilibrium trajectory of $\text{Na}(\text{DME})_4$. EOM-EA-CCSD/aug-cc-pVDZ.

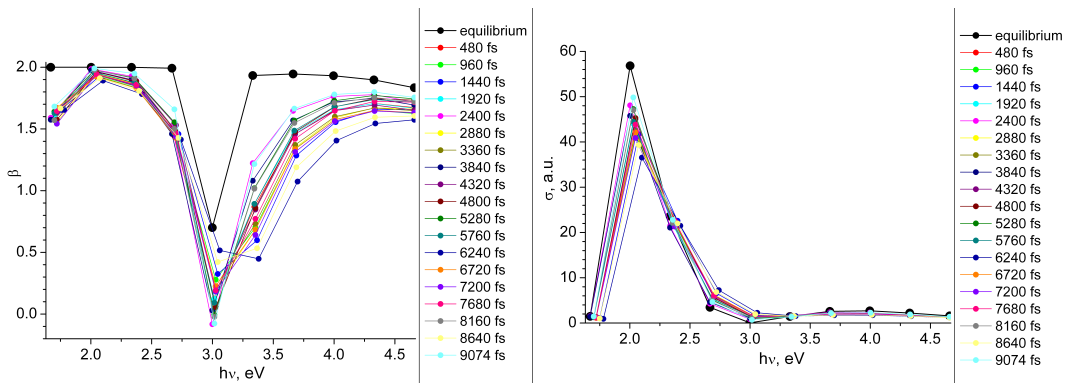
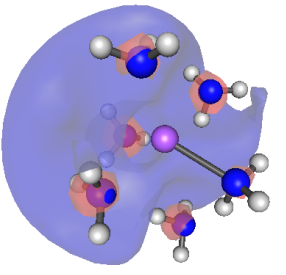


Figure 4.27: Anisotropy parameters and total cross-sections computed at different snapshots from the equilibrium trajectory of $\text{Na}(\text{DME})_6$. $\omega\text{B97X-D}/6-31+\text{G(d)}$.

Table 4.4: State properties computed using the EOM-EA-CCSD/aug-cc-pVDZ wave functions and properties of the Dyson orbitals for the lowest electronic state of $\text{Na}(\text{NH}_3)_6$ at selected snapshots. VIEs are given in eV and other quantities in a.u.

Snapshot, fs	Properties	Values	Picture
equilibrium	VIE μ ΔR^Ψ \bar{R}^d d_{eh}	2.76 2.17 8.89 7.94 3.98	
3360	VIE μ ΔR^Ψ \bar{R}^d d_{eh}	2.68 2.13 8.94 8.13 4.23	
4800	VIE μ ΔR^Ψ \bar{R}^d d_{eh}	2.61 2.03 9.14 8.50 3.01	
5280	VIE μ ΔR^Ψ	2.57 0.97 9.22	

	\bar{R}^d	8.99	
	d_{eh}	1.47	
8160	VIE	2.83	
	μ	2.00	
	ΔR^Ψ	8.63	
	\bar{R}^d	7.80	
	d_{eh}	3.93	

4.8 Appendix D: Comparison of DFT and EOM-EA Dyson orbitals: The effect on β and σ

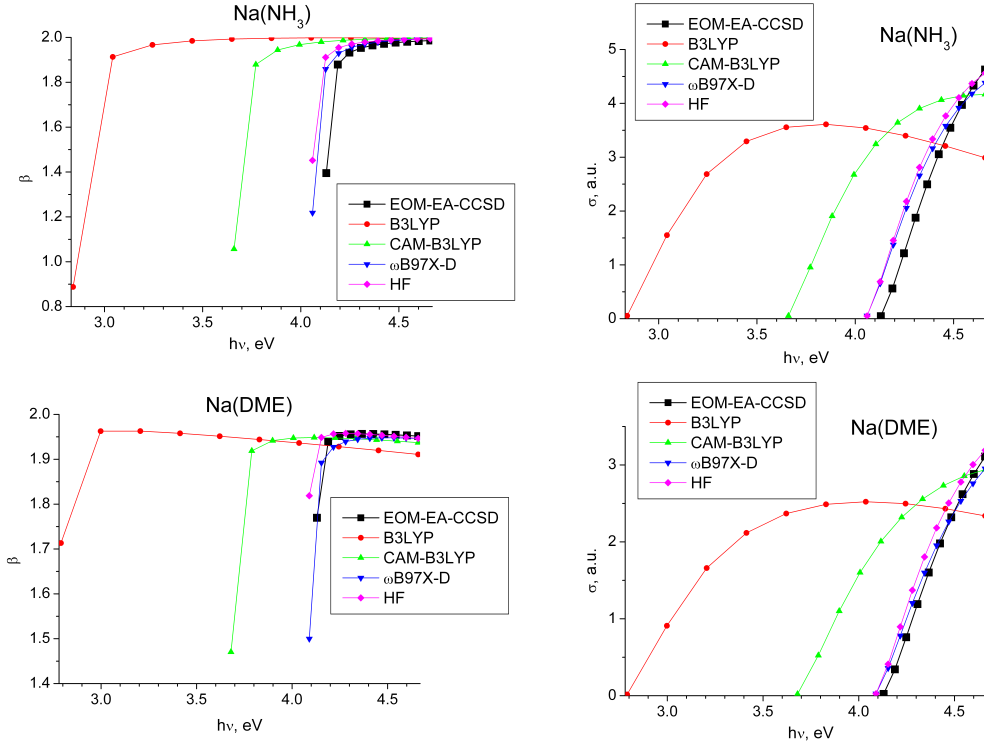


Figure 4.28: Anisotropy parameters and total cross-sections computed using the EOM-EA-CCSD Dyson orbitals and Koopmans' theorem (Kohn-Sham and Hartree-Fock SOMOs) for $\text{Na}(\text{NH}_3)$ (upper panel) and $\text{Na}(\text{DME})$ (lower panel).

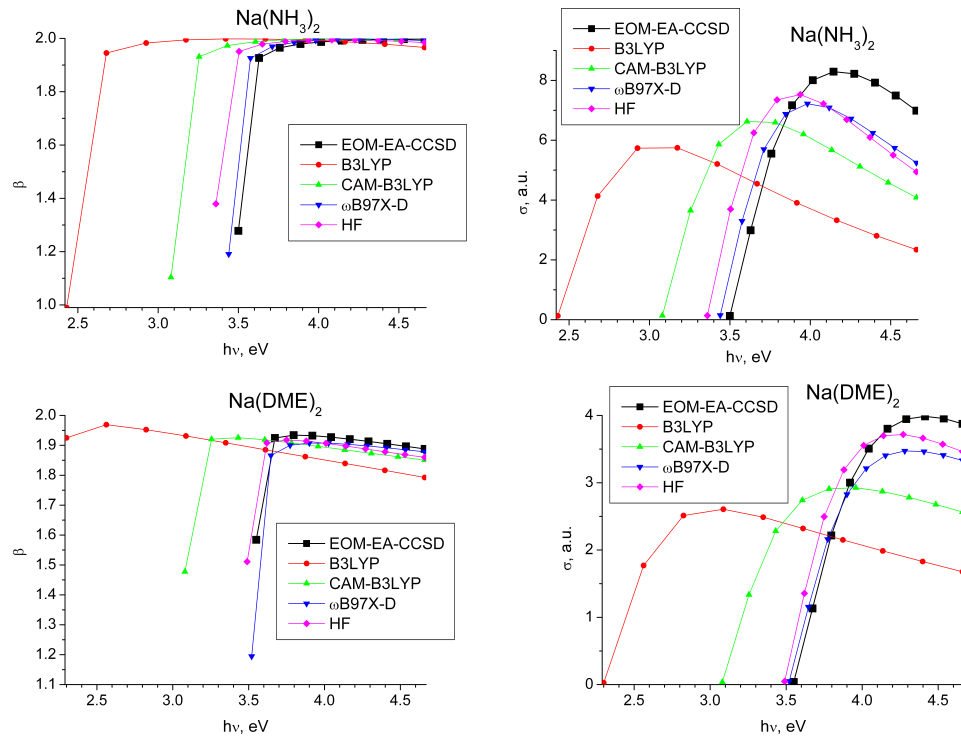


Figure 4.29: Anisotropy parameters and total cross-sections computed using the EOM-EA-CCSD Dyson orbitals and Koopmans' theorem (Kohn-Sham and Hartree-Fock SOMOs) for $\text{Na}(\text{NH}_3)_2$ (upper panel) and $\text{Na}(\text{DME})_2$ (lower panel).

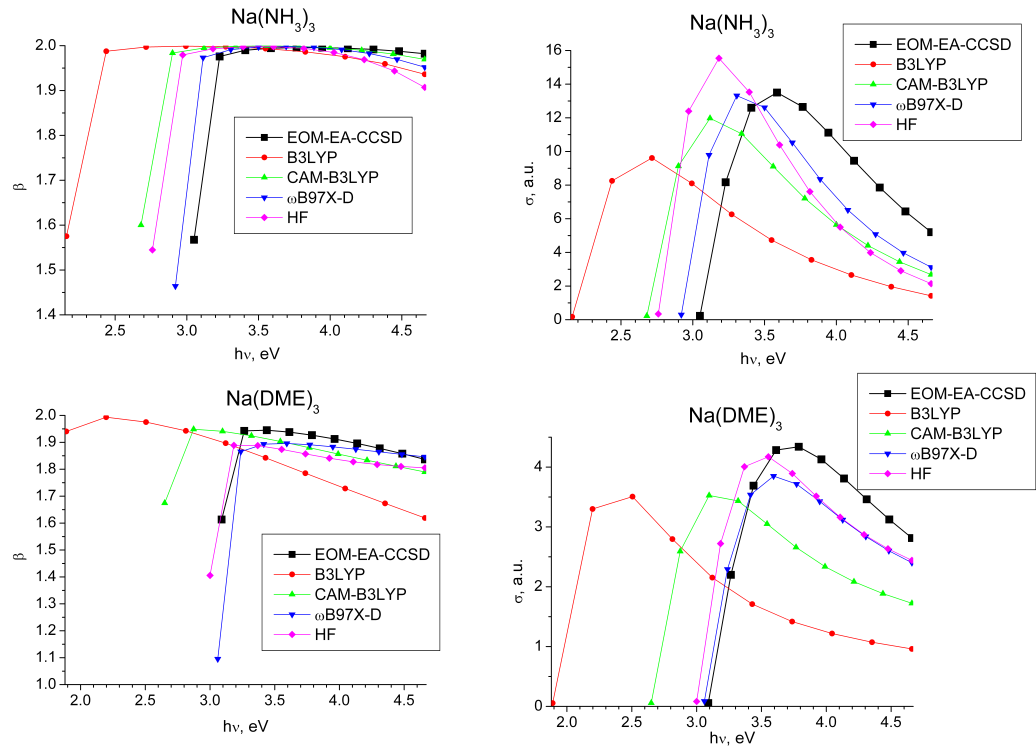


Figure 4.30: Anisotropy parameters and total cross-sections computed using the EOM-EA-CCSD Dyson orbitals and Koopmans' theorem (Kohn-Sham and Hartree-Fock SOMOs) for $\text{Na}(\text{NH}_3)_3$ (upper panel) and $\text{Na}(\text{DME})_3$ (lower panel).

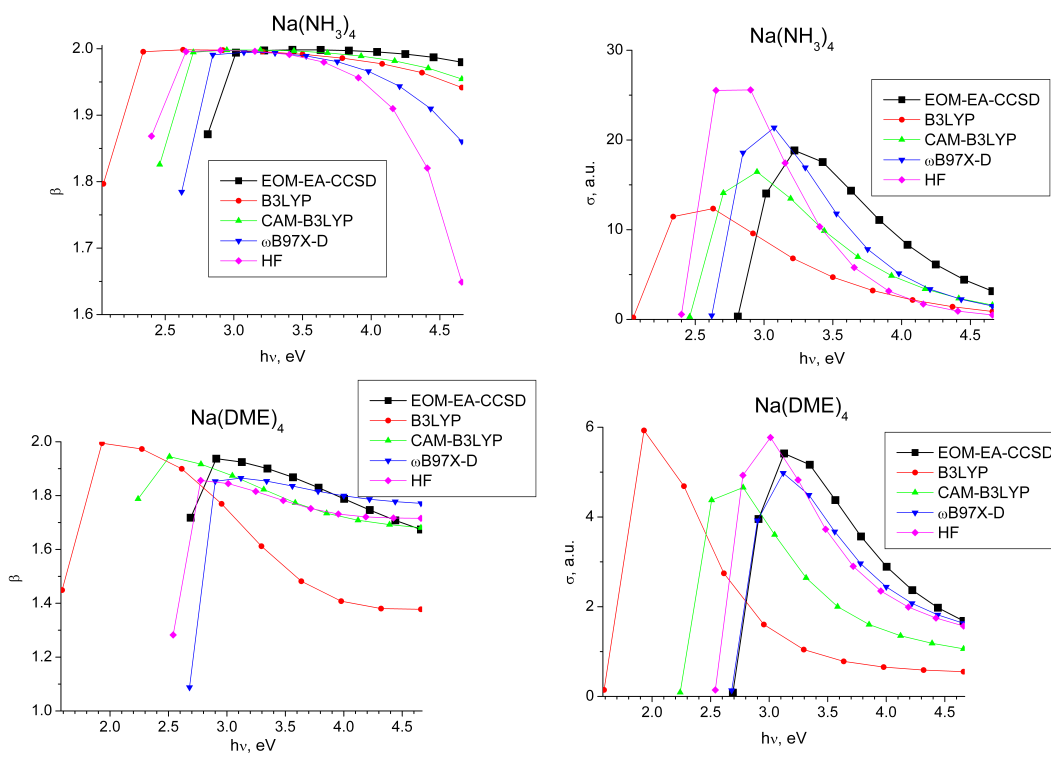


Figure 4.31: Anisotropy parameters and total cross-sections computed using the EOM-EA-CCSD Dyson orbitals and Koopmans' theorem (Kohn-Sham and Hartree-Fock SOMOs) for $\text{Na}(\text{NH}_3)_4$ (upper panel) and $\text{Na}(\text{DME})_4$ (lower panel).

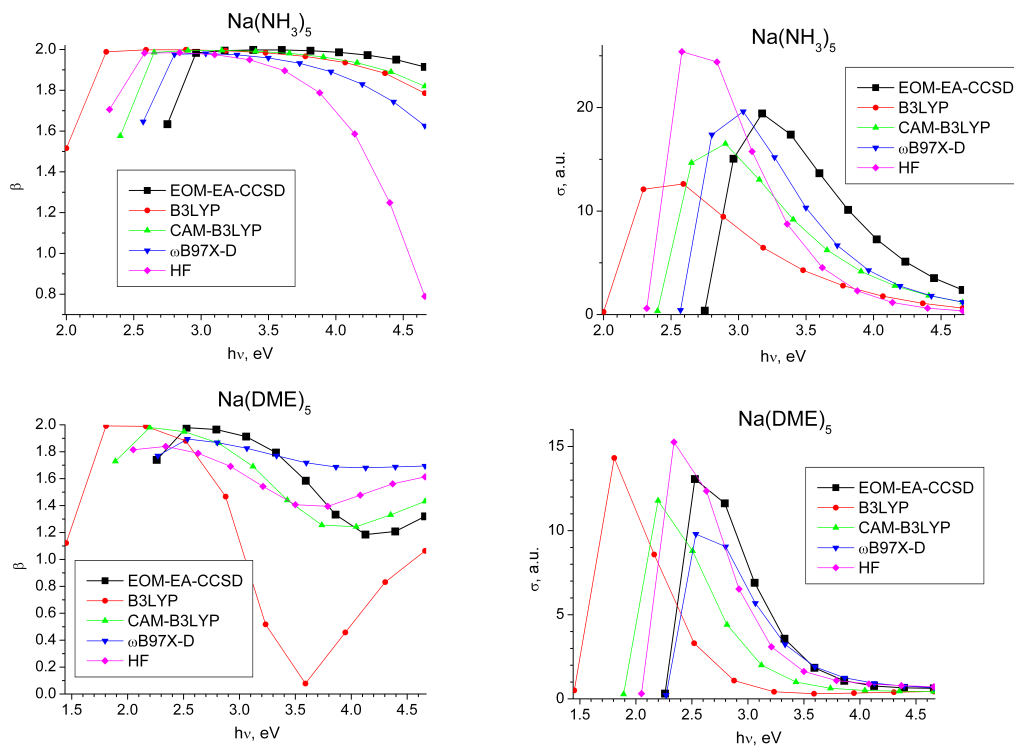


Figure 4.32: Anisotropy parameters and total cross-sections computed using the EOM-EA-CCSD Dyson orbitals and Koopmans' theorem (Kohn-Sham and Hartree-Fock SOMOs) for $\text{Na}(\text{NH}_3)_5$ (upper panel) and $\text{Na}(\text{DME})_5$ (lower panel).

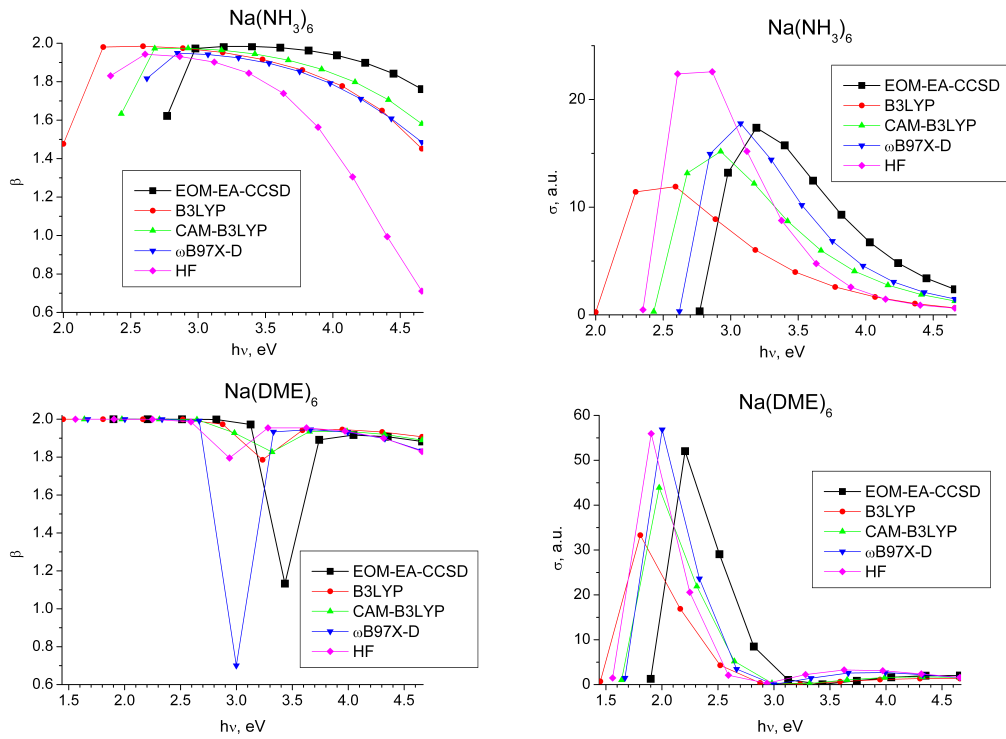


Figure 4.33: Anisotropy parameters and total cross-sections computed using the EOM-EA-CCSD Dyson orbitals and Koopmans' theorem (Kohn-Sham and Hartree-Fock SOMOs) for $\text{Na}(\text{NH}_3)_6$ (upper panel) and $\text{Na}(\text{DME})_6$ (lower panel).

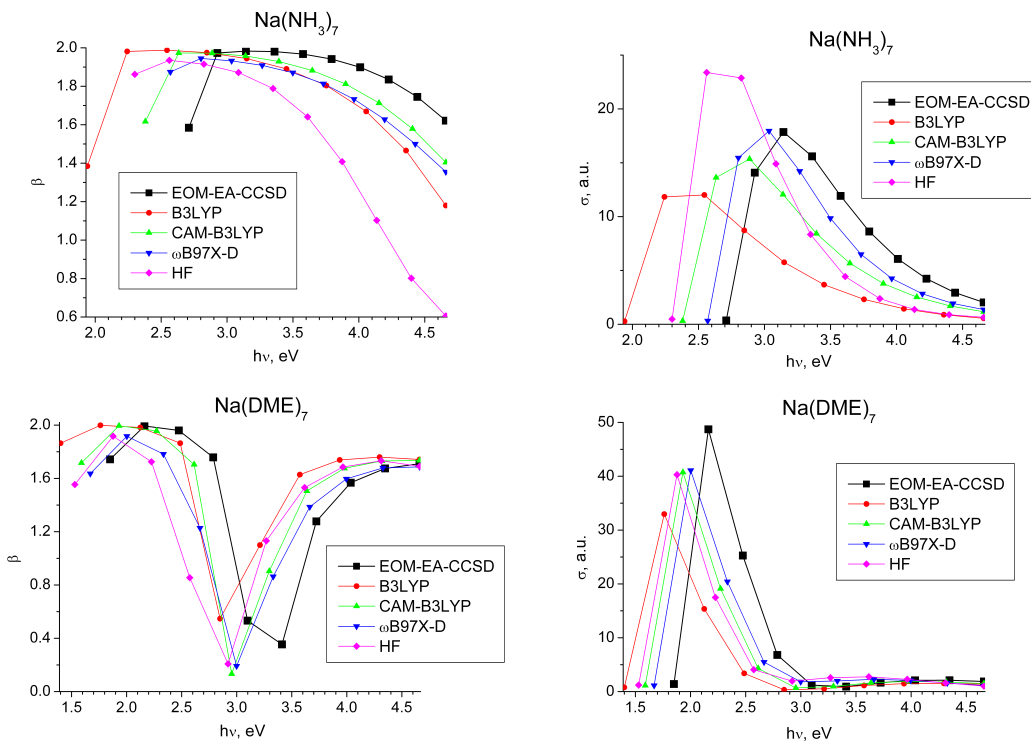


Figure 4.34: Anisotropy parameters and total cross-sections computed using the EOM-EA-CCSD Dyson orbitals and Koopmans' theorem (Kohn-Sham and Hartree-Fock SOMOs) for $\text{Na}(\text{NH}_3)_7$ (upper panel) and $\text{Na}(\text{DME})_7$ (lower panel).

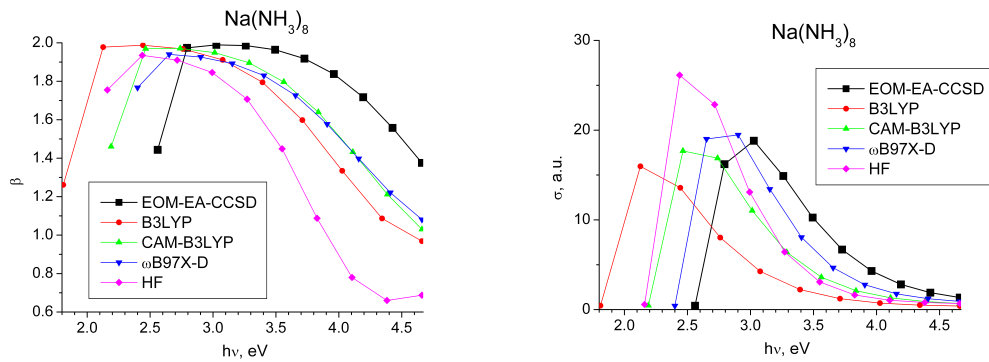


Figure 4.35: Anisotropy parameters and total cross-sections computed using the EOM-EA-CCSD Dyson orbitals and Koopmans' theorem (Kohn-Sham and Hartree-Fock SOMOs) for $\text{Na}(\text{NH}_3)_8$.

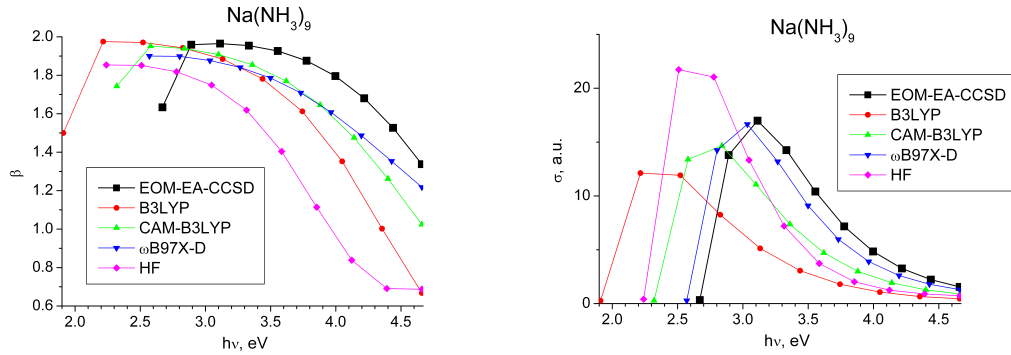


Figure 4.36: Anisotropy parameters and total cross-sections computed using the EOM-EA-CCSD Dyson orbitals and Koopmans' theorem (Kohn-Sham and Hartree-Fock SOMOs) for $\text{Na}(\text{NH}_3)_9$.

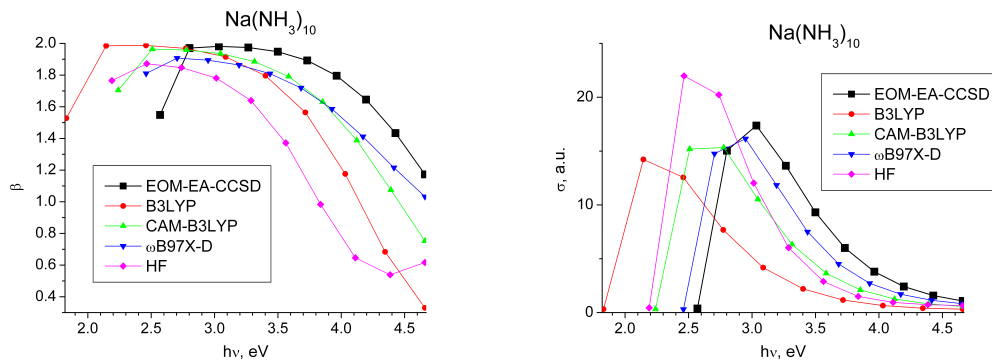


Figure 4.37: Anisotropy parameters and total cross-sections computed using the EOM-EA-CCSD Dyson orbitals and Koopmans' theorem (Kohn-Sham and Hartree-Fock SOMOs) for $\text{Na}(\text{NH}_3)_{10}$.

4.9 Chapter 4 references

- [1] J. Simons. Detachment processes for molecular anions. In C.Y. Ng, editor, *Photoionization and Photodetachment*, volume 10, Part II of *Advanced Series in Physical Chemistry*. World Scientific Publishing Co., Singapore, 2000.
- [2] A. Sanov and R. Mabbs. Photoelectron imaging of negative ions. *Int. Rev. Phys. Chem.*, 27:53–85, 2008.
- [3] K.L. Reid. Picosecond time-resolved photoelectron spectroscopy as a means of gaining insight into mechanisms of intramolecular vibrational energy redistribution in excited states. *Int. Rev. Phys. Chem.*, 27:607–628, 2008.
- [4] O. Welz, J.D. Savee, D.L. Osborn, S.S. Vasu, C.J. Percival, D.E. Shallcross, and C.A. Taatjes. Direct kinetic measurements of Criegee intermediate (CH_2OO) formed by reaction of CH_2I with O_2 . *Science*, 335:204–207, 2012.
- [5] D.M. Neumark. Probing the transition state with negative ion photodetachment: experiment and theory. *Phys. Chem. Chem. Phys.*, 7:433, 2005.
- [6] D.M. Neumark. Probing chemical dynamics with negative ions. *J. Chem. Phys.*, 125:132303, 2006.
- [7] J. Linderberg and Y. Öhrn. *Propagators in quantum chemistry*. Academic, London, 1973.
- [8] J.V. Ortiz. Toward an exact one-electron picture of chemical bonding. *Adv. Quantum Chem.*, 35:33–52, 1999.
- [9] H.R. Hudock, B.G. Levine, A.L. Thompson, H. Satzger, D. Townsend, N. Gador, S. Ulrich, A. Stolow, and T.J. Martínez. Ab initio molecular dynamics and time-resolved photoelectron spectroscopy of electronically excited uracil and thymine. *J. Phys. Chem. A*, 111:8500–8598, 2007.
- [10] C.M. Oana and A.I. Krylov. Cross sections and photoelectron angular distributions in photodetachment from negative ions using equation-of-motion coupled-cluster Dyson orbitals. *J. Chem. Phys.*, 131:124114, 2009.
- [11] H.A. Bethe and E.E. Salpeter. *Quantum mechanics of one and two electron atoms*. Plenum, New York, 1977.

- [12] K.J. Reed, A.H. Zimmerman, H.C. Andersen, and J.I. Brauman. Cross sections for photodetachment of electrons from negative ions near threshold. *J. Chem. Phys.*, 64:1368–1375, 1976.
- [13] C.M. Oana and A.I. Krylov. Dyson orbitals for ionization from the ground and electronically excited states within equation-of-motion coupled-cluster formalism: Theory, implementation, and examples. *J. Chem. Phys.*, 127:234106, 2007.
- [14] S. Gozem, A.O. Gunina, T. Ichino, D.L. Osborn, J.F. Stanton, and A.I. Krylov. Photoelectron wave function in photoionization: Plane wave or Coulomb wave? *J. Phys. Chem. Lett.*, 6:4532–4540, 2015.
- [15] A.I. Krylov. Equation-of-motion coupled-cluster methods for open-shell and electronically excited species: The hitchhiker’s guide to Fock space. *Annu. Rev. Phys. Chem.*, 59:433–462, 2008.
- [16] K. Sneskov and O. Christiansen. Excited state coupled cluster methods. *WIREs Comput. Mol. Sci.*, 2:566, 2012.
- [17] R.J. Bartlett. Coupled-cluster theory and its equation-of-motion extensions. *WIREs Comput. Mol. Sci.*, 2(1):126–138, 2012.
- [18] A.H.C. West, B.L. Yoder, D. Luckhaus, C.-M. Saak, M. Doppelbauer, and R. Signorell. Angle-resolved photoemission of solvated electrons in sodium-doped clusters. *J. Phys. Chem. Lett.*, 6:1487–1492, 2015.
- [19] A.H.C. West, B.L. Yoder, D. Luckhaus, and R. Signorell. Solvated electrons in clusters: Magic numbers for the photoelectron anisotropy. *J. Phys. Chem. A*, 119:1237612382, 2015.
- [20] R. Signorell, B.L. Yoder, A.H.C. West, J.J. Ferreiro, and C.-M. Saak. Angle-resolved valence shell photoelectron spectroscopy of neutral nanosized molecular aggregates. *Chem. Science*, 5:12831295, 2014.
- [21] T. Zeuch and U. Buck. Sodium doped hydrogen bonded clusters: Solvated electrons and size selection. *Chem. Phys. Lett.*, 579:1–10, 2013.
- [22] D. Smidova, J. Lengyel, A. Pysanenko, J. Med, P. Slavicek, and M. Farnik. Reactivity of hydrated electron in finite size system: Sodium pickup on mixed N₂O-water nanoparticles. *J. Phys. Chem. Lett.*, 6:2865–2869, 2015.
- [23] B.C. Garrett, D.A. Dixon, D.M. Camaioni, D.M. Chipman, M.A. Johnson, C.D. Jonah, G.A. Kimmel, J.H. Miller, T.N. Rescigno, P.J. Rossky, S.S. Xantheas, S.D. Colson, A.H. Laufer, D. Ray, P.F. Barbara, D.M. Bartels, K.H. Becker, H. Bowen, S.E. Bradforth, I. Carmichael, J.V. Coe, L.R. Corrales, J.P. Cowin, M. Dupuis,

- K.B. Eisenthal, J.A. Franz, M.S. Gutowski, K.D. Jordan, B.D. Kay, J.A. LaVerne JA, S.V. Lymar, T.E. Madey, C.W. McCurdy, D. Meisel, S. Mukamel, A.R. Nilsson, T.M. Orlando, N.G. Petrik, S.M. Pimblott, J.R. Rustad, G.K. Schenter, S.J. Singer, A. Tokmakoff, L.S. Wang, C. Wittig, and T.S. Zwier. Role of water in electron-initiated processes and radical chemistry: Issues and scientific advances. *Chem. Rev.*, 105:355–389, 2005.
- [24] O.T. Ehrler and D.M. Neumark. Dynamics of electron solvation in molecular clusters. *Acc. Chem. Res.*, 42:769, 2009.
- [25] J.M. Herbert and L.D. Jacobson. Nature most squishy ion: The important role of solvent polarization in the description of the hydrated electron. *Int. Rev. Phys. Chem.*, 30:1–48, 2010.
- [26] J. M. Herbert. The quantum chemistry of loosely-bound electrons. *Rev. Comp. Chem.*, 28:391–517, 2015.
- [27] J. Cooper and R.N. Zare. Angular distribution of photoelectrons. *J. Chem. Phys.*, 48:942–943, 1968.
- [28] Y. Yamamoto, Y.-I. Suzuki, G. Tomasello, T. Horio, S. Karashima, R. Mitríć, and T. Suzuki. Time- and angle-resolved photoemission spectroscopy of hydrated electrons near a liquid water surface. *Phys. Rev. Lett.*, 112:187603, 2014.
- [29] K. Hashimoto and K. Daigoku. Ground and low-lying excited states of $\text{Na}(\text{NH}_3)_n$ and $\text{Na}(\text{H}_2\text{O})_n$ clusters: Formation and localization of solvated electron. *Chem. Phys. Lett.*, 469:62–67, 2009.
- [30] R.J. Bartlett. Many-body perturbation theory and coupled cluster theory for electron correlation in molecules. *Annu. Rev. Phys. Chem.*, 32:359–401, 1981.
- [31] R.J. Bartlett and J.F. Stanton. Applications of post-Hartree-Fock methods: A tutorial. *Rev. Comp. Chem.*, 5:65–169, 1994.
- [32] R.J. Bartlett. To multireference or not to multireference: That is the question? *Int. J. Mol. Sci.*, 3:579–603, 2002.
- [33] R.J. Bartlett. The coupled-cluster revolution. *Mol. Phys.*, 108:2905–2920, 2010.
- [34] T.-C. Jagau and A.I. Krylov. Characterizing metastable states beyond energies and lifetimes: Dyson orbitals and transition dipole moments. *J. Chem. Phys.*, 144:054113, 2016.
- [35] H. Reisler and A.I. Krylov. Interacting Rydberg and valence states in radicals and molecules: Experimental and theoretical studies. *Int. Rev. Phys. Chem.*, 28:267–308, 2009.

- [36] J.J. Sakurai. *Modern Quantum Mechanics*. Addison-Wesley Publishing Company, 1995.
- [37] L.D. Landau and E.M. Lifshitz. *Quantum Mechanics: Non-relativistic theory*. Pergamon, Oxford, 1977.
- [38] S. Gozem and A.I. Krylov. ezDyson user's manual, 2015.
ezDyson, <http://iopenshell.usc.edu/downloads/>.
- [39] Shao, Y.; Gan, Z.; Epifanovsky, E.; Gilbert, A.T.B.; Wormit, M.; Kussmann, J.; Lange, A.W.; Behn, A.; Deng, J.; Feng, X., et al. Advances in molecular quantum chemistry contained in the Q-Chem 4 program package. *Mol. Phys.*, 113:184–215, 2015.
- [40] A.I. Krylov and P.M.W. Gill. Q-Chem: An engine for innovation. *WIREs Comput. Mol. Sci.*, 3:317–326, 2013.
- [41] J.-D. Chai and M. Head-Gordon. Systematic optimization of long-range corrected hybrid density functionals. *J. Chem. Phys.*, 128:084106, 2008.
- [42] J.-D. Chai and M. Head-Gordon. Long-range corrected hybrid density functionals with damped atom-atom dispersion interactions. *Phys. Chem. Chem. Phys.*, 10:6615–6620, 2008.
- [43] P.J. Stephens, F.J. Devlin, C.F. Chabalowski, and M.J. Frisch. *Ab Initio* calculation of vibrational absorption and circular dichroism spectra using density functional force fields. *J. Phys. Chem.*, 98:11623–11627, 1994.
- [44] T. Yanai, D.P. Tew, and N.C. Handy. A new hybrid exchange–correlation functional using the Coulomb-attenuating method (CAM-B3LYP). *Chem. Phys. Lett.*, 393:51 – 57, 2004.

Chapter 5: Photoionization of arginine in gas phase and in solution

5.1 Introduction

Gas-phase studies of amino acids are essential for extracting thermochemical information necessary to understand fragmentation patterns¹ in proteomics² and genomics³. The ionization energies of amino acids in the gas phase are also needed for studies of amino acids on semiconducting surfaces⁴ relevant in the context of new types of bio-devices. Since they are non-volatile and fragile, introducing amino acids into the gas phase is a challenging task. Moreover, amino acids easily undergo dissociative ionization facilitated by depositing internal energy into molecules upon vaporization. Therefore, for measuring ionization energies and studying fragmentation channels it is important to distinguish between thermal decomposition in the gas phase and fragmentation upon ionization. In the extensive study of Lichtenberger *et. al.*⁵, which focused on determining correlations between adiabatic ionization energies (AIEs) and proton affinities, two amino acids are missing due to the complete absence of data: histidine and arginine. The two are similar in that they have large proton-acceptor functional groups in their long side chains, leading to existence of numerous low-lying isomers. Histidine was recently studied⁶ by mass spectrometry with VUV synchrotron radiation ionization

using a novel method of impaction of nanoparticles on a heater for generating gas-phase amino acids. Accompanying theoretical modeling (using B3LYP) suggested that seven conformers are accessible under the experimental conditions.

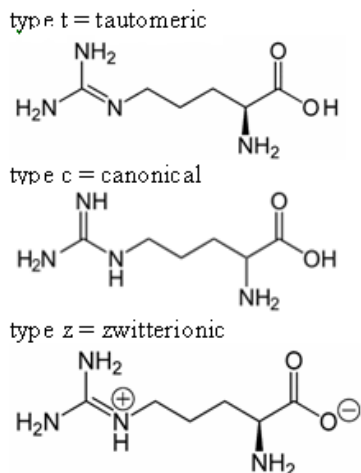


Figure 5.1: Different forms of arginine.

Arginine, in turn, was shown⁷ to have over a hundred isomers – setting the record among 20 natural amino acids. In the gas phase, conformers of canonical or tautomeric type (sketched in Fig. 5.1) are the most abundant. The existence of zwitterionic forms in the gas phase has been extensively debated⁸, but *ab initio* calculations⁷ suggested that, despite being considerably higher in energy, they are within thermally accessible range. Even at low temperatures, several isomers have considerable populations in equilibrium vapor, making the system intrinsically multi-isomeric; at room temperature at least eight isomers are present⁷. The large number of isomers arise due to a large and flexible side chain with the guanidine group: it participates in various non-covalent interactions, exhibiting stereoelectronic effects and forming multiple red- and blue-shifting hydrogen bonds, and even double hydrogen bonds. This imposes stringent requirements for

appropriate electronic structure method and basis set, as shown in an extensive benchmark study⁹. For instance, including perturbative triples correction (T) is highly desirable for coupled-cluster with single and double substitutions (CCSD), while preferable density functional theory (DFT) functionals are of double-hybrid type, and at least D3 correction is necessary for dispersion. Among lower-rung functionals, hybrid B3LYP¹⁰ and ω B97X¹¹ perform relatively well, provided that they are combined with a suitable description of dispersion. In terms of basis sets, extensive polarization and diffusion contributions are important, however, going beyond triple ζ is not needed. In geometry optimizations, canonical protocol of isomer search with semiempirical PM3 method, highly successful in many cases, overlooks tens of low-lying isomers; B3LYP performs well as a starting point, but further second order perturbation theory (MP2) refinement is desirable⁷. Clearly, studying photoionization of such complicated system calls for a high level of theory, such as the equation-of-motion coupled-cluster with single and double substitutions for ionization potential (EOM-IP-CCSD) method^{12–14}.

5.2 Computational details

Equilibrium geometries of neutral arginine (shown in Fig. 5.2) were obtained from Ref. 7, where they were computed at the MP2/6-31++G(d,p) level of theory. We labeled isomers according to the order of CCSD/6-31++G(d,p) total energies from Ref. 7 (i.e., t1 corresponds to the lowest energy tautomeric form). We performed calculations of vertical ionization energies (VIEs) and Dyson orbitals of selected isomers using EOM-IP-CCSD/aug-cc-pVDZ. We optimized the structures of gas-phase cations using ω B97X-D3/6-31++G(3df,2pd), starting from the geometries of neutral isomers (which corresponds to vertical ionization). We subsequently computed AIEs as difference between the EOM-IP-CCSD energy of the cation at its equilibrium structure and the CCSD total

energy of the neutral at the corresponding equilibrium structure, corrected by zero-point vibrational energies computed with ω B97X-D3/6-31++G(d,p).

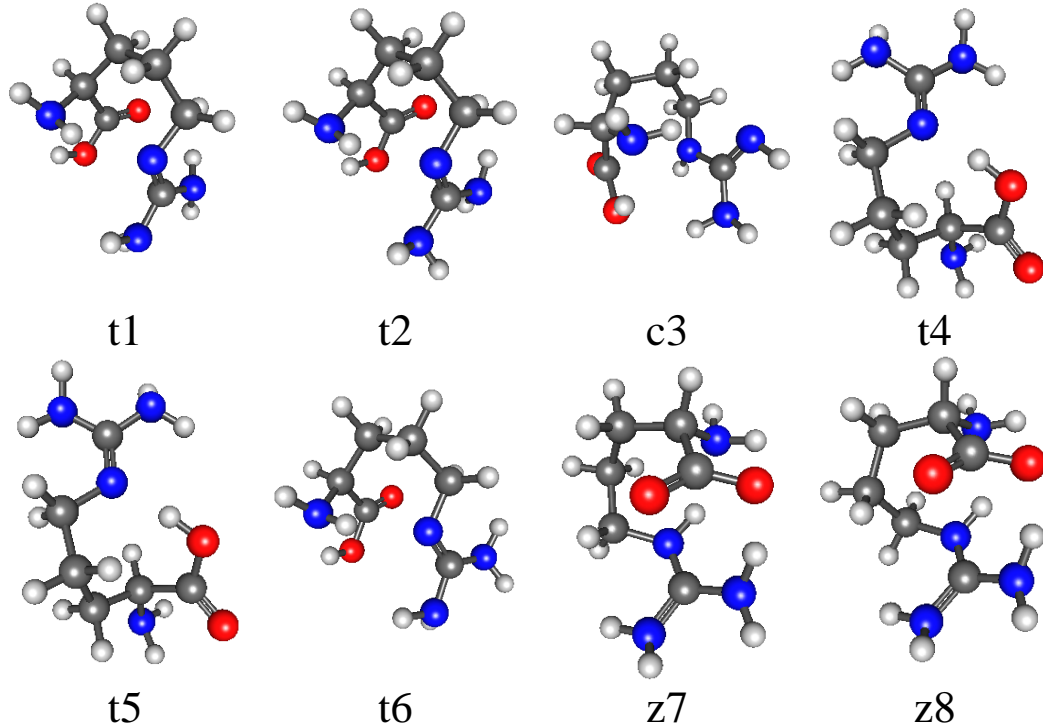


Figure 5.2: Isomers of arginine considered in this work. t_i denotes tautomeric conformers, c_3 denotes canonical form, and z_j denotes zwitterionic conformers.

To model the impact of energy imparted by ionizing photons, we carried out *ab initio* molecular dynamics (AIMD) simulations for cationic species with ω B97X-D3/6-31++G(d,p). The 9675 fs trajectory was initiated from the neutral equilibrium geometry and the initial velocities were randomly sampled from the Maxwell-Boltzmann distribution at 10,000 K (\sim 1 eV of excess energy), 1000 K (\sim 0.1 eV of excess energy), and 400 K.

To model ionization in condensed phase, we performed geometry optimizations of aqueous neutral and cationic arginine with ω B97X-D3/6-31++G(3df,2pd)/CPCM (conductor-like polarizable continuum model, PCM). The equilibrium structures of the

neutral species in water were sampled using classical molecular dynamics (MD) with the OPLS-AA force field and SPC/E description for water in a cubic 20 Å box with periodic boundary conditions. We considered two forms: carboxyl-to-amino zwitterionic structure without counterions and a singly protonated at the guanidine group form with the Cl⁻ counterion. The initial geometries were taken from the gas phase and then optimized with a chosen force field in solution; the initial velocities were randomly sampled from the Boltzmann distribution at 300 K. Following temperature equilibration in the NVT ensemble and density equilibration in the NPT ensemble, 1 ns production run was performed. We computed VIEs at snapshots (taken every 50 ps, total of 21 snapshots) using EOM-IP-CCSD/MM (molecular mechanics) with the quantum mechanical (QM) part comprising arginine. Such calculations agree within 0.2 eV for the 8 lowest VIEs with the results obtained for the larger QM part, which included arginine and 7 or 6 water molecules. We used a truncated basis set: aug-cc-pVDZ for heavy atoms and cc-pVDZ for H atoms; these VIEs agree with the full aug-cc-pVDZ description within 0.1 eV. For one snapshot, we also considered EOM-IP-CCSD/CPCM and microhydrated clusters of varying size in vacuum (described by EOM-IP-CCSD). We selected water molecules for the QM part and for microsolvated clusters based on hydrogen bonding criteria as follows: one closest water molecule, three donor water molecules near the carboxyl group, three acceptor water molecules, six molecules (a combination of two previous triades), one extra closest water molecule giving seven in total. For microsolvated clusters we also included one with three more water molecules, totaling ten. Unfortunately, including more than 7 water molecules into the QM region within QM/MM or QM/CPCM turns out to be too expensive at the EOM-CC level and an attempt to further reduce basis set (to cc-pVDZ on all atoms) introduces considerable 0.2-0.3 eV errors.

All electronic structure calculations were carried out with the Q-Chem package¹⁵ and molecular dynamics simulations in water were performed using Gromacs¹⁶.

5.3 Results and discussion

5.3.1 Gas-phase ionization

On the basis of previously reported⁷ computed equilibrium populations of gaseous arginine, we considered six lowest-lying conformers of the canonical and tautomeric type, and two zwitterionic conformers (see Fig. 5.2). For each structure, we computed 9 VIEs (5 for zwitterions) based on the analysis of energies of the occupied Hartree-Fock (HF) orbitals. All these ionizations are almost pure one-electron transitions, with the norms of Dyson orbitals being 0.94–0.95. They also follow Koopmans’ predictions in terms of the leading contributing canonical orbitals, except for the second and the third transitions in zwitterionic conformers, which have leading contributions from HOMO-2 and HOMO-1, respectively (where HOMO denotes highest occupied molecular orbital). The computed lowest VIEs, AIEs, and the corresponding Dyson orbitals are collected in Fig. 5.3.

The optimization of the cationic structures reveals that several conformers undergo dissociative ionization producing neutral CO₂ and amine cations. These processes are highly exothermic: 2.2 eV for the tautomeric conformers and 1.6 eV for the zwitterion. Other isomers undergo substantial structural relaxation, resulting in a 1 eV difference between the lowest VIE and AIE. Such significant relaxation hints that Franck-Condon factors for the 0-0 transition might be unfavorable. All non-dissociating conformers maintain their type of structure (i.e., they remain tautomeric, or canonical, or zwitterionic). The leading contributions to the Dyson orbitals come from the guanidine and/or

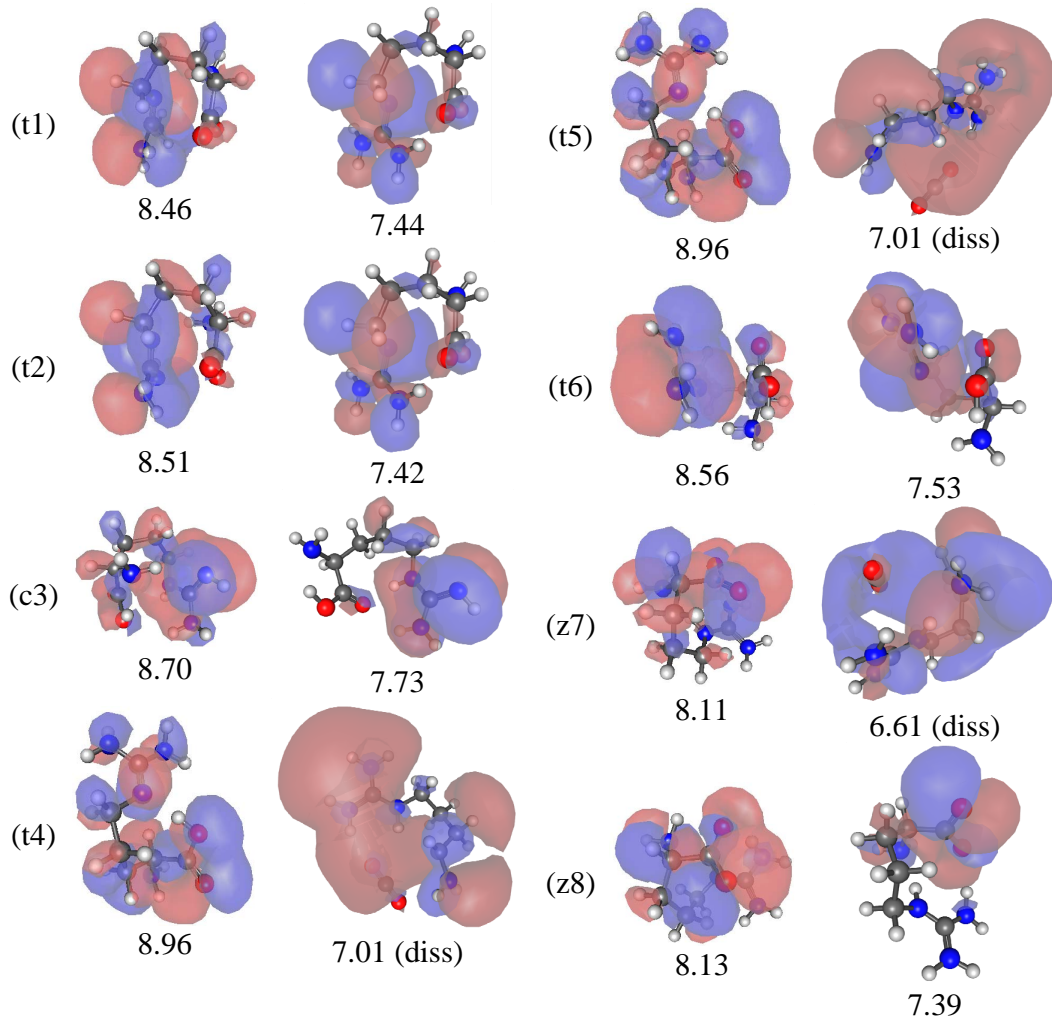


Figure 5.3: Energies and Dyson orbitals of different isomers of arginine at the Franck-Condon (left columns) and relaxed (right columns) structures.

carboxyl group. We note that the Dyson orbitals computed at the relaxed ionized structures are somewhat more localized compared to the Dyson orbitals computed at the initial (neutral) structures. Fig. 5.4 presents the computed stick spectra containing nine lowest VIEs and the lowest AIE for the isomers with a non-dissociative cationic state.

According to the AIMD simulations (carried out for a representative set of t1, c3, t4, and z8 isomers), imparting energy (1 eV, or 0.1 eV, or even 400 K) into the cationic

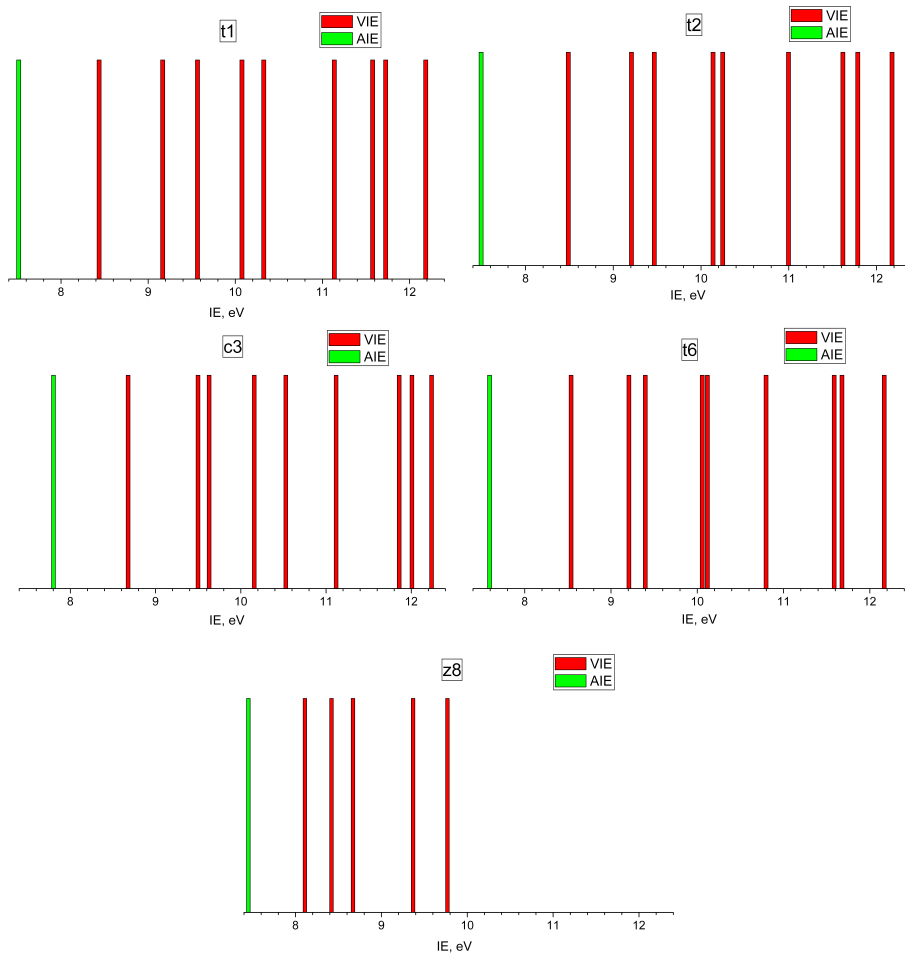


Figure 5.4: Stick spectra showing the lowest nine VIEs and the lowest AIE for t1, t2, c3, t6, and z8 isomers of arginine.

systems leads to a rapid dissociation on < 50 fs timescale. The resulting fragments are small, up to atoms, except for the lowest excess energy (400 K), at which for some canonical/tautomeric conformers we observed proton transfer to guanidine. The resulting zwitterionic structures underwent CO₂ abstraction – again, within 50 fs – and the resulting cations remained stable throughout the rest of the simulation, i.e., for about 10 ps.

To conclude, our calculations strongly suggest that ionization of arginine in the gas phase leads to rapid fragmentation and only a small yield of parent cation can be expected.

5.3.2 Effect of solvation

To gain an insight into effect of the solvent on ionization, we performed geometry optimizations at the ω B97X-D3/6-31++G(3df,2pd) level of theory with the CPCM description of solvent, in a similar manner as was done in the gas phase. The initial structures were optimized starting from the gas-phase geometries. The geometry optimization of the cations was performed starting from the Franck-Condon structures. The initial structures of solvated species remained similar to their gas-phase counterparts, but no dissociation was observed for the final cationic species, revealing that solvation introduces qualitative changes into the ionization process. The structures of most of the cations were similar to those of the corresponding neutral systems, but some converted to zwitterionic types. We observed two main scenarios: some isomers produced zwitterions with the guanidine group protonated, while others underwent proton transfer resulting in the protonated amino-group.

Prompted by this observation, we decided to consider an amino-zwitterion, in addition to the protonated structure, in the MD simulations of aqueous arginine. The amino-zwitterion was extensively tested to evaluate the effects of varying the size of the QM part (shown in Fig. 5.5), as well as to assess the performance of the implicit CPCM model and microsolvation in vacuum.

We found that having 6 or 7 explicit water molecules in QM yields similar VIEs. We note that, for the converged results, the solvation shell must include both donor- and acceptor-type hydrogen bonds with the solute, otherwise the description is imbalanced,

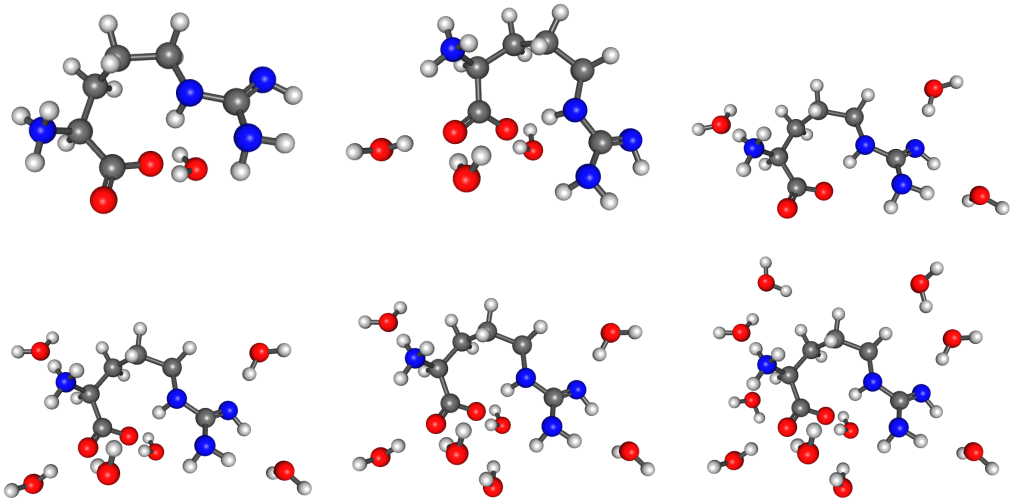


Figure 5.5: Arginine with closest hydrogen-bonded water molecules. Left to right: one closest water molecule, three donor water molecules near the carboxyl group, three acceptor water molecules – in the upper row; six (a combination of three donor and three acceptor) water molecules, seven (six and one closest), ten (seven and three closest) molecules – in the lower row.

leading to considerable discrepancies in VIEs computed with either 6, 7 or 0 water molecules in the QM region. Having 0 or 6/7 explicit water molecules does not introduce more than 0.2 eV difference in VIEs across all states, with a notable exception of state 9, where having only arginine in QM produces over 1 eV error. We note that this energy (around 12 eV) exceeds ionization energy of bulk water (11 eV¹⁷). Indeed, the analysis of Dyson orbitals for the 9th state (shown in Fig. 5.6) reveals a qualitative change upon adding water into QM and considerable contributions of water molecules, when they are available. Comparison with the Dyson orbitals for the first state, Fig. 5.7, confirms that this effect is specific only for some states. Consistently with no water contribution into the corresponding Dyson orbital, the lowest VIE changes within 0.1 eV for all considered sizes of the QM region.

Compared to the QM/MM result with 7 water molecules, PCM produces errors of up to 0.5 eV when only arginine is included into the QM part, with the exception of

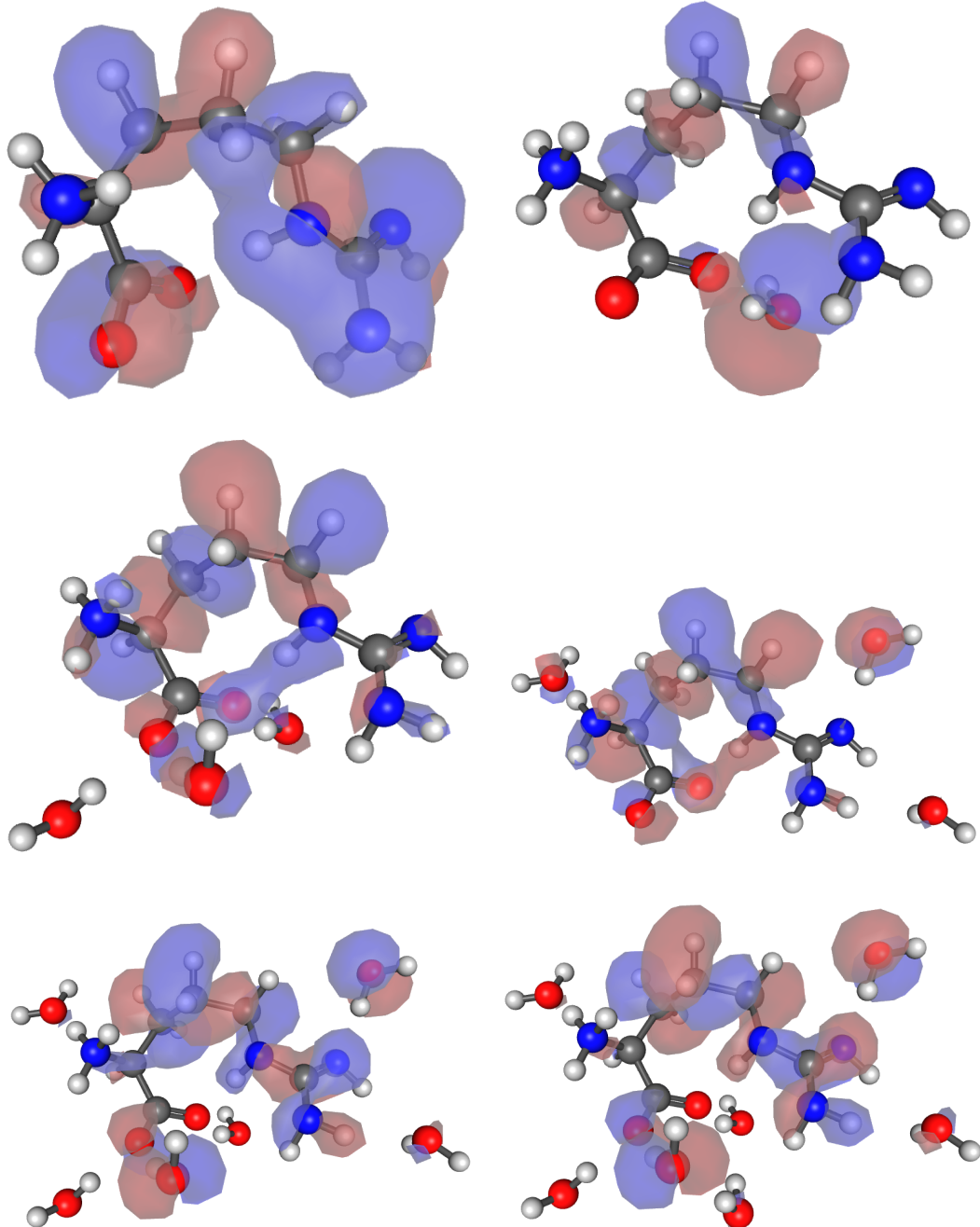


Figure 5.6: Dyson orbitals corresponding to the 9th ionized state computed at QM/MM level for arginine with different number of water molecules in QM.

the 1 eV deviation for the 9th state. Introducing explicit water molecules into the QM region improves the results, reducing errors to 0.4 eV. These observations agree with

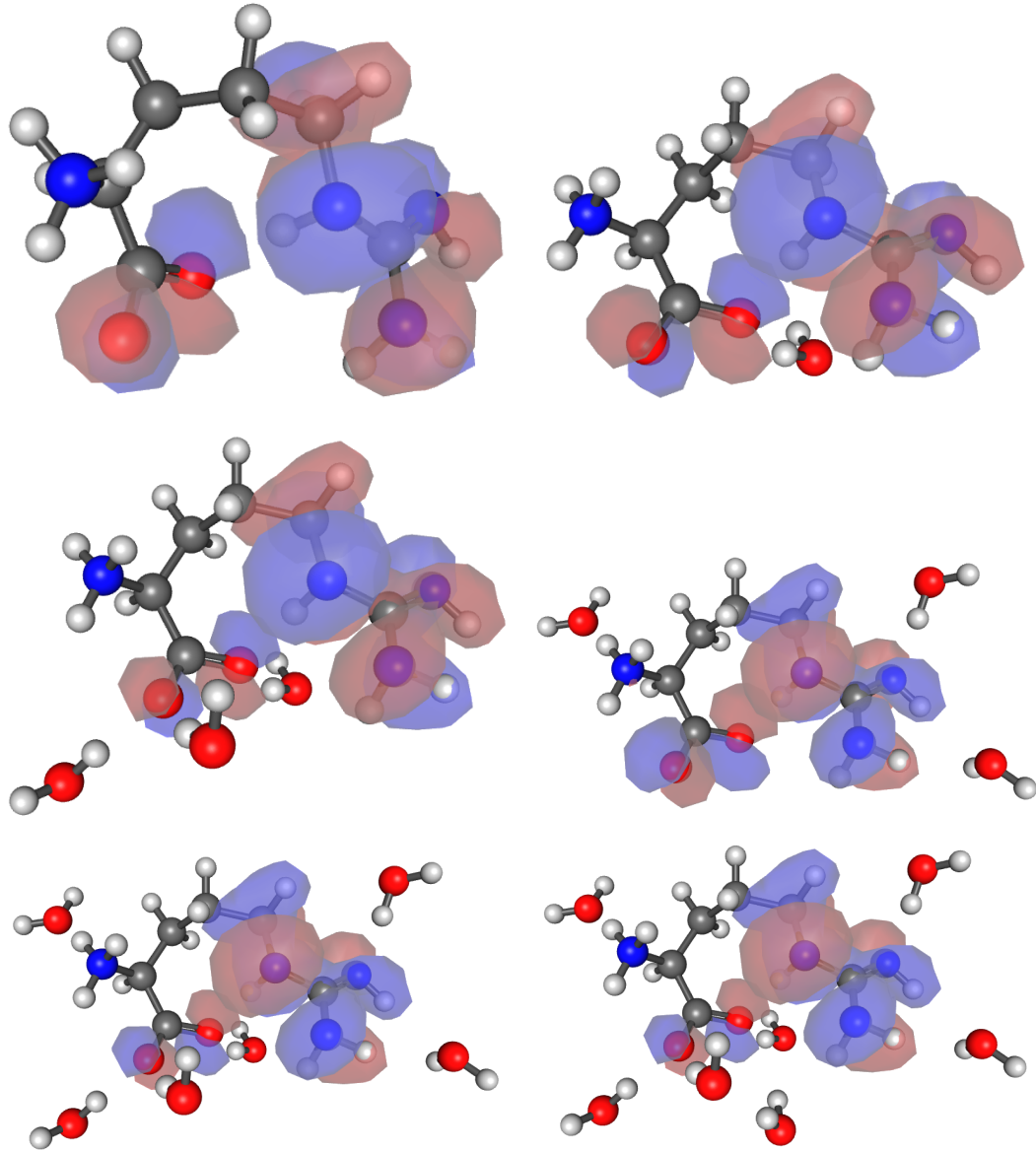


Figure 5.7: Dyson orbitals corresponding to the first ionized state computed at QM/MM level for arginine with different number of water molecules in QM.

conclusions in previous studies^{18–21} that PCM description of solvent leads to considerable errors for ionization energies.

In the gas phase, when no solvent molecules are included in the calculations, the VIEs differ by 0.5–1 eV from the QM/MM data, but microsolvation with 10 water

molecules brings the difference down to 0–0.5 eV. The comparison of the first Dyson orbital computed with QM/MM or QM/CPCM in solvent and QM only in vacuum for arginine with 7 water molecules is shown in Fig. 5.8. The orbitals look qualitatively similar, but adding solvent leads to some delocalization. We note that reference HF orbitals are considerably different, with Dyson orbitals containing 86% HOMO + 10% HOMO-1, 91% HOMO + 7% HOMO-1, 71% HOMO + 28% HOMO-1 within QM/MM, QM/CPCM, and QM only descriptions, respectively.

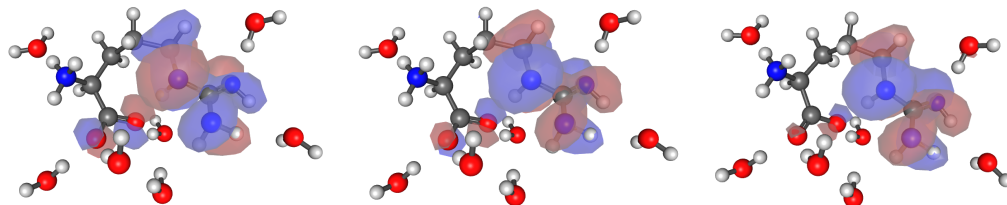


Figure 5.8: Dyson orbitals corresponding to the first ionized state of hydrated or micro-hydrated arginine with 7 water molecules. From left to right: QM/MM, QM/CPCM, QM only.

QM/MM VIEs of the 9 lowest ionized states averaged over 21 snapshots are shown in Fig. 5.9. The stick spectrum from the MD snapshots was convoluted with Gaussians 0.2 eV wide (typical resolution of synchrotron photon source). Since all transitions remain almost pure one-electron in the solvent, with the Dyson orbitals norms exceeding 0.9 in every case, we applied the same cross-section approximation and used unit height for every stick. Considerable broadening makes the lines overlap, such that the maximum of the resulting spectral line is shifted away from the averaged first IE. We expect some additional contributions from bulk water ionization to appear between states 8 and 9, but this would not affect the first peak. Despite different protonation states, the maxima of the first peak happen to be around 10 eV for both species. Protonated arginine, however, yields much narrower peak, such that the onsets differ by \sim 0.5 eV.

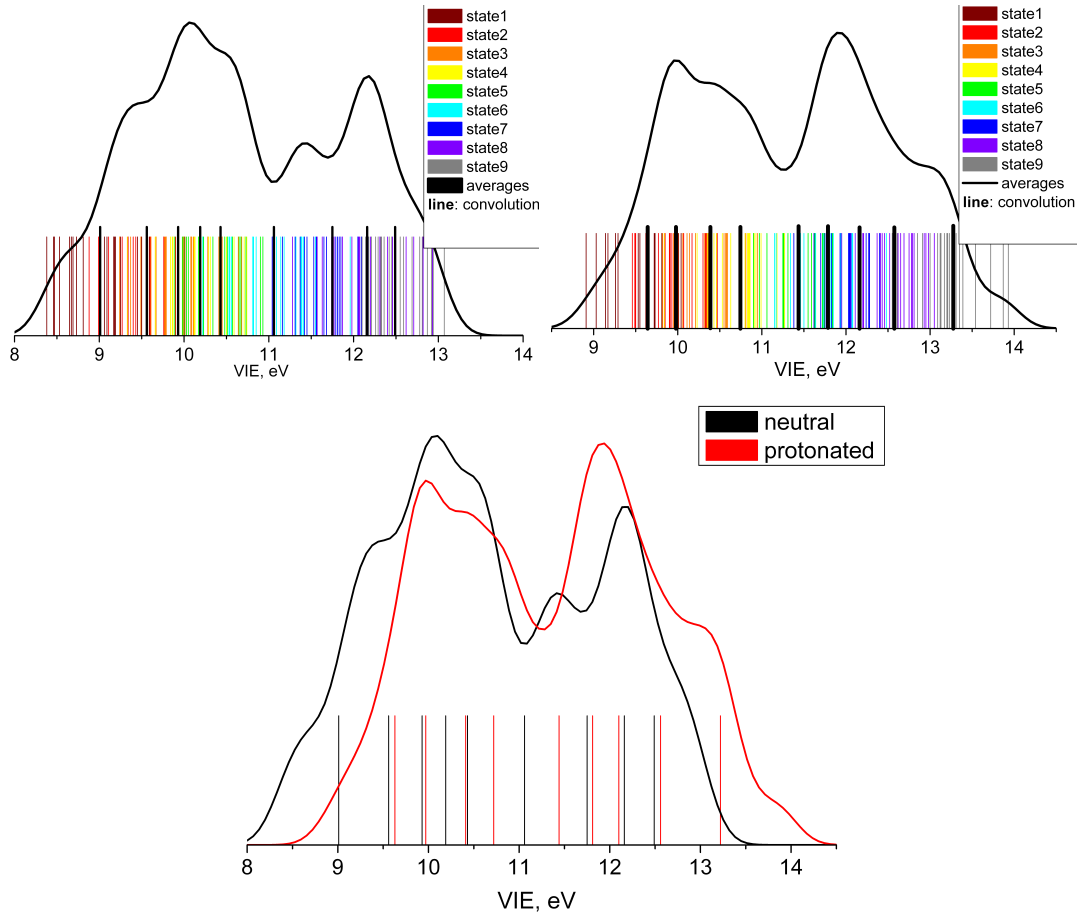


Figure 5.9: Computed photoelectron spectra of zwitterionic and protonated arginine in aqueous solution.

In sum, we observe that solvation: (i) suppresses the dissociative ionization and (ii) requires considering several ionized states due to close-lying IEs and considerable broadening.

5.4 Chapter 5 references

- [1] A.G. Harrison. The gas-phase basicities and proton affinities of amino acids and peptides. *Mass Spectrom. Rev.*, 16:201–217, 1997.
- [2] R. Aebersold and M. Mann. Mass spectrometry-based proteomics. *Nature*, 422:198–207, 2003.
- [3] Z. Meng, T.A. Simmons-Willis, and P.A. Limbach. The use of mass spectrometry in genomics. *Biomol. Eng.*, 21:1–13, 2004.
- [4] M. Oda and T. Nakayama. Electronic-state control of amino acids on semiconductor surfaces. *Appl. Surf. Sci.*, 244:627–630, 2005.
- [5] S. Campbell, J.L. Beauchamp, M. Rempe, and D.L. Lichtenberger. Correlations of lone pair ionization energies with proton affinities of amino acids and related compounds. Site specificity of protonation. *Int. J. Mass Spectrom.*, 117:83–99, 1992.
- [6] K.R. Wilson, L. Belau, C. Nicolas, M. Jimenez-Cruz, S.R. Leone, and M. Ahmed. Direct determination of the ionization energy of histidine with VUV synchrotron radiation. *Int. J. Mass Spectrom.*, 249–250:155–161, 2006.
- [7] S. Ling, W. Yu, Z. Huang, Z. Lin, M. Haranczyk, and M. Gutowski. Gaseous arginine conformers and their unique intramolecular interactions. *J. Phys. Chem. A*, 110:12282–12291, 2006.
- [8] J. Rak, P. Skurski, J. Simons, and M. Gutowski. Low-energy tautomers and conformers of neutral and protonated arginine. *J. Am. Chem. Soc.*, 123:11695–11707, 2001.
- [9] Y. Yuan, M. J. L. Mills, P. L. A. Popelier, and F. Jensen. Comprehensive analysis of energy minima of the 20 natural amino acids. *J. Phys. Chem. A*, 118:7876–7891, 2014.
- [10] P.J. Stephens, F.J. Devlin, C.F. Chabalowski, and M.J. Frisch. *Ab Initio* calculation of vibrational absorption and circular dichroism spectra using density functional force fields. *J. Phys. Chem.*, 98:11623–11627, 1994.
- [11] J.-D. Chai and M. Head-Gordon. Systematic optimization of long-range corrected hybrid density functionals. *J. Chem. Phys.*, 128:084106, 2008.

- [12] R. Chaudhuri, D. Mukhopadhyay, and D. Mukherjee. Applications of open-shell coupled cluster theory using an eigenvalue-independent partitioning technique: Approximate inclusion of triples in IP calculations. *Chem. Phys. Lett.*, 162:393, 1989.
- [13] J.F. Stanton and J. Gauss. Analytic energy derivatives for ionized states described by the equation-of-motion coupled cluster method. *J. Chem. Phys.*, 101(10):8938–8944, 1994.
- [14] A.I. Krylov. Equation-of-motion coupled-cluster methods for open-shell and electronically excited species: The hitchhiker’s guide to Fock space. *Annu. Rev. Phys. Chem.*, 59:433–462, 2008.
- [15] Shao, Y.; Gan, Z.; Epifanovsky, E.; Gilbert, A.T.B.; Wormit, M.; Kussmann, J.; Lange, A.W.; Behn, A.; Deng, J.; Feng, X., et al. Advances in molecular quantum chemistry contained in the Q-Chem 4 program package. *Mol. Phys.*, 113:184–215, 2015.
- [16] B. Hess, C. Kutzner, D. van der Spoel, and E. Lindahl. GROMACS 4: Algorithms for highly efficient, load-balanced, and scalable molecular simulation. *J. Chem. Theory Comput.*, 4:435–447, 2008.
- [17] S. Barth, M. Ončák, V. Ulrich, M. Mucke, T. Lischke, P. Slavíček, and U. Hergenhahn. Valence ionization of water clusters: From isolated molecules to bulk. *J. Phys. Chem. A*, 113:13519–13527, 2009.
- [18] B. Jagoda-Cwiklik, P. Slavíček, L. Cwiklik, D. Nolting, B. Winter, and P. Jungwirth. Ionization of imidazole in the gas phase, microhydrated environments, and in aqueous solution. *J. Phys. Chem. A*, 112:3499, 2008.
- [19] A.V. Marenich, C.J. Cramer, and D.G. Truhlar. Universal solvation model based on solute electron density and on a continuum model of the solvent defined by the bulk dielectric constant and atomic surface tensions. *J. Phys. Chem. B*, 113:6378–6396, 2009.
- [20] L. Sviatenko, O. Isayev, L. Gorb, F. Hill, and J. Lezczynski. Toward robust computational electrochemical predicting the environmental fate of organic pollutants. *J. Comput. Chem.*, 32:2195, 2011.
- [21] J. Zhang, H. Zhang, T. Wu, Q. Wang, and D. van der Spoel. Comparison of implicit and explicit solvent models for the calculation of solvation free energy in organic solvents. *J. Chem. Theory Comput.*, 2017. doi:10.1021/acs.jctc.7b00169.

Chapter 6: Future work

We derived and implemented the equation-of-motion coupled-cluster with single and double substitutions (EOM-CCSD) Dyson orbitals, which can be used for computing total and differential cross-sections and for assisting the interpretation of experimental studies. The research presented in this thesis opens many ways for expansion, in terms of both method development and studying solvation effects.

6.1 Method development: Electronic structure part, outgoing electron and experimental observables modeling, extension to time-resolved experiments

For electronic structure part of the problem, derivation and application of Dyson orbitals within EOM-MP2 formalism¹ would allow to reduce the scaling of the calculations from $O(N^6)$ to $O(N^5)$, while maintaining accuracy and simplicity of the formulation. As can be readily seen from the programmable expressions derived in Chapter 2, this will require implementing EOM-MP2 left vectors. Currently only EOM-CC left vectors are implemented, while EOM-MP2 left vectors for the reference state are not available². Such implementation will extend the size of the systems that can be tackled.

Another interesting line of research is to investigate the asymptotic behavior of EOM-CC Dyson orbitals computed using Gaussian-type basis sets (GTO). As was shown long ago³, the correct asymptotic behavior of the radial part is

$$\phi^d(r) \propto e^{-\alpha r}, \quad (6.1)$$

where α is related to the ionization energy, $\alpha = \sqrt{2 \cdot IE}$. However, the radial part of GTOs is defined as

$$\phi(r) = n(l, \beta) r^l e^{-\beta r^2}, \quad (6.2)$$

where n is normalization coefficient, specific for an angular momentum l . Thus, the asymptotic decay will follow $e^{-\beta_{diff} r^2}$, where β_{diff} is the exponent of the most diffuse GTO basis function. It would be interesting to determine at which r values (angular dependent in the case of molecules due to non-spherical symmetry) the performance deteriorates, and to connect it to basis-set size and diffuseness, as well as to assess the effect on the computed spectral properties. Even though we do not expect significant deterioration, since with the increase of r , the exponent decreases faster than a linear function (dipole moment operator \mathbf{r}), some improvement was observed⁴ for calculating β anisotropy parameters and total photoionization cross-sections when using Slater-type orbitals (which have correct asymptotic behavior) instead of GTOs in density functional theory (DFT).

In Chapter 3, it was shown that simple single-center expansion with physically meaningful single parameter Z enables modeling cross-sections for broad range of photon energies and very simple one-dimensional model was proposed for computing optimal Z from the first principles (i.e., without fitting to experimental results). This idea needs to be generalized and expanded to full dimensionality and any types of outgoing

waves. Furthermore, *ezDyson* can be expanded for computing experimental observables for autoionization or autodetachment processes, taking the extension of Dyson orbitals for metastable states⁵ within EOM-CC approach with complex absorbing potential (CAP) as an input. For this development, one needs to incorporate both real and imaginary parts of CAP-EOM Dyson orbitals. As metastable states play very important role in plasmas, atmospheric chemistry, and in extraterrestrial conditions, the results can be used to provide parameters for kinetic modeling of those processes. In particular, by application to stable and metastable, valence and dipole-bound anions relevant for interstellar space, this study can contribute towards resolving the puzzle of the diffuse interstellar bands^{6,7}.

Time-resolved photoelectron spectroscopy and imaging, TRPES and TRPEI^{8–12}, are sensitive to nuclear degrees of freedom of the systems, which means that their modeling needs to account for non-adiabatic dynamics. Currently, full dynamics at the EOM-CC level is not affordable beyond the smallest systems. It also requires implementation of the EOM-CC non-adiabatic couplings. Having EOM-MP2 Dyson orbitals would be very useful for these studies, too. MS-PT2 implementation¹³ suggests that at least within *ab initio* multiple spawning (AIMS) scheme the EOM treatment would be possible and, moreover, superior due a common set of the MOs for all states by construction. At the same time, EOM treatment at some snapshots can be used¹⁴ for benchmarking when selecting appropriate density functional, if time-dependent DFT, TD-DFT, happens to be electronic structure method of choice¹⁵. For instance, we have already shown in Chapter 4 that DFT self-interaction error has significant effect on orbitals and experimental spectroscopic properties of sodium-doped clusters in their ground electronic state.

6.2 Understanding solvent effects

There are numerous possibilities to expand studies of solvated electrons by, for example, considering different solvents, various dopants, or neat clusters. The methodology described in Chapter 2 would be especially useful and powerful for the following:

- characterizing excited states of solvated electrons by EOM-EA/EOM-EE (EOM-CC for electron attachment or excitation) Dyson orbitals (related to the experimental study of Gartmann *et. al.*¹⁶)
- describing multi-doped $M_k(NH_3)_n$ clusters by using EOM-EA/EOM-SF (EOM-CC for electron attachment or spin-flip) combination. Such clusters are interesting for understanding if bulk phase transition of the solvated electrons (reviewed in Ref. 150) exists at cluster level.

Although it is unclear whether direct TRPEI modeling would be affordable for the first problem, it would be very interesting to try. Alternatively, as discussed above in section 6.1, theory can contribute by providing information on vertical excitation energies and oscillator strengths of transitions to the lowest-lying excited states, as well as by providing photoelectron angular distributions (PADs) for these states as a reference for facilitating the interpretation of experimental results. For the second problem, even though we would not be able to model as large clusters as in the experimental studies¹⁷, we can directly visualize and discover trends for varying k , n , and metal M, as well as provide benchmarks for approximate treatments, as was done in Chapter 4.

One can develop a molecular-level insight into solvent effects on ionization by visualizing and comparing Dyson orbitals in the gas phase, in microsolvated clusters of various sizes, and in bulk water. One interesting model system would be phenol

and phenolate, whose photoionization/photodetachment was modeled¹⁸ at the EOM-IP-CCSD/EFP (effective fragment potential) level of theory. In that study aqueous photoionization and photodetachment spectra were successfully reproduced using the molecular dynamics (MD) snapshots, but the relative intensities were incorrect, possibly because of the same cross-section approximation. By comparing to the experimental gas-phase spectra^{19,20}, we notice a different trend in relative peak intensities, however, apart from having no solvent, the gas phase experiments are conducted at much lower photon energies, 21.2 and 3.5 eV for phenol and phenolate, respectively – compared to 200 eV in solution. Therefore, visualizing Dyson orbitals for different solvation states of phenol and phenolate (including microsolvation), followed by computing total cross-sections in a broad range of photon energies, will provide an insight into the underlying physics as well as allow one to test the validity of extrapolations from microhydration to bulk for total cross-sections. Additionally, we can evaluate applicability of the same cross-section approximation under different conditions.

Preliminary gas-phase and microsolvation results are shown in Fig. 6.1. These Dyson orbitals suggest that we should expect different behavior of the two species upon solvation, with anion being more sensitive. The next step would be to compute total cross-sections at different snapshots in solution, as was done in previous work¹⁸, and to incorporate them into the peak profiles. Since the computed cross-sections are absolute values in the atomic units²¹, we can directly compare the outcome with the experimental spectra. Similar procedure can be applied to gas-phase data at the corresponding experimental photon energies, combined with gas-phase MD snapshots to take temperature effect into account. Finally, cross-sections can be modeled for a broad photon energy range in different solvation states (no solvent, clusters, bulk) to discriminate between solvent effects and the role of experimental setup and to test if convergence to bulk

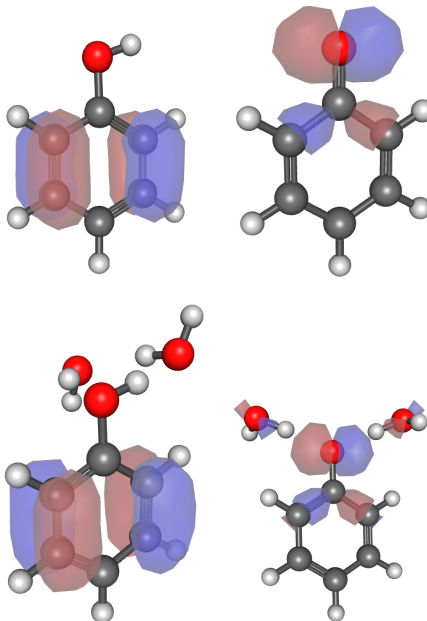


Figure 6.1: Second Dyson orbital for the bare (top) and doubly hydrated (bottom) phenol and phenolate.

with cluster size increase is observed. Visualizing the corresponding Dyson orbitals will allow one to visually connect the trends in the experimental observables with the underlying microscopic picture, and comparing Dyson orbitals' norms with the computed cross-sections will allow one to assess the validity of approximating cross-section by the norms in different regimes.

6.3 Scanning tunneling microscopy

While photoelectron imaging provides indirect observation of changes in wave functions upon photoionization via PADs, scanning tunneling microscopy (STM) is designed to directly obtain images of electron density, an example of which is shown in Fig. 6.2.

The observable quantity in microscopy experiments is the space- and frequency-resolved spectral density $N(\mathbf{r}, \omega)$, a many-body analogue of density of states $\rho(\mathbf{r}, \omega)$.

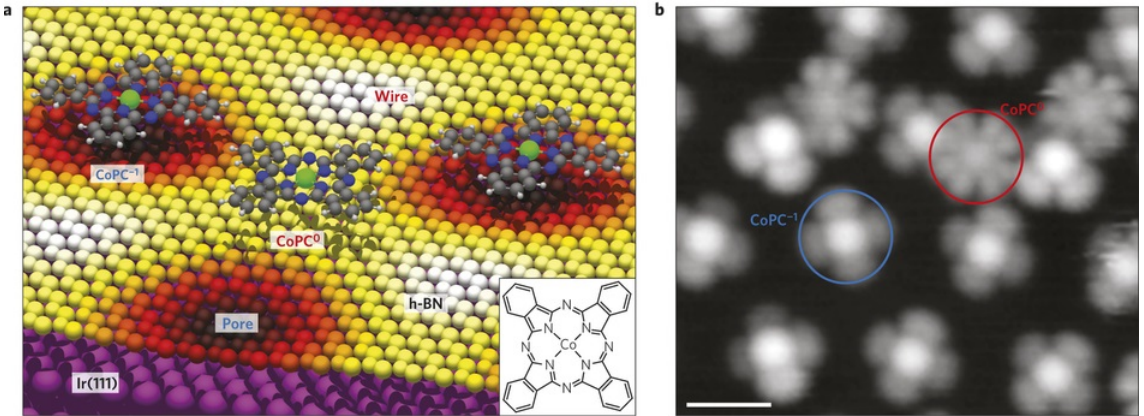


Figure 6.2: Cartoon (a) and STM image (b) of CoPC and its anions adsorbed on a h-BN monolayer on Ir(111). Inset in (a) shows the chemical structure of CoPC. Reprinted by permission from Macmillan Publishers Ltd: Nature Physics (Ref. 22), copyright 2015.

The STM images are usually analyzed in terms of the uncorrelated orbitals, which produces density of states (a recent molecular example can be found in Ref. 23). Toroz et. al.²⁴ went further and utilized many-body treatment, borrowing quasi-particle wave function (QPWF) description from solid state physics^{25,26}. When the tip is not included into the description, the quasi-particle here is of a hole type, “dressed” by the interaction with N electrons of the system:

$$N(\mathbf{r}, \omega) = \hbar \sum_i |\langle N-1, i | \hat{\Psi}(\mathbf{r}) | N, 0 \rangle|^2 \times \delta(\hbar\omega - E_0(N) + E_i(N-1)) \quad (6.3)$$

Here $|N, i\rangle$ is i -th excited state of an N -electron system with total energy $E_i(N)$; $i = 0$ represents ground state. In principle, the system comprises both the molecule and the substrate, but experiments can be designed to make molecule isolated electrically from the substrate by adding an insulating layer. In this case, one can focus on the molecule alone (only the effects of tunneling to or from substrate would be neglected).

Then in case of well-separated states with respect to the experimental resolution, i.e., by having $E_0(N) - E_i(N-1) > \hbar d\omega$, one obtains spectral density as the square modulus of hole-type QPWF:

$$N(\mathbf{r}, \omega) d\omega = |\langle N-1 | \hat{\Psi}(\mathbf{r}) | N \rangle|^2 = |hQWF(\mathbf{r})|^2 \quad (6.4)$$

Taking into account the form of Fermi field operator as a combination of contributions from basis orbitals, one can immediately see that $\hat{\Psi}(\mathbf{r}) = \sum_p \hat{a}_p \phi_p(\mathbf{r})$, Eq. (6.4) represents the Dyson orbital. That is, under certain conditions, the STM affords direct observation of spatially resolved molecular Dyson orbitals (squared). Toroz *et. al.*^{24,27} used primarily configuration interaction singles and doubles, CISD (which lacks size-extensivity), and, in limited cases, CCSD in order to include the effects of electron correlation into STM image modeling. In their calculations, for computational convenience the CI/CC coefficients for the neutral initial and for the final $N-1$ -electron states were computed using the same set of canonical HF orbitals of neutrals. Even such approximate treatment allowed them to predict²⁷ the case where correlation is expected to qualitatively change observed image.

Our approach for Dyson orbitals (Chapter 2) is more robust and naturally allows one to compare correlated and uncorrelated pictures directly from one calculation, simplifying analysis and prediction process. Furthermore, we can go beyond a simple model and contribute towards improvement of more complicated descriptions of STM images.

6.4 Chapter 6 references

- [1] J.F. Stanton and J. Gauss. Perturbative treatment of the similarity transformed Hamiltonian in equation-of-motion coupled-cluster approximations. *J. Chem. Phys.*, 103:1064–1076, 1995.
- [2] Q-Chem. Q-chem user’s manual (version 4.4), 2016.
http://www.q-chem.com/qchem-website/manual/qchem44_manual/index.html.
- [3] J. Katriel and E.R. Davidson. Asymptotic behavior of atomic and molecular wave functions. *Proc. Nat. Acad. Sci.*, 77(8):4403–4406, 1980.
- [4] Y. Lin and C. Ning. Calculation of photodetachment cross sections and photo-electron angular distributions of negative ions using density functional theory. *J. Chem. Phys.*, 143:144310, 2015.
- [5] T.-C. Jagau and A.I. Krylov. Characterizing metastable states beyond energies and lifetimes: Dyson orbitals and transition dipole moments. *J. Chem. Phys.*, 144:054113, 2016.
- [6] P.J. Sarre. The diffuse interstellar bands: a dipole-bound state hypothesis. *Mon. N. Roy. Astr. Soc.*, 313:L14–L16, 2000.
- [7] M. Tulej, D. A. Kirkwood, M. Pachkov, and J. P. Maier. Gas-phase electronic transitions of carbon chain anions coinciding with diffuse interstellar bands. *Astrophys. J. Lett.*, 506(1):L14–L16, 1998.
- [8] S. Ullrich, T. Schultz, M.Z. Zgierski, and A. Stolow. Electronic relaxation dynamics in DNA and RNA bases studied by time-resolved photoelectron spectroscopy. *Phys. Chem. Chem. Phys.*, 6:2796–2801, 2004.
- [9] D.M. Neumark. Time-resolved photoelectron spectroscopy of molecules and clusters. *Annu. Rev. Phys. Chem.*, 52:255–277, 2001.
- [10] A. Stolow, A.E. Bragg, and D.M. Neumark. Femtosecond time-resolved photo-electron spectroscopy. *Chem. Rev.*, 104:1719–1757, 2004.
- [11] T. Suzuki. Femtosecond time-resolved photoelectron imaging. *Annu. Rev. Phys. Chem.*, 57:555–592, 2006.
- [12] S. Lochbrunner, J.J. Larsen, J.P. Shaffer, M. Schmitt, T. Schultz, J.G. Underwood, and A. Stolow. Methods and applications of femtosecond time-resolved photo-electron spectroscopy. *J. Electron. Spectrosc. Relat. Phenom.*, 112(1-3):183–198, 2000.

- [13] T. Mori, W.J. Glover, M.S. Schuurman, and T.J. Martinez. Role of rydberg states in the photochemical dynamics of ethylene. *J. Phys. Chem. A*, 116:2808–2818, 2012.
- [14] A.O. Gunina and A.I. Krylov. Probing electronic wave functions of sodium-doped clusters: Dyson orbitals, anisotropy parameters, and ionization cross-sections. *J. Phys. Chem. A*, 120:9841–9856, 2016.
- [15] A. Humeniuk, M. Wohlgemuth, T. Suzuki, and R. Mitrić. Time-resolved photo-electron imaging spectra from non-adiabatic molecular dynamics simulations. *J. Chem. Phys.*, 139(13):134104, 2013.
- [16] T.E. Gartmann, B.L. Yoder, E. Chasovskikh, and R. Signorell. Lifetimes and energetics of the first electronically excited states of NaH₂O from time-resolved photoelectron imaging. *Chem. Phys. Lett.*, 2017. doi: 10.1016/j.cplett.2017.01.044.
- [17] S. Hartweg, A.H.C. West, B.L. Yoder, and R. Signorell. Metal transition in sodium-ammonia nanodroplets. *Angew. Chem. Int. Ed.*, 55:12347–12350, 2016.
- [18] D. Ghosh, A. Roy, R. Seidel, B. Winter, S. Bradforth, and A.I. Krylov. A first-principle protocol for calculating ionization energies and redox potentials of solvated molecules and ions: Theory and application to aqueous phenol and phenolate. *J. Phys. Chem. B*, 116:7269–7280, 2012.
- [19] T. P. Debies and J. W. Rabalais. Photoelectron spectra of substituted benzenes II. Seven valence electron substitution. *J. Elec. Spect. Rel. Phenomena*, 1:355, 1972.
- [20] R. F. Gunion, M. K. Gilles, M. L. Polak, and W. C. Lineberger. Ultraviolet photo-electron spectroscopy of the phenide, benzyl and phenoxide anions, with ab initio calculations. *Int. J. Mass Spectrom. Ion Proc.*, 117:601 – 620, 1992.
- [21] S. Gozem and A.I. Krylov. ezDyson user's manual, 2015.
ezDyson, <http://iopenshell.usc.edu/downloads/>.
- [22] F. Schulz, M. Ijas, R. Drost, S.K. Hamalainen, A. Harju, A.P. Seitsonen, and P. Liljeroth. Many-body transitions in a single molecule visualized by scanning tunnelling microscopy. *Nature Phys.*, 11:229–234, 2015.
- [23] J. Nieminen, E. Niemi, V. Simic-Milosevic, and K. Morgenstern. STM images and tunneling channels of substituted benzene molecules. *Phys. Rev. B*, 72:195421, 2005.
- [24] D. Toroz, M. Rontani, and S. Corni. Visualizing electron correlation by means of ab initio scanning tunneling spectroscopy images of single molecules. *J. Chem. Phys.*, 134:024104, 2011.

- [25] M. Rontani and E. Molinari. Imaging quasiparticle wave functions in quantum dots via tunneling spectroscopy. *Phys. Rev. B*, 71:233106, 2005.
- [26] M. Rontani and E. Molinari. Correlation effects in quantum dot wave function imaging. *Jap. J. Appl. Phys.*, 45(3B):1966–1969, 2006.
- [27] D. Toroz, M. Rontani, and S. Corni. Proposed alteration of images of molecular orbitals obtained using a scanning tunneling microscope as a probe of electron correlation. *Phys. Rev. Lett.*, 110:018305, 2013.

Bibliography

- R. Aebersold and M. Mann. *Nature*, 422:198–207, 2003.
- E. Alizadeh, T.M. Orlando, and L. Sanche. *Annu. Rev. Phys. Chem.*, 66:379, 2015.
- E. Alizadeh and L. Sanche. *Chem. Rev.*, 112:5578–5602, 2012.
- C.-O. Almbladh and U. von Barth. *Phys. Rev. B*, 31:3231–3244, 1985.
- C. Backx, G.R. Wight, and M.J. Van der Wiel. *J. Phys. B*, 9:315, 1976.
- M. T. Baeza-Romero, M. A. Blitz, A. Goddard, and P. W. Seakins. *Int. J. Chem. Kinet.*, 44:532–545, 2012.
- S. Barth, M. Ončák, V. Ulrich, M. Mucke, T. Lischke, P. Slavíček, and U. Hergenhahn. *J. Phys. Chem. A*, 113:13519–13527, 2009.
- R.J. Bartlett. *Annu. Rev. Phys. Chem.*, 32:359–401, 1981.
- R.J. Bartlett. *Int. J. Mol. Sci.*, 3:579–603, 2002.
- R.J. Bartlett. *Mol. Phys.*, 108:2905–2920, 2010.
- R.J. Bartlett. *WIREs Comput. Mol. Sci.*, 2(1):126–138, 2012.
- R.J. Bartlett and J.F. Stanton. *Rev. Comp. Chem.*, 5:65–169, 1994.
- L. Belau, K. R. Wilson, S. R. Leone, and M. Ahmed. *J. Phys. Chem. A*, 111:10075–10083, 2007.
- T. Best, R. Otto, S. Trippel, P. Hlavenka, A. von Zastrow, S. Eisenbach, S. Jezouin, R. Wester, E. Vigren, M. Hamberg, and W. D. Geppert. *Astrophys. J.*, 742:63, 2011.
- H.A. Bethe and E.E. Salpeter. *Quantum mechanics of one and two electron atoms*. Plenum, New York, 1977.
- D.M. Bishop. *Adv. Quantum Chem.*, 3:25–59, 1967.

- O. Bjorneholm, F. Federmann, S. Kakar, and T. Moller. *J. Chem. Phys.*, 111(2):546–550, 1999.
- M. A. Blitz, A. Goddard, T. Ingham, and M. J. Pilling. *Rev. Sci. Instrum.*, 78:034103, 2007.
- A. Bodi, P. Hemberger, D.L. Osborn, and B. Sztaray. *J. Phys. Chem. Lett.*, 4:2984–2952, 2013.
- F. Buchner, T. Schultz, and A. Lubcke. *Phys. Chem. Chem. Phys.*, 14:5837–5842, 2012.
- P. Burrow. P. Burrow, 2007.
<http://digitalcommons.unl.edu/physicsburrow/6/>.
- G.V. Buxton. G.V. Buxton. In M. Spotheim-Maurizot, M. Mostafavi, J. Belloni, and T. Douki, editors, *Radiation Chemistry: From Basics to Applications in Material and Life Sciences*, pages 3–16. EDP Sciences, 2008.
- I. Cacelli, R. Moccia, and A. Rizzo. *Phys. Rev. A*, 57:1895–1905, 1998.
- H.P. Cady. *J. Phys. Chem.*, 1:707–713, 1897.
- D. Caine. *Organic Reactions*, 23:1–258, 2011.
- S. Campbell, J.L. Beauchamp, M. Rempe, and D.L. Lichtenberger. *Int. J. Mass Spectrom.*, 117:83–99, 1992.
- A.W. Castleman and K.H. Bowen. *J. Phys. Chem.*, 100:12911–12944, 1996.
- J.-D. Chai and M. Head-Gordon. *Phys. Chem. Chem. Phys.*, 10:6615–6620, 2008.
- J.-D. Chai and M. Head-Gordon. *J. Chem. Phys.*, 128:084106, 2008.
- D.W. Chandler and P.L. Houston. *Annu. Rev. Phys. Chem.*, 87:1445–1447, 1987.
- R. Chaudhuri, D. Mukhopadhyay, and D. Mukherjee. *Chem. Phys. Lett.*, 162:393, 1989.
- X. Chu. *Phys. Rev. A*, 82:023407, 2010.
- J. Cizek. *J. Chem. Phys.*, 45:4256–4266, 1966.
- T.A. Cool, J. Wang, K. Nakajima, C.A. Taatjes, and A. McIlroy. *Int. J. Mol. Sci.*, 247:18–27, 2005.
- J. Cooper and R.N. Zare. *J. Chem. Phys.*, 48:942–943, 1968.

- J.W. Cooper. *Phys. Rev.*, 128:681–693, 1962.
- H.H. Corzo and J.V. Ortiz. *Adv. Quantum Chem.*, 74:267–298, 2017.
- M. Cossi, N. Rega, G. Scalmani, and V. Barone. *J. Comput. Chem.*, 24:669–681, 2003.
- C. J. Cramer and D. G. Truhlar. *Acc. Chem. Res.*, 42:489–492, 2009.
- C.J. Cramer and D.G. Truhlar. *Chem. Rev.*, 99:2161, 1999.
- J. Cukras, S. Coriani, P. Decleva, O. Christiansen, and P. Norman. *J. Chem. Phys.*, 139:094103, 2013.
- J. Cukras, P. Decleva, and S. Coriani. *J. Chem. Phys.*, 141:174315, 2014.
- T. P. Debies and J. W. Rabalais. *J. Elec. Spect. Rel. Phenomena*, 1:355, 1972.
- P.V. Demekhin, A. Ehresmann, and V.L. Sukhorukov. *J. Chem. Phys.*, 134:024113, 2011.
- L.G. Dodson, L. Shen, J.D. Savee, N.C. Eddingsaas, O. Welz, C.A. Taatjes, D.L. Osborn, S.P. Sander, and M. Okumura. *J. Phys. Chem. A*, 119:1279–1291, 2015.
- F. Dong, S. Heinbuch, J. J. Rocca, and E. R. Bernstein. *J. Chem. Phys.*, 124(22):224319, 2006.
- A. Dreuw and M. Wormit. *WIREs Comput. Mol. Sci.*, 5:82–95, 2015.
- I. Duchemin, D. Jacquemin, and X. Blase. *J. Chem. Phys.*, 144:164106, 2016.
- O.T. Ehrler and D.M. Neumark. *Acc. Chem. Res.*, 42:769, 2009.
- A. J. Eskola and R. S. Timonen. *Phys. Chem. Chem. Phys.*, 5:2557–2561, 2003.
- J.P. Farrel, L.S. Spector, B.K. McFarland, P.H. Bucksbaum, M. Gühr, M.B. Gaarde, and K.J. Schafer. *Phys. Rev. A*, 83:023420, 2011.
- M. Faubel, K. R. Siefermann, Y. Liu, and B. Abel. *Acc. Chem. Res.*, 45:120–130, 2012.
- R.F. Fink, M.N. Piancastelli, A.N. Grum-Grzhimailo, and K. Ueda. *J. Chem. Phys.*, 130:014306, 2009.
- C. Fockenberg, H. J. Bernstein, G. E. Hall, J. T. Muckerman, J. M. Preses, T. J. Sears, and R. E. Weston. *Rev. Sci. Instrum.*, 70:3259–3264, 1999.

- G. Fronzoni, M. Stener, and P. Decleva. *Chem. Phys.*, 298:141–153, 2004.
- B.C. Garrett, D.A. Dixon, D.M. Camaioni, D.M. Chipman, M.A. Johnson, C.D. Jonah, G.A. Kimmel, J.H. Miller, T.N. Rescigno, P.J. Rossky, S.S. Xantheas, S.D. Colson, A.H. Laufer, D. Ray, P.F. Barbara, D.M. Bartels, K.H. Becker, H. Bowen, S.E. Bradforth, I. Carmichael, J.V. Coe, L.R. Corrales, J.P. Cowin, M. Dupuis, K.B. Eisenthal, J.A. Franz, M.S. Gutowski, K.D. Jordan, B.D. Kay, J.A. LaVerne JA, S.V. Lymar, T.E. Madey, C.W. McCurdy, D. Meisel, S. Mukamel, A.R. Nilsson, T.M. Orlando, N.G. Petrik, S.M. Pimblott, J.R. Rustad, G.K. Schenter, S.J. Singer, A. Tokmakoff, L.S. Wang, C. Wittig, and T.S. Zwier. *Chem. Rev.*, 105:355–389, 2005.
- T.E. Gartmann, B.L. Yoder, E. Chasovskikh, and R. Signorell. *Chem. Phys. Lett.*, 2017. doi: 10.1016/j.cplett.2017.01.044.
- D. Ghosh. *J. Phys. Chem. A*, 121:741–752, 2017.
- D. Ghosh, O. Isayev, L.V. Slipchenko, and A.I. Krylov. *J. Phys. Chem. A*, 115:6028–6038, 2011.
- D. Ghosh, A. Roy, R. Seidel, B. Winter, S. Bradforth, and A.I. Krylov. *J. Phys. Chem. B*, 116:7269–7280, 2012.
- D.M. Gingrich. *Practical Quantum Electrodynamics*. CRC Press, 2006.
- M. Goldmann, J. Miguel-Sanchez, A. H. C. West, B. L. Yoder, and R. Signorell. *J. Chem. Phys.*, 142:224304, 2015.
- H. Gomez, G. Meloni, J. Madrid, and D. M. Neumark. *J. Chem. Phys.*, 119:872–879, 2003.
- M.S. Gordon, D.G. Fedorov, S.R. Pruitt, and L.V. Slipchenko. *Chem. Rev.*, 112:632–672, 2012.
- M.S. Gordon, M.A. Freitag, P. Bandyopadhyay, J.H. Jensen, V. Kairys, and W.J. Stevens. *J. Phys. Chem. A*, 105:293–307, 2001.
- M.S. Gordon, L. Slipchenko, H. Li, and J.H. Jensen. M.S. Gordon, L. Slipchenko, H. Li, and J.H. Jensen. In D.C. Spellmeyer and R. Wheeler, editors, *Annual Reports in Computational Chemistry*, volume 3, pages 177–193. Elsevier, 2007. ISSN 1574-1400. URL <http://www.sciencedirect.com/science/article/B7RNN-4PPMX91-D/2/247d166fda2e8f52be7f7e96dfe33ffd>.
- S. Gozem, A.O. Gunina, T. Ichino, D.L. Osborn, J.F. Stanton, and A.I. Krylov. *J. Phys. Chem. Lett.*, 6:4532–4540, 2015.
- S. Gozem and A.I. Krylov. S. Gozem and A.I. Krylov, 2015.

- ezDyson, <http://iopenshell.usc.edu/downloads/>.
- J. Gu, J. Leszczynski, and H. F.Schaefer III. *Chem. Rev.*, 112:5603–5640, 2012.
- A.O. Gunina and A.I. Krylov. *J. Phys. Chem. A*, 120:9841–9856, 2016.
- R. F. Gunion, M. K. Gilles, M. L. Polak, and W. C. Lineberger. *Int. J. Mass Spectrom. Ion Proc.*, 117:601 – 620, 1992.
- S. Han and D.R. Yarkony. *J. Chem. Phys.*, 133:194107, 2010.
- S. Han and D.R. Yarkony. *J. Chem. Phys.*, 134:174104, 2011.
- S. Han and D.R. Yarkony. *J. Chem. Phys.*, 134:134110, 2011.
- S. Han and D.R. Yarkony. *Mol. Phys.*, 110:845–859, 2012.
- A.G. Harrison. *Mass Spectrom. Rev.*, 16:201–217, 1997.
- S. Hartweg, A.H.C. West, B.L. Yoder, and R. Signorell. *Angew. Chem. Int. Ed.*, 55: 12347–12350, 2016.
- S. Hartweg, B.L. Yoder, G.A. Garcia, L. Nahon, and R. Signorell. *Phys. Rev. Lett.*, 2017. doi: arXiv:1612.02338.
- K. Hashimoto and K. Daigoku. *Chem. Phys. Lett.*, 469:62–67, 2009.
- A.J.R. Heck and D.W. Chandler. *Annu. Rev. Phys. Chem.*, 46:335–372, 1995.
- T. Helgaker, M. Jaszunski, and K. Ruud. *Chem. Rev.*, 99:293–352, 1999.
- T. Helgaker, P. Jørgensen, and J. Olsen. *Molecular electronic structure theory*. Wiley & Sons, 2000.
- J. M. Herbert. *Rev. Comp. Chem.*, 28:391–517, 2015.
- J. M. Herbert and M. P. Coons. *Annu. Rev. Phys. Chem.*, 68, 2017. doi: 10.1146/annurev-physchem-052516-050816.
- J.M. Herbert and L.D. Jacobson. *Int. Rev. Phys. Chem.*, 30:1–48, 2010.
- B. Hess, C. Kutzner, D. van der Spoel, and E. Lindahl. *J. Chem. Theory Comput.*, 4: 435–447, 2008.
- P.L. Houston. *Acc. Chem. Res.*, 28:453–460, 1995.
- H.R. Hudock, B.G. Levine, A.L. Thompson, H. Satzger, D. Townsend, N. Gador, S. Ulrich, A. Stolow, and T.J. Martínez. *J. Phys. Chem. A*, 111:8500–8598, 2007.

- A. Humeniuk, M. Wohlgemuth, T. Suzuki, and R. Mitrić. *J. Chem. Phys.*, 139(13):134104, 2013.
- V. Simic-Milosevic J. Nieminen, E. Niemi and K. Morgenstern. *Phys. Rev. B*, 72:195421, 2005.
- L.D. Jacobson and J. M. Herbert. *J. Am. Chem. Soc.*, 133:19889–19899, 2011.
- T.-C. Jagau and A.I. Krylov. *J. Chem. Phys.*, 144:054113, 2016.
- T.-C. Jagau, D. Zuev, K.B. Bravaya, E. Epifanovsky, and A.I. Krylov. *J. Phys. Chem. Lett.*, 5:310–315, 2014.
- B. Jagoda-Cwiklik, P. Slaviček, L. Cwiklik, D. Nolting, B. Winter, and P. Jungwirth. *J. Phys. Chem. A*, 112:3499, 2008.
- K. D. Jordan and P. D. Burrow. *Chem. Rev.*, 87(3):557–588, 1987.
- H.J. Kaiser, E. Heinicke, R. Rackwitz, and D. Feldmann. *Z. Phys.*, 270:259–265, 1974.
- A. Kammrath, J. R. R. Verlet, G.B. Griffin, and D. M. Neumark. *J. Chem. Phys.*, 125:171102, 2006.
- J. Katriel and E.R. Davidson. *Proc. Nat. Acad. Sci.*, 77(8):4403–4406, 1980.
- J. Kessler, M. Dracinsky, and P. Bour. *J. Comput. Chem.*, 34:366–371, 2013.
- K. Khistyayev, K.B. Bravaya, E. Kamarchik, O. Kostko, M. Ahmed, and A.I. Krylov. *Faraday Discuss.*, 150:313–330, 2011.
- D. Khuseynov, C.C. Blackstone, L.M. Culberson, and A. Sanov. *J. Chem. Phys.*, 141:124312, 2014.
- C.A. Kraus. *J. Am. Chem. Soc.*, 30:1323–1344, 1908.
- A.I. Krylov. *Acc. Chem. Res.*, 39:83–91, 2006.
- A.I. Krylov. *Annu. Rev. Phys. Chem.*, 59:433–462, 2008.
- A.I. Krylov and P.M.W. Gill. *WIREs Comput. Mol. Sci.*, 3:317–326, 2013.
- S. S. Kumar, D. Hauser, R. Jindra, T. Best, S. Roucka, W. D. Geppert, T. J. Millar, and R. Wester. *Astrophys. J.*, 776:25, 2013.
- L.D. Landau and E.M. Lifshitz. *Quantum Mechanics: Non-relativistic theory*. Pergamon, Oxford, 1977.

- A.W. Lange and J.M. Herbert. *J. Phys. Chem. Lett.*, 1:556–561, 2009.
- P.W. Langhoff. P.W. Langhoff. In V. McKoy T. Rescigno and B. Schneider, editors, *Electron Molecule and Photon Molecule Collisions*, pages 183–224. Plenum, New York, 1979.
- D. J. Larson, C. J. Edge, R. E. Elmquist, N. B. Mansour, , and R. Trainham. *Phys. Scr.*, T22:183–190, 1988.
- S.V. Levchenko and A.I. Krylov. *J. Chem. Phys.*, 120(1):175–185, 2004.
- M. Levy, J.P. Perdew, and V. Sahni. *Phys. Rev. A*, 30:2745–2748, 1984.
- F. Libisch, C. Huang, and E. A. Carter. *Acc. Chem. Res.*, 47:2768–2775, 2014.
- Y. Lin and C. Ning. *J. Chem. Phys.*, 143:144310, 2015.
- J. Linderberg and Y. Öhrn. *Propagators in quantum chemistry*. Academic, London, 1973.
- S. Ling, W. Yu, Z. Huang, Z. Lin, M. Haranczyk, and M. Gutowski. *J. Phys. Chem. A*, 110:12282–12291, 2006.
- J. H. Litman, B. L. Yoder, B. Schlappi, and R. Signorell. *Phys. Chem. Chem. Phys.*, 15:940–949, 2013.
- S. Lochbrunner, J.J. Larsen, J.P. Shaffer, M. Schmitt, T. Schultz, J.G. Underwood, and A. Stolow. *J. Electron. Spectrosc. Relat. Phenom.*, 112(1-3):183–198, 2000.
- J.F. Lockyear, O. Welz, J.D. Savee, F. Goulay, A.J. Trevitt, C.A. Taatjes, D.L. Osborn, and S.R. Leone. *J. Phys. Chem. A*, 11013-11026, 2013.
- A. Lubcke, F. Buchner, N. Heine, I. V. Hertel, and T. Schultz. *Phys. Chem. Chem. Phys.*, 12:14629–14634, 2010.
- R.R. Lucchese, K. Takatsuka, and V. McKoy. *Phys. Rep.*, 131(3):147–221, 1986.
- R. Mabbs, E. Surber, and A. Sanov. *J. Chem. Phys.*, 122:054308, 2005.
- A.V. Marenich, C.J. Cramer, and D.G. Truhlar. *J. Phys. Chem. B*, 113:6378–6396, 2009.
- A. R. McKay, M. E. Sanz, C. R. S. Mooney, R. S. Minns, E. M. Gill, and H. H. Fielding. *Rev. Sci. Instrum.*, 81:123101, 2010.
- Z. Meng, T.A. Simmons-Willis, and P.A. Limbach. *Biomol. Eng.*, 21:1–13, 2004.

- M. Mitsui, N. Ando, S. Kokubo, A. Nakajima, and K. Kaya. *Phys. Rev. Lett.*, 91: 153002, 2003.
- T. Mori, W.J. Glover, M.S. Schuurman, and T.J. Martinez. *J. Phys. Chem. A*, 116: 2808–2818, 2012.
- M. Mostafavi and I. Lampre. M. Mostafavi and I. Lampre. In M. Spotheim-Maurizot, M. Mostafavi, J. Belloni, and T. Douki, editors, *Radiation Chemistry: From Basics to Applications in Material and Life Sciences*, pages 33–52. EDP Sciences, 2008.
- V.A. Mozhayskiy and A.I. Krylov. V.A. Mozhayskiy and A.I. Krylov. ezSpectrum, <http://iopenshell.usc.edu/downloads/>.
- M. Musiał and R. J. Bartlett. *Rev. Mod. Phys.*, 79:291, 2007.
- A.P.P. Natalense and R. R. Lucchese. *J. Chem. Phys.*, 111:5344, 1999.
- D.M. Neumark. *Annu. Rev. Phys. Chem.*, 52:255–277, 2001.
- D.M. Neumark. *Phys. Chem. Chem. Phys.*, 7:433, 2005.
- D.M. Neumark. *J. Chem. Phys.*, 125:132303, 2006.
- C.M. Oana and A.I. Krylov. *J. Chem. Phys.*, 127:234106, 2007.
- C.M. Oana and A.I. Krylov. *J. Chem. Phys.*, 131:124114, 2009.
- M. Oda and T. Nakayama. *Appl. Surf. Sci.*, 244:627–630, 2005.
- J.V. Ortiz. *Adv. Quantum Chem.*, 35:33–52, 1999.
- P.A. Pieniazek, S.A. Arnstein, S.E. Bradforth, A.I. Krylov, and C.D. Sherrill. *J. Chem. Phys.*, 127:164110, 2007.
- E. Pluhařová, P. Jungwirth, S. E. Bradforth, and P. Slavíček. *J. Phys. Chem. B*, 115: 1294, 2011.
- E. Pluhařová, P. Slavíček, and P. Jungwirth. *Acc. Chem. Res.*, 48:1209–1217, 2015.
- G.D. Purvis and R.J. Bartlett. *J. Chem. Phys.*, 76:1910–1918, 1982.
- Q-Chem. Q-Chem, 2016.
http://www.q-chem.com/qchem-website/manual/qchem44_manual/index.html.
- J.W. Rabalais. *Principles of UltraViolet Photoelectron Spectroscopy*. John Wiley and Sons: New York, 1977.

- J. Rak, P. Skurski, J. Simons, and M. Gutowski. *J. Am. Chem. Soc.*, 123:11695–11707, 2001.
- K.J. Reed, A.H. Zimmerman, H.C. Andersen, and J.I. Brauman. *J. Chem. Phys.*, 64:1368–1375, 1976.
- K.L. Reid. *Int. Rev. Phys. Chem.*, 27:607–628, 2008.
- H. Reisler and A.I. Krylov. *Int. Rev. Phys. Chem.*, 28:267–308, 2009.
- N. Rohringer, A. Gordon, and R. Santra. *Phys. Rev. A*, 74(4):043420, 2006.
- M. Rontani and E. Molinari. *Phys. Rev. B*, 71:233106, 2005.
- M. Rontani and E. Molinari. *Jap. J. Appl. Phys.*, 45(3B):1966–1969, 2006.
- M. Ruberti, V. Averbukh, and P. Decleva. *J. Chem. Phys.*, 141:164126, 2014.
- M. Ruberti, R. Yun, K. Gokhberg, S. Kopelke, L.S. Cederbaum, F. Tarantelli, and V. Averbukh. *J. Chem. Phys.*, 139:144107, 2013.
- M. Ruckenbauer, S. Mai, P. Marquetand, and L. González. *Sci. Rep.*, 6:35522, 2016.
- J.J. Sakurai. *Modern Quantum Mechanics*. Addison-Wesley Publishing Company, 1995.
- J.A.R. Samson and W.C. Stolte. *J. Electron. Spectrosc. Relat. Phenom.*, 123:265–276, 2002.
- A. Sanov. *Annu. Rev. Phys. Chem.*, 65:341–363, 2014.
- A. Sanov and R. Mabbs. *Int. Rev. Phys. Chem.*, 27:53–85, 2008.
- P.J. Sarre. *Mon. N. Roy. Astr. Soc.*, 313:L14–L16, 2000.
- F. Schulz, M. Ijas, R. Drost, S.K. Hamalainen, A. Harju, A.P. Seitsonen, and P. Liljeroth. *Nat. Phys.*, 11:229–234, 2015.
- G.M. Seabra, I. G. Kaplan, and J. V. Ortiz. *J. Chem. Phys.*, 123:114105, 2005.
- G.M. Seabra, I. G. Kaplan, V. G. Zakrzewski, and J. V. Ortiz. *J. Chem. Phys.*, 121:4143–4155, 2004.
- R. Seidel, B. Winter, and S.E. Bradforth. *Annu. Rev. Phys. Chem.*, 67:283–305, 2006.
- H.M. Senn and W. Thiel. *Angew. Chem. Int. Ed.*, 48:1198–1229, 2009.

- Shao, Y.; Gan, Z.; Epifanovsky, E.; Gilbert, A.T.B.; Wormit, M.; Kussmann, J.; Lange, A.W.; Behn, A.; Deng, J.; Feng, X., et al. *Mol. Phys.*, 113:184–215, 2015.
- A. T. Shreve, T. A. Yen, and D. M. Neumark. *Chem. Phys. Lett.*, 493:216–219, 2010.
- K. R. Siefermann, Y. Liu, E. Lugovoy, O. Link, M. Faubel, U. Buck, B. Winter, and B. Abel. *Nat. Chem.*, 2:274–279, 2010.
- H. Siegbahn, L. Asplund, and P. Kelfve. *Chem. Phys. Lett.*, 35:330–335, 1975.
- R. Signorell, M. Goldmann, B. L. Yoder, A. Bodi, E. Chasovskikh, L. Lang, and D. Luckhaus. *Chem. Phys. Lett.*, 658:1–6, 2016.
- R. Signorell, B.L. Yoder, A.H.C. West, J.J. Ferreiro, and C.-M. Saak. *Chem. Science*, 5:12831295, 2014.
- J. Simons. In C.Y. Ng, editor, *Photoionization and Photodetachment*, volume 10, Part II of *Advanced Series in Physical Chemistry*. World Scientific Publishing Co., Singapore, 2000.
- J. Simons. *Annu. Rev. Phys. Chem.*, 62:107–128, 2011.
- I. R. Slagle and D. Gutman. *J. Am. Chem. Soc.*, 107:5342–5347, 1985.
- I. R. Slagle, F. Yamada, and D. Gutman. *J. Am. Chem. Soc.*, 103:149–153, 1981.
- P. Slavíček, B. Winter, M. Faubel, S.E. Bradforth, and P. Jungwirth. *J. Am. Chem. Soc.*, 131:6460–6467, 2009.
- L.V. Slipchenko. *J. Phys. Chem. A*, 114:8824–8830, 2010.
- D. Smidova, J. Lengyel, A. Pysanenko, J. Med, P. Slavicek, and M. Farnik. *J. Phys. Chem. Lett.*, 6:2865–2869, 2015.
- S.J. Smith and D.S. Burch. *Phys. Rev.*, 116:1125–1131, 1959.
- K.C. Smyth and J.I. Brauman. *J. Chem. Phys.*, 56:4620–4625, 1972.
- K. Sneskov and O. Christiansen. *WIREs Comput. Mol. Sci.*, 2:566, 2012.
- K. Sneskov, T. Schwabe, J. Kongsted, and O. Christiansen. *J. Chem. Phys.*, 134:104108, 2011.
- J.F. Stanton and J. Gauss. *J. Chem. Phys.*, 101(10):8938–8944, 1994.
- J.F. Stanton and J. Gauss. *J. Chem. Phys.*, 103:1064–1076, 1995.

- J.F. Stanton and J. Gauss. *J. Chem. Phys.*, 111:8785–8788, 1999.
- P.J. Stephens, F.J. Devlin, C.F. Chabalowski, and M.J. Frisch. *J. Phys. Chem.*, 98: 11623–11627, 1994.
- A. Stolow, A.E. Bragg, and D.M. Neumark. *Chem. Rev.*, 104:1719–1757, 2004.
- M. Strajbl, G. Hong, and A. Warshel. *J. Phys. Chem. B*, 106:13333–13343, 2002.
- Q. Sun and G. K.-L. Chan. *Acc. Chem. Res.*, 49:2705–2712, 2016.
- E. Surber, R. Mabbs, and A. Sanov. *J. Phys. Chem. A*, 107:8215–8224, 2003.
- T. Suzuki. *Annu. Rev. Phys. Chem.*, 57:555–592, 2006.
- T. Suzuki. *Int. Rev. Phys. Chem.*, 31:265–318, 2012.
- L. Sviatenko, O. Isayev, L. Gorb, F. Hill, and J. Lezczynski. *J. Comput. Chem.*, 32: 2195, 2011.
- K.H. Tan, C.E. Brion, P.E. Van Der Leeuw, and M.J. Van der Wiel. *Chem. Phys.*, 29: 299–309, 1978.
- Y. Tang, H. Shen, K. Sekiguchi, N. Kurahashi, T. Mizuno, Y. I. Suzuki, and T. Suzuki. *Phys. Chem. Chem. Phys.*, 12:3653–3655, 2010.
- S. Thürmer, R. Seidel, M. Faubel, W. Eberhardt, J.C. Hemminger, S.E. Bradforth, and B. Winter. *Phys. Rev. Lett.*, 111:173005, 2013.
- R. S. Timonen, E. Ratajczak, D. Gutman, and A. F. Wagner. *J. Phys. Chem.*, 91: 5325–5332, 1987.
- G. Tomasello, A. Humeniuk, and R. Mitrić. *J. Phys. Chem. A*, 118(37):8437–8445, 2014.
- J. Tomasi, B. Mennucci, and R. Cammi. *Chem. Rev.*, 105:2999–3093, 2005.
- D. Toroz, M. Rontani, and S. Corni. *J. Chem. Phys.*, 134:024104, 2011.
- D. Toroz, M. Rontani, and S. Corni. *Phys. Rev. Lett.*, 110:018305, 2013.
- S. Trippel, J. Mikosch, R. Berhane, R. Otto, M. Weidemuller, and R. Wester. *Phys. Rev. Lett.*, 97:193003, 2006.
- M. Tulej, D. A. Kirkwood, M. Pachkov, and J. P. Maier. *Astrophys. J. Lett.*, 506(1): L14–L16, 1998.

- L. Turi and P. J. Rossky. *Chem. Rev.*, 112:5641–5674, 2012.
- S. Ullrich, T. Schultz, M.Z. Zgierski, and A. Stolow. *Phys. Chem. Chem. Phys.*, 6: 2796–2801, 2004.
- J.G. Underwood and K.L. Reid. *J. Chem. Phys.*, 113:1067–1074, 2000.
- D. Vanfleteren, D.V. Neck, P.W. Ayers, R.C. Morrison, and P. Bultinck. *J. Chem. Phys.*, 130:194104, 2009.
- L. Velarde, T. Habteyes, E. Grumblig, K. Pichugin, and A. Sanov. *J. Chem. Phys.*, 127:084302, 2007.
- A. M. Velasco, C. Lavin, O. Dolgounitcheva, and J. V. Ortiz. *J. Chem. Phys.*, 141: 074308, 2014.
- A. M. Velasco, C. Lavin, I. Martin, J. Melin, and J. V. Ortiz. *J. Chem. Phys.*, 131: 024104, 2009.
- J. R. R. Verlet, A. E. Bragg, A. Kammerath, O. Cheshnovsky, and D. M. Neumark. *Science*, 307:93–96, 2005.
- J. Wang, B. Yang, T.A. Cool, N. Hansen, and T Kasper. *Int. J. Mass Spectrom.*, 269: 210–220, 2008.
- M.L. Weichman, J.B. Kim, J.A. DeVine, D.S. Levine, and D.M. Neumark. *J. Am. Chem. Soc.*, 137:1420–1423, 2015.
- A.R. Welden, J.J. Phillips, and D. Zgid. *arXiv*, 2015. doi: arXiv:1505.05575.
- O. Welz, J.D. Savee, D.L. Osborn, S.S. Vasu, C.J. Percival, D.E. Shallcross, and C.A. Taatjes. *Science*, 335:204–207, 2012.
- O. Welz, J. Zador, J.D. Savee, L. Sheps, D.L. Osborn, and C.A. Taatjes. *J. Phys. Chem. A*, 117:11983–12001, 2013.
- A.H.C. West, B.L. Yoder, D. Luckhaus, C.-M. Saak, M. Doppelbauer, and R. Signorell. *J. Phys. Chem. Lett.*, 6:1487–1492, 2015.
- A.H.C. West, B.L. Yoder, D. Luckhaus, and R. Signorell. *J. Phys. Chem. A*, 119: 1237612382, 2015.
- W. Weyl. *Ann. Phys.*, 197:601–612, 1864.
- K.R. Wilson, L. Belau, C. Nicolas, M. Jimenez-Cruz, S.R. Leone, and M. Ahmed. *Int. J. Mass Spectrom.*, 249-250:155–161, 2006.

- B. Winter and M. Faubel. *Chem. Rev.*, 106:1176, 2006.
- H.J. Wörner, H. Niikura, J.B. Bertrand, P.B. Corkum, and D.M. Villeneuve. *Phys. Rev. Lett.*, 102:103901, 2009.
- M. Xie, Z. Zhou, Z. Wang, D. Chen, and F. Qi. *Int. J. Mass Spectrom.*, 293:28–33, 2010.
- Y. Yamamoto, Y.-I. Suzuki, G. Tomasello, T. Horio, S. Karashima, R. Mitríć, and T. Suzuki. *Phys. Rev. Lett.*, 112:187603, 2014.
- T. Yanai, D.P. Tew, and N.C. Handy. *Chem. Phys. Lett.*, 393:51 – 57, 2004.
- B. Yang, J. Wang, T. A. Cool, N. Hansen, S. Skeen, and D. L. Osborn. *Int. J. Mass Spectrom.*, 309:118–128, 2012.
- R. M. Young and D. M. Neumark. *Chem. Rev.*, 112:5553–5577, 2012.
- Y. Yuan, M. J. L. Mills, P. L. A. Popelier, and F. Jensen. *J. Phys. Chem. A*, 118: 7876–7891, 2014.
- T. Zeuch and U. Buck. *Chem. Phys. Lett.*, 579:1–10, 2013.
- J. Zhang, H. Zhang, T. Wu, Q. Wang, and D. van der Spoel. *J. Chem. Theory Comput.*, 2017. doi:10.1021/acs.jctc.7b00169.
- E. Zurek, P.P. Edwards, and R. Hoffmann. *Angew. Chem. Int. Ed.*, 48(44):8198–8232, 2009.